Thermoelectric properties of new transition metal arsenides and antimonides

by

Navid Soheilnia

A thesis
presented to the University of Waterloo
in fulfillment of the
thesis requirement for the degree of
Doctor of Philosophy
in
Chemistry

Waterloo, Ontario, Canada, 2007

Declaration

I hereby declare that I am the sole author of this thesis. This is a true copy of the thesis, including any required final revisions, as accepted by my examiners.

I understand that my thesis may be made electronically available to the public.

Abstract

The main focus of this work is on exploratory investigation of thermoelectric (TE) materials. Thermoelectric devices are solid-state devices that convert thermal energy from a temperature gradient into electrical energy (Seebeck effect), or convert electrical energy into a temperature gradient (Peltier effect). Modifying existing materials and finding new materials with proper thermoelectric properties are the two approaches considered in this research. Good thermoelectric materials are usually narrow band gap semiconductors with large Seebeck coefficient, reasonably high electrical conductivity and low thermal conductivity. Early transition metal antimonides and arsenides, with unique structural features were chosen for finding high performance TE materials.

During the investigation of group four antimonides, a series of new ternaries, $ZrSi_{\delta}Sb_{2-\delta}$, $ZrGe_{\delta}Sb_{2-\delta}$ and $HfGe_{\delta}Sb_{2-\delta}$ was developed. Single crystal X-ray diffraction was used for crystal structure determination, and energy depressives X-ray analysis (EDX) was used for compositional analysis. Metallic properties of these compounds were predicted by electronic structure calculations and confirmed by physical property measurements.

It was revealed that Mo_3Sb_7 turns semiconducting by partial Sb/Te exchange. Similarly, isostructural Re_3As_7 was modified to become semiconducting by partial Ge/As exchange. Crystal structures were determined by single crystal X-ray and powder X-ray diffraction utilizing Rietveld method. Electronic structures were determined by using the LMTO method and confirmed the semiconducting properties of these ternary compounds. Physical property measurements showed exceptional TE properties for these compounds. It was also confirmed by the X-ray single crystal analysis that it is possible to intercalate different cations with the proper size into the existing cubic voids of the structure. The effect of cation intercalation on physical properties of these compounds were investigated and revealed the enhancement of transport properties as a result of this intercalation.

Acknowledgements

I thank god for giving me the strength to achieve my dream. I am indebted to Professor Holger Kleinke for his friendship, invaluable guidance, encouragement and support. I was so fortunate to work under his supervision and grateful for the diversity of the experience I have gained through out these years.

I owe special thanks to my wonderful wife, Azin, whose love, supports, patience and encouragements enabled me to complete my studies and made it a memorable time.

I would like to thank my parents who thought me how to be a better person. I am also thankful for all the family love and support.

I have been blessed in having great colleagues. Many thanks to Dr. Abdeljalil Assoud, Yanjie Cui, Dr. Enkhtsetseg Dashjav, Dr. Shahab Derakhshan, Michael Garland, Arnaud Germain, John Giraldi, Dr. Jean Paul Jemetio, Katja Kleinke, Dr. Chi-Shen Lee, Jackie Xu , Hong Xu, Pingjian Zhou and Victor Zhu.

I am also thankful for my advisory committee members, Prof. R. T. Oakley, Prof. L. F. Nazar, and Prof. Kathryn Preuss for their comments and suggestions during the course of my research. I also appreciate my examiners, Prof. Y. Mozharivskyj and Prof. L. Simon for their time.

For Azin

Table of Contents

List of Figures

List of Tables

List of Abbreviations

a	crystallographic unit cell axis
Å	angstrom
a^*	reciprocal unit cell axis
b	crystallographic unit cell axis
B	B parameter
b^*	reciprocal unit cell axis
c	crystallographic unit cell axis
c^*	reciprocal unit cell axis
CCD	charge coupled device
cm^{-1}	reciprocal centimeter
COHP	crystal orbital Hamilton population
COOP	crystal orbital overlap population
C_p	specific heat
C_v	heat capacity
CVD	chemical vapor deposition
DOS	density of states
E_a	activation energy
EDX	energy dispersive X-ray
E_F	Fermi energy
E_g	energy band gap
eV	electron volt
ϕ	coefficient of performance

f	atomic scattering factor
$F_{(hkl)}$	crystallographic structure factor
GOOF	goodness of fit
GSAS	general structure analysis system
η	power generation efficiency
h	Plank constant
$\hbar$	reduced Plank constant
I	current
ICOHP	integrated crystal orbital Hamilton population
IPD	image plate detector
K	degree Kelvin
κ	thermal conductivity
k	wave vector
k_B	Boltzmann constant
κ_e	electronic thermal conductivity
κ_{ph}	lattice thermal conductivity
L	Lorenz number
LDA	local density approximation
LMTO	linear muffin-tin orbital
μ	carrier mobility
m^*	effective mass
MOP	Mulliken overlap population
N_A	Avogadro's number

N_V	band degeneracy
ºC	degrees centigrade
Π	Peltier coefficient
PGEC	phonon-glass, electron-crystal
PSD	position sensitive detector
PXRD	powder X-ray diffraction
Q	heat flow
θ_D	Debye temperature
ρ	specific resistivity
R	gas constant
R_H	Hall coefficient
S	Seebeck coefficient
σ	electrical conductivity
τ	carrier scattering time
$t_{1/2}$	half-rise time
TE	thermoelectric
υ	velocity of sound
Ω	Ohm
ZT	figure-of-merit

Chapter 1

1. Thermoelectrics

1.1 Introduction

The finite sources of fossil fuels and environmental considerations are becoming the main concerns of countries and scientific communities. Reducing the green house gas emissions and lowering the dependency on fossil fuels are some of the most important issues and concerns of the world. Limited natural resources, environmental pollution and global warming are some concerns and motivations for finding alternative sources of energy. For decades scientists have been focusing on these problems and trying to find solutions. Solar cells[1], wind turbines[2] and fuel cells[3] are some of the directions in which research is moving. Thermoelectrics are materials capable of converting heat into electricity and vice versa.[4] Thermoelectric generators are solid state devices that use the Seebeck effect, and thermoelectric coolers are solid state heat pumps that use the Peltier effect[5] (Figure 1.1). These are reliable and environmental friendly devices with one important weak point: low efficiency.

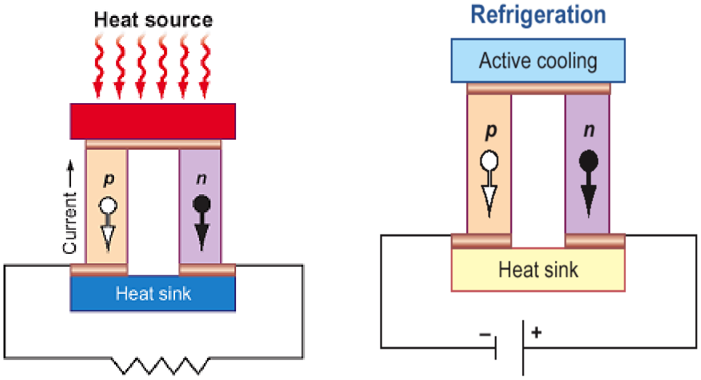

Figure 1.1 Power generation (left) and refrigeration (right) in thermoelectrics.[6]

Over the past decade an increasing interest in thermoelectric materials has developed.[7] Recent advances in material science, synthesis techniques and characterization methods, have made research on thermoelectrics a rapidly expanding subject for scientific research communities around the globe. This chapter will focus on a brief history of thermoelectric materials, efficiency in thermoelectric materials, desirable properties to achieve high efficiency materials, some of the latest developments in this field and the best materials available as high performers up to the present. A typical thermoelectric module (Figure 1.2) consists of *p*-type and *n*-type semiconducting materials that are connected electrically in series and thermally in parallel.

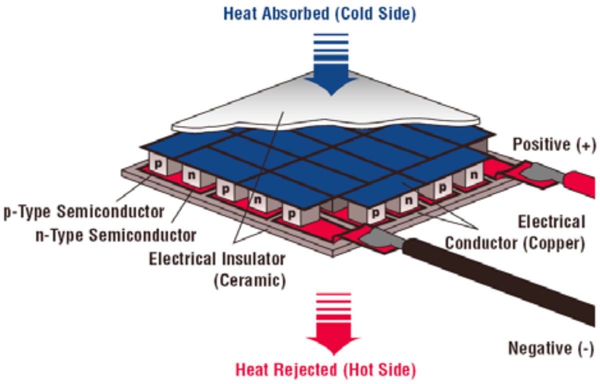

Figure 1.2 Typical thermoelectric module.[8]

1.2 History of thermoelectric materials

In 1821, Estonian born scientist, Thomas John Seebeck (1770-1831), found that if the junctions of two different metals are placed at different temperatures, a compass magnet would deflect when it is placed near the closed loop circuit.[9] He also found out that the magnitude of deflection was proportional to the temperature difference and depended on the type of the conducting materials. At first he thought deflection is the result of magnetic field induced by temperature,[9] but soon he realized that the deflection is the result of an electric current produced because of temperature difference in the closed circuit, and the voltage produced is proportional to the temperature difference between the two junctions. This proportionality is known as Seebeck coefficient (S), often called thermopower. The voltage difference (ΔV) is proportional to temperature difference between the hot side and the cold side ($\Delta T = T_H - T_C$):

$$S = \frac{\Delta V}{\Delta T} \; [\mu V K^{-1}]$$

He tested this effect on a large number of materials and arranged them in order of the product $S\sigma$, where S is Seebeck coefficient and σ is electrical conductivity ($\Omega^{-1}cm^{-1}$).

When heat is applied to one side of the thermoelectric material, electrons as charge carriers gain higher kinetic energy, and since it is relatively easy for them to move in the material, they diffuse from the hot side to the cold side. After a while, negatively charged electrons will be accumulated at the cold side, and positively charged holes will be accumulated at the hot side. This charge accumulation on both sides results in a potential difference between the two junctions, and an electrical current, when the two sides get connected. This current will be maintained as long as the temperature gradient exists (Figure 1.3).

Figure 1.3 Temperature gradient between the two ends of the bar shaped thermoelectric material causes charge accumulation and potential difference between the hot end and the cold end.

Around 13 years later, in 1834 a French watchmaker and part time physicist, Jean Charles Athanase Peltier (1785-1845), discovered the complementary effect. He noticed the temperature change at the junction between the two different conductors when an electrical current passes through.[10] Peltier did not know the relation between this effect and Seebeck's experiments and observations. In 1838 a Russian scientist, Emil Lenz (1804-1865), showed that depending on the direction of the current, heat could be absorbed or generated at the junction of the two different conductors.[11] He showed water freezes at a bismuth-copper junction, and melts when the direction of the flow reversed. The Peltier coefficient (Π) is described by the ratio of the heat flow (Q [js^{-1}]) to the applied current (I [A]):

$$\Pi = \frac{Q}{I}\ [WA^{-1}]$$

About 20 years later in 1851 William Thomson (Lord Kelvin) predicted a relationship between the Seebeck and the Peltier coefficient, and introduced a third thermoelectric effect, the Thomson effect.[12] Based on his theory, he concluded that the heat produced or absorbed in this phenomenon is related to both the electrical current and the temperature gradient:

$$q = \rho \cdot J^2 - \mu J \frac{dT}{dX}$$

where ρ is the resistivity, J is the current density, μ is the Thompson coefficient and dT/dX is the temperature gradient along the sample. In 1885 Rayleigh considered the possibility of using the thermoelectric effect for power generation.[5] In 1909 and 1911 Altenkirch gave a better theory for the thermoelectric power generation and refrigeration.[13, 14] In his theory he states that good thermoelectric materials should have large Seebeck coefficients (S), high electrical conductivity (σ) to minimize the joule heating, and low thermal conductivity (κ) to maintain the temperature gradient between the hot and cold side.

Metals and metal alloys were the main focus of the thermoelectric research, and because of their low Seebeck coefficients, they were not the appropriate materials for thermoelectric applications. In metals the ratio of thermal conductivity to electrical conductivity is constant at a given temperature (Wiedemann-Franz law).[15] Thus it is impossible to increase the electrical conductivity and lower the thermal conductivity at the same time in metals. It was shown in late 1930s that synthetic semiconductors could have a Seebeck coefficient above 100μV/K.[5]

A Russian scientist, A. F. Ioffe, developed the theory of semiconductor thermo elements in 1949.[11] In 1954 Goldsmid and Douglas showed that thermoelectric coolers could reach sub zero temperatures (ºC).[16] Unfortunately large gap semiconductors have very low electrical conductivity; therefore, they are not ideal for thermoelectric applications. Later in 1956 Ioffe and his coworkers showed the semiconductors that were made at that time for transistor applications had much larger electrical conductivity, and correspondingly these semiconductors exhibited much better thermoelectric properties. It was observed that if a thermoelectric material would be alloyed with elements or compounds with similar crystal structure, the thermoelectric properties would further improve.[17]

The main focus of this study is on finding new materials or modifying some of the existing materials in order to prepare high performance materials for thermoelectric power generators and cooling devices. Detailed and clear understanding of crystal structure and physical properties of materials are vital for effective research. The main part of the discussion in this chapter is dedicated to the important crystal structure and electronic structure details for efficiency improvements in thermoelectric materials.

1.3 Applications, advantages and disadvantages

Replacing fossil fuels as the main source of power generation and finding a more efficient way to produce energy with less maintenance and pollution are becoming a necessity. Thermoelectric power generation and thermoelectric cooling seem to be good answers to all of these needs. There are large varieties of applications available for these materials such as power source for electronic and mechanical devices in remote locations (arctic regions and along the pipelines), medical applications such as pace makers, and also applications where the reliability and absence of moving parts outweigh other factors such as cost and efficiency, like space probes and waste heat recovery. As for thermoelectric cooling devices, refrigerators without moving parts and cooling fluids, environmental friendly air conditioners, CPU coolers in laptops and portable coolers for food and beverages are some to name. Figure 1.4 shows selected commercially available thermoelectric materials.

Figure 1.4 Applications of thermoelectrics in power generation and cooling devices.[18]

The down side of these materials is their low efficiency (around 5%) and high cost compared to traditional power generators or refrigerators. In spite of the large waste of energy through the waste heat in the exhaust and coolant in gasoline fuel operating vehicles,[19] the efficiency (25% of the fuel energy) for combustion engines are still higher compared to thermoelectric power generators.

1.4 Thermoelectric efficiency

Altenkirch mentioned that a good thermoelectric material should possess a high Seebeck coefficient, a high electrical conductivity and a low thermal conductivity. These properties are related to each other in a so-called figure-of-merit Z (K^{-1}):[20]

$$Z = \frac{S^2\sigma}{\kappa}\ [K^{-1}]$$

Where S is Seebeck coefficient, σ is electrical conductivity and κ ($\kappa=\kappa_{ph}+\kappa_e$) is the total thermal conductivity (sum of the lattice and the electronic contribution). For simplicity one can define ZT as the dimensionless figure-of-merit:[6]

$$ZT = T\times\frac{S^2\sigma}{\kappa}$$

The product of $S^2\sigma$ is called power factor and has higher values in narrow gap semiconductors,[7] compared to metallic compounds. The figure-of-merit for a module consisting of a *p*-type and *n*-type material can be calculated by the relationship below:[21]

$$ZT = T\times\frac{(S_p - S_n)^2}{[(\sqrt{\frac{\kappa_n}{\sigma_n}} + \sqrt{\frac{\kappa_p}{\sigma_p}})]^2}$$

The efficiency (η) in power generation and the coefficient of performance (ϕ) in refrigeration mode are directly related to the ZT value. The efficiency (η) for power generation is the ratio of the electrical power output (W) over the thermal power supplied (Q_H), and the coefficient of performance (ϕ) corresponds to the ratio of cooling rate (Q_C) over the power supplied (W).[5, 22]

$$\eta = \frac{W}{Q_H} = \frac{T_H - T_C}{T_H} \times \frac{\sqrt{1+ZT} - 1}{\sqrt{1+ZT} + \frac{T_C}{T_H}}$$

$$\phi = \frac{Q_C}{W} = \left(\frac{T}{T_H - T_C} \times \frac{\sqrt{1+ZT} - 1}{\sqrt{1+ZT} + 1}\right) - \frac{1}{2}$$

For both equations $T = \frac{T_H + T_C}{2}$. Since the main focus of this work is on thermoelectric power generation, parameters related to the power generation efficiency, η, will be discussed. The efficiency formula consists of two parts, Carnot efficiency ($\frac{T_H - T_C}{T_H}$) and the loss term ($\frac{\sqrt{1+ZT} - 1}{\sqrt{1+ZT} + \frac{T_C}{T_H}}$). Higher ZT value will result in higher efficiency, and when ZT reaches infinity, the efficiency reaches the Carnot efficiency.[7] High ZT value can be achieved with high Seebeck values, reasonable electrical conductivity and low thermal conductivity. The focus in this section is on introducing different parameters important for increasing ZT and the relationship between these parameters.

1.4.1 Optimum materials for thermoelectric applications

Before getting into a detailed discussion about each parameter in the figure-of-merit expression, choosing the appropriate material for this application is very important. Figure 1.5 shows the dependence of the electrical conductivity, the Seebeck coefficient and the thermal conductivity on the concentration of free carriers. Low carrier concentration materials like insulators, in spite of their high Seebeck coefficient, are usually not considered as proper materials for these applications. Extremely low electrical conductivity of these materials is the reason behind this conclusion. Moreover, for high carrier concentration materials like metals, low Seebeck values and very large thermal conductivities are the two main reasons that eliminate them as good candidate materials for thermoelectric applications. Only small-gap semiconductors fall into the appropriate category of materials.

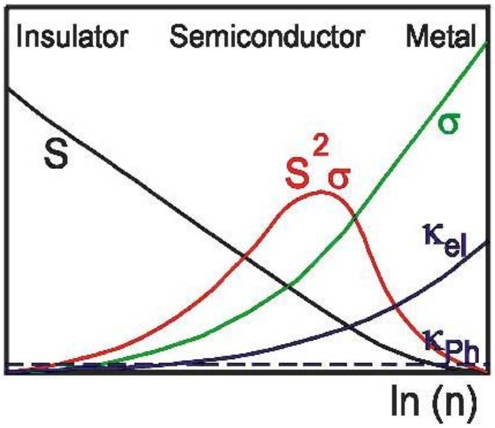

Figure 1.5 Dependence of S, σ and κ on carrier concentration.

1.4.2 Seebeck coefficient

The Seebeck coefficient is explained by the Mott equation.[23] The Mott equation shows that the Seebeck coefficient is proportional to the logarithmic derivative of σ with respect to E, above and below the Fermi level.

$$S = \frac{\pi^2}{3} \cdot \frac{k^2 T}{e} \cdot \left.\frac{d \ln \sigma(E)}{dE}\right|_{E=E_F}$$

According to Mahan et al.,[20] the Seebeck coefficient is proportional to the first derivative of the density of states (DOS) with respect to energy, E, above and below the Fermi level :

$$S \propto \frac{1}{DOS(E)} \cdot \left.\frac{d\, DOS(E)}{dE}\right|_{E=E_F}$$

Since the electrical conductivity (σ) increases with DOS ($\sigma \propto DOS(E)\big|_{E=E_F}$), increasing σ will result in decreasing S. The density of states and the band structure will be discussed in chapter two. This argument implies the importance of the electronic structure, especially the shape of the bands above and below the Fermi level. One of the most important pieces of information that can be deduced from the electronic structure of a compound is the shape of the bands around the Fermi level. This band shape e.g., flat bands or steep bands, affects the conduction process. In a free-electron gas model, energy (E) is proportional to the square of the wave vector *k*:[21]

$$\mathrm{E} = \frac{\mathrm{h}^2 k^2}{8\pi^2 m^*}$$

Where h is Planck's constant and m^* is the effective mass of the charge carriers. A partial's effective mass is the mass of transport in a crystal. Electrons and holes as charge carriers in a crystal behave the same as free particles in a vacuum, in respond to electric and magnetic field, but with different mass and this difference is called the effective mass of the charge carriers. The first derivative of E versus *k* is the measure of the band dispersion and has inverse relationship to the effective mass, m^*:

$$\frac{\mathrm{dE}}{\mathrm{d}k} = \frac{\mathrm{h}^2 k}{4\pi^2 m^*}$$

This derivative is physically related to the band velocity, $\mathrm{v} = \frac{\mathrm{p}}{m^*}$, where p is the momentum, that can be obtained by the de Broglie equation, $\mathrm{p} = \frac{\mathrm{h}k}{2\pi}$. By replacing the momentum in the band velocity equation, the new velocity relationship can be deduced:

$$\mathrm{v} = \frac{\mathrm{h}k}{2\pi m^*}$$

The carrier mobility and the energy can be directly related to the first derivative of E versus *k*:

$$\mathrm{v} = \frac{2\pi}{\mathrm{h}} \cdot \left(\frac{\mathrm{dE}}{\mathrm{d}k}\right)$$

Large band dispersions will result in large carrier mobility and large conductivity, while small band dispersions (flat bands) result in smaller mobility and smaller electrical conductivity. Coexistence of both flat bands and steep bands around the Fermi level will be the ideal condition to have optimum conductivity and Seebeck in one compound. Wide bands interpret into wide density of states and flat bands interpret into spikes in the density of states.

1.4.3 Electrical conductivity

The electrical conductivity is a result of charge carrier movement. When an electrical potential difference along the conducting material exists, mobile charge carriers create an electrical current. For any conductive material, σ can be expressed as the product of charge carrier concentration, n, carrier charge, ē (1.602×10^{-19} C), and the carrier mobility, μ ($\frac{\text{cm}^2}{\text{Vs}}$):[24]

$$\sigma = n\bar{e}\mu$$

The carrier mobility is a function of the carrier scattering time (τ), the effective mass (m^*) in the direction of the current (I), and the carrier charge:

$$\mu = \frac{\bar{e}\tau}{m^*}$$

The carrier scattering time is the time that the charge carrier loses the momentum. Materials containing elements with similar electronegativity are more likely to have higher scattering time, resulting in higher electrical conductivity.[25] The effective carrier mass, m^*, has an important role in carrier mobility. It is responsible for transport properties in a crystal, where electrons or holes behave in a similar fashion like the free particles, but with different masses.[26] The effective mass can be expressed by a combination of Newton's second law

($\vec{F} = m\vec{a}$, $\vec{F} = \text{net force}, m = \text{mass}, \vec{a} = \text{acceleration}$) and quantum mechanic. For an electron in an external electric field, E, " $\vec{a}$ " would be defined as:

$$\vec{a} = \frac{1}{\hbar^2} \cdot \frac{d^2\varepsilon}{dk^2} \cdot q \cdot \vec{E}$$

" $\vec{a}$ " is acceleration, $\hbar$ is the reduced Planck's constant, $\hbar = h/2\pi$, k is the wave vector, which shows how the phases of the orbitals change when the translational symmetry is applied, i.e. the energy ε is a function of k. $\vec{E}$ is the external electrical field and q is the charge. The force that electrons experience under the external field can be expressed by: $\vec{F} = q \cdot \vec{E}$, and the effective mass under the existence of an external electrical field can be calculated:

$$\frac{1}{m^*} = \frac{1}{\hbar^2} \cdot \frac{d^2\varepsilon}{dk^2}$$

The effective mass depends on the bandwidth, which depends on orbital overlap.[26] Wide bands have smaller effective masses, which translates into higher mobility and conductivity in comparison to narrow bands (flat bands) with larger effective masses and lower mobility.

Electrical conductivity is a function of temperature. In metals, conductivity decreases by increasing the temperature because of the decrease in mobility due to increasing phonon vibrations and decreasing scattering time (τ). As for semiconductors, increasing temperature results in increasing the number of charge carriers and ultimately causes an increase in electrical conductivity. The number of charge carriers in intrinsic semiconductors changes exponentially with the band gap size and the temperature (exp ($-E_g/2kT$).

1.4.4 Thermal conductivity

The thermal conductivity, κ, is the measure of heat transferred through a material. Both the charge carriers and the vibrations of the lattice (phonons) can transfer the heat. The total thermal conductivity is the sum of the contributions by both phonons and charge carriers:

$$\kappa=\kappa_e+\kappa_{ph}$$

For metals, large numbers of charge carriers are responsible for high thermal conductivity. In metals, the major contribution to the thermal conductivity is electronic; and the phonon contribution has a smaller effect. According to the Wiedemann-Franz law[15], the ratio of the thermal to the electrical conductivity for all metals at a given temperature is the same:

$$\kappa_e = L\sigma T$$

Where L is Lorentz number ($L=2.45\times10^{-8}$ WΩK^{-2}). Knowing the relationship between the electrical conductivity and electronic contribution of thermal conductivity, one can rewrite the figure-of-merit as:

$$ZT = \frac{S^2}{L\cdot(1+\frac{\kappa_{ph}}{\kappa_e})}$$

This formula clearly shows materials with large S, large κ_e and low κ_{ph} are best for achieving high ZT values. Metals have large κ_e values and very low Seebeck coefficient, which make them inappropriate for thermoelectric applications. Semiconductors on the other hand have large Seebeck value, small electronic contributions and the possibility of minimizing phonon contribution to achieve higher ZT values. Typically, increasing σ decreases the Seebeck value but it is possible to reduce κ_{ph} without affecting the electronic transport properties of the material.

In 1914 Debye expressed a theory on conduction of heat by the lattice vibration.[15] In his theory he assumed that thermal conductivity of a defect-free crystal should be infinite at all temperatures, if all the forces between the atoms are elastic. If any change happens to these forces between the atoms, the conductivity becomes finite. These changes will result in a sound velocity change and scattering of the vibrational waves responsible for the thermal conductivity. Sound velocity, is the velocity of a particle in an environment as it transmits a wave. Peierls improved Debye's theory on lattice thermal conductivity. He used the idea of vibrational waves (phonons), assuming that the kinetic theory of gases is valid for the phonons.[27]

$$\kappa_{ph} = \frac{1}{3} C_v \upsilon l$$

C_v is the heat capacity, υ is the velocity of sound and l is the average distance that vibrational waves travel before scattering. At high temperatures (T > ~300 K) the sound velocity and the heat capacity are temperature-independent and therefore the mean free path of the phonons can be used to determine the lattice thermal conductivity. The Debye temperature (θ_D) is the temperature of the crystal's highest normal mode of vibration.[28] Materials with low Debye temperatures have small κ_{ph}. Low bond energies and high atomic masses will result in low Debye temperatures. Atomic disorders and large unit cells are also important factors that can help reducing the phonon thermal conductivities. Pohl and his collaborators introduced the idea of the thermal conductivity of crystals with glass-like behavior.[29] Due to their large disorder, glasses have the lowest thermal conductivity. They concluded that many aspects of the thermal conductivity in glasses are not well known and held small phonon mean free-path responsible for low thermal conductivity in glasses. Slack proposed the possibility of having materials with glass like thermal conductivities and crystalline like electrical properties.[30]

Such materials are called "phonon glass-electron crystal" or PGEC materials. These materials can be prepared by having heavy atoms in large pockets or cages in a crystalline network of a compound. These heavy atoms can rattle in the cage and lower the thermal conductivity without having large effects on the electronic properties of the compound.

In recent years, Mahan described the characteristics of good thermoelectric materials, suggesting some microscopic parameters that can be used to improve ZT for a thermoelectric material.[31]

$$ZT = f(E_g, B)$$

E_g is the semiconductor band gap. ZT increases by increasing E_g until E_g=6-10k_BT (k_B, Boltzmann constant), for band gaps larger than 10k_BT the ZT plateaus. The gap must be large enough so that no intrinsic carriers exist. Aside from this property, the gap size has no other effect on ZT. The optimum gap size depends on the operating temperature, for example for operating device at 300 K, the optimum gap size should be 0.2 eV (~ 8k_BT). The most important factor for increasing ZT is the B parameter (Figure 1.6). This parameter includes all the material properties:

$$B \propto \frac{N_v \mu (m^*)^{3/2}}{\kappa_{ph}}$$

μ is the carrier mobility, m^* is the effective band mass and N_v is the degeneracy of the band extrema (top of the valence band for *p*-type and bottom of the conduction band for *n*-type materials).

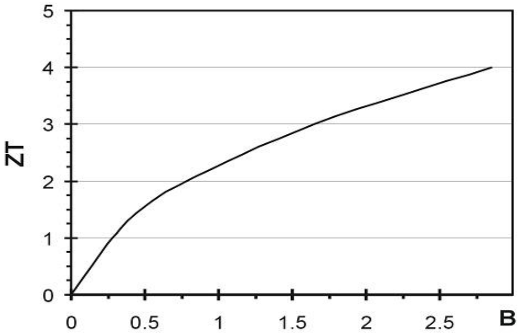

Figure 1.6 The relationship between ZT and B.[25]

The band degeneracy (N_v) is an important factor for increasing the B parameter. N_v is the number of degenerate extrema at the Fermi level. N_v can be as high as 48 by symmetry.[32] As for a comparison, $InBi_2Te_3$ has N_v=6, Si-Ge alloys have N_v=6 and PbTe has N_v=4. N_v(max) is determined only by crystal symmetry. Table A. 1, shows the maximum N_v for different Laue classes. The actual value for N_v is related to the details of the band structure. Only when the band extrema appear at a general point in the Brillouin zone, can N_v(max) be achieved.[25] Compounds with small unit cells or simple stoichiometry usually have these extrema at high symmetry points, e.g., on the reciprocal axis, which result in lower N_v values. There is no rule that can exactly predict the maximum degeneracy; generally large spin-orbit coupling and large unit cells make it possible to achieve larger N_v values. The spin-orbit coupling can introduce changes in energy of the atomic spin-orbit coupling constant (0.1 eV or more in crystals of heavy atoms) and may therefore greatly change the details of the band.[33]

1.5 Advanced materials for thermoelectric applications

The big challenge in finding proper materials for thermoelectric applications is tuning the properties to increase performance. Different approaches can be considered based on the desired type of the materials: bulk or low-dimensional or nano-scale materials.[6] Traditional solid-state reactions are used for preparing bulk materials. Nanomaterials and thin films are prepared by techniques such as chemical vapor deposition (CVD).

1.5.1 Low dimensional materials

The ZT formula shows the dependency of the figure-of-merit on the transport properties of solids. The transport properties, σ, S and κ are inter-related in regular three-dimensional structures, and it is hard to change one property without affecting the other properties. The idea behind the low-dimensional systems is that decreasing dimensionality and size causes difference in the DOS and allow independent changes of transport properties (σ, S, κ).[34] It is also known that nano-structured semiconductor materials can better scatter phonons with mid to long wave length and get closer to the κ_{min} value.[35] Figure 1.7 compares the density of states of bulk materials and low dimensional materials.

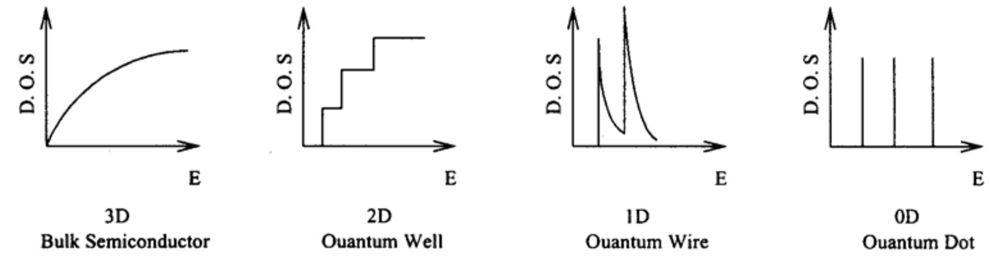

Figure 1.7 Density of states for a bulk three-dimensional semiconductor, a two-dimensional quantum well, a one-dimensional quantum wire and a zero-dimensional quantum dot.[34]

Three research approaches toward low-dimensional materials are being considered:

1. The use of quantum confinement effects[35] that enhance the density of states near the Fermi energy. The ZT value reported by using this approach is 0.9 at 300 K and 2.0 at 550 K in $PbSe_{0.98}Te_{0.02}/PbTe$ quantum-dot structures.[36]

2. The phonon-blocking, electron-transmitting super lattice approach, which benefits from mismatch between components of the super lattice to reduce the κ_{ph}.[37] The ZT value (≈330 K) reported by using this approach is ≈ 2.4 in *p*-type Bi_2Te_3/Sb_2Te_3 super lattices and ≈ 1.4 in *n*-type $Bi_2Te_3/Bi_2Te_{2.83}Se_{0.17}$ super lattices.[38]

3. Thermionic effects in hetero structures.[39, 40]

1.5.2 Bulk materials, Skutterudites

The skutterudite is the name of the $CoAs_3$ based mineral. It was mined as a source of cobalt in the region of Skutterud, Norway.[41] These materials have cubic structure and their properties highly depend on their compositions. Eight corner-shared octahedra TX_6 (T=Co, Fe, Rh, Ir; X=P, As, Sb), make a void at the center of the $(TX_6)_8$ cluster (Figure 1.8). The crystal structure of the skutterudites has two voids in each unit cell, which are large enough to accommodate large lanthanide atoms. The filled compounds are called filled skutterudites with general formula of $R_{1-Z}T_4X_{12}$ ($Z \leq 1$), where R is the lanthanide.

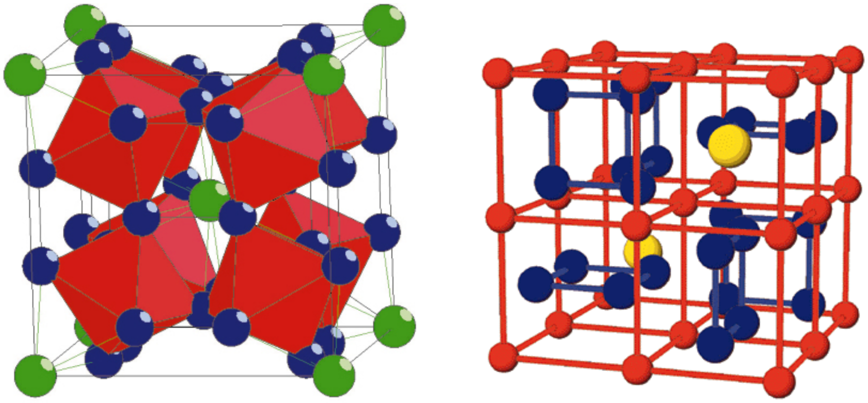

Figure 1.8 Schematic view of a filled skutterudite.[42]

Introducing lanthanide atoms as guests into the existing voids of skutterudites resulted in good thermoelectric properties of these compounds.[42, 43] In 1996, Sales et al.[44] and Fleurial et al.[45] reported high ZT values for $LaFe_3CoSb_{12}$ and $CeFe_3CoSb_{12}$ at high temperatures. The ZT value is expected to reach ≈1.4 at 1000 K for $CeFe_3CoSb_{12}$.[46] Recent studies showed that partially filled skutterudites have higher ZT values due to the combination of low thermal conductivities and higher power factors.[47-50] Strong phonon scattering and low thermal conductivity of these compounds confirmed the validity of Slack's PGEC concept. Partial filling of the holes will result in transport property improvements and higher power factors.[51] Skutterudites are not only good thermoelectric materials, but also helped scientists to develop a better understanding of the thermal transport processes and phonon-scattering mechanisms.

1.5.3 Bulk materials, Chalcogenides

Many salts of heavier chalcogenides (Se, Te) exhibit semiconducting behavior and have high melting points. These are attractive properties for thermoelectric materials. The difference in the electronegativities from sulfur to tellurium makes it possible to have many different semiconducting materials with small energy gaps appropriate for thermoelectric materials. Depending on the band gap size, they can be suitable for operation over a wide range of temperatures (≈ 200-1400 K).[51] Most of the commercially available thermoelectric materials up now are chalcogenide compounds. The famous Bi_2Te_3 and its solid solutions, $Bi_{2-x}Sb_xTe_3$ and $Bi_2Te_{3-x}Se_x$,[21] PbTe with ZT ≈ 0.8 at 500ºC and TAGS (Te-Ag-Ge-Sb) are well-known examples.[52] In this section a few good thermoelectric chalcogenides will be presented.

Kanatzidis et al. reported a ternary compound with good thermoelectric properties. Introducing cesium into the mixture of bismuth and tellurium results in a complete structural change from Bi_2Te_3, and formation of a new compound, $CsBi_4Te_6$.[53] This compound crystallizes in the space group *C*2/*m* and has a highly anisotropic layered structure.[54] Figure 1.9 shows the slabs of anionic $[Bi_4Te_6]^-$ alternating with layers of Cs^+ ions.

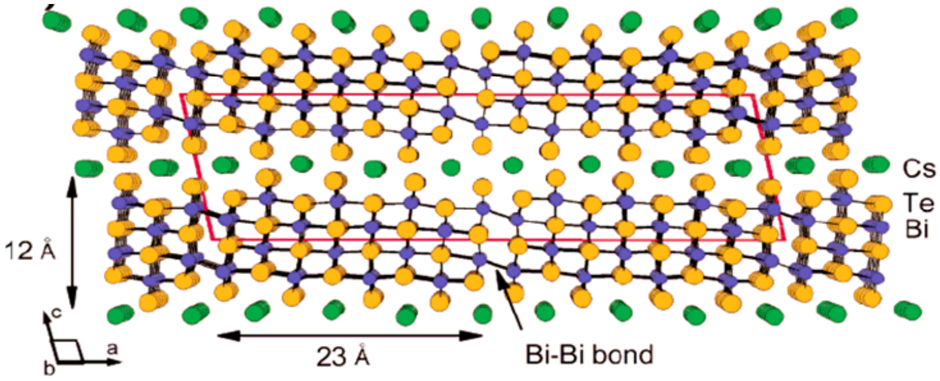

Figure 1.9 Monoclinic crystal structure of $CsBi_4Te_6$ along the *b*-axis.[53]

The transport properties of $CsBi_4Te_6$ are very sensitive to the level of doping. Doped with SbI_3, a ZT value of 0.8 at 225 K was attained. This is the best ZT for a bulk material below room temperature so far. The existence of a Bi–Bi bond in this structure is responsible for the small band gap (≈ 0.08–0.1 eV), compared to Bi_2Te_3 (0.16 eV), occurring with a lower temperature for the maximum ZT value.

The Kanatzidis group recently reported a family of materials based on lead chalcogenide. Lead antimony silver telluride (LAST) of the general formula $AgPb_mSbTe_{m+2}$ showed promising properties as a thermoelectric material. This compound forms a super structure of the NaCl type (Figure 1.10).[55]

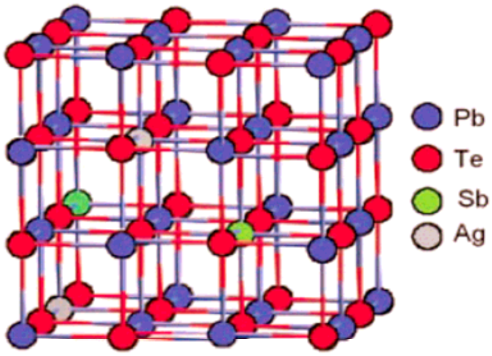

Figure 1.10 Crystal structure of cubic $AgPb_mSbTe_{m+2}$.[55]

Recent studies revealed the existence of at least two inhomogeneous nano scale phases within the major phase.[56] The high numbers of these nano scale phases help reducing the thermal conductivity by reducing the phonon transmission. The LAST materials have very low lattice thermal conductivities, ~ 0.45 $Wm^{-1}K^{-1}$ at 700 K depending on "m". A large number of compositions can be prepared by changing m in $AgPb_mSbTe_{m+2}$ (LAST-m). Properly doped materials exhibit high ZT values (≈ 1.2 for LAST-10 to ≈ 1.7 for LAST-18 at 700 K). LAST-18 has *n*-type properties with $\sigma \approx 1850\ \Omega^{-1}cm^{-1}$ and $S \approx -135\ \mu VK^{-1}$ at 300 K.

To build a thermoelectric device, both *p*-type and *n*-type materials are needed. Kanatzidis et al. reported a *p*-type counterpart for *n*-type $AgPb_mSbTe_{m+2}$.[57] The general formula of this *p*-type material is $Na_{1-x}Pb_mSb_yTe_{m+2}$, and with appropriate combinations of m, y and x, large values of ZT can be achieved. With m = 20, x = 0.05 and y =1, $\sigma \approx 1541\ \Omega^{-1}cm^{-1}$ and $S \approx 96\ \mu VK^{-1}$ at 300 K, a large power factor of 19 $\mu Wcm^{-1}K^{-2}$, were obtained.

Like the *n*-type material, the high ZT values for these compounds are related to their low thermal conductivity (≈ 1.8 $Wm^{-1}K^{-1}$ at room temperature to ≈ 0.85 $Wm^{-1}K^{-1}$ at 700 K). Large mass disorders in the atomic positions of the crystal structure, lowers the thermal conductivity of the material. High-resolution transmission electron microscopy (HRTEM) showed the existence of the nano scale inhomogeneous phases in the crystal structure, explaining the low thermal conductivity in these compounds.

1.5.4 Bulk materials, Oxides

A good thermoelectric material possesses high Seebeck coefficient, reasonable electrical conductivity and low thermal conductivity. For commercial application, other conditions such as cost, toxicity and abundance of the starting materials should be considered as well. Some oxide materials can operate in air, are often non-toxic and usually cost efficient and often stable at elevated temperatures. Because of the low mobility of most oxides, they were not considered as good thermoelectric materials.[58] Interesting transport properties of the layered cobalt oxides, $NaCo_2O_4$[59] and $Ca_3Co_4O_9$[60, 61] attracted the attention of the thermoelectric community. Large Seebeck values (≈ 100 μVK^{-1}) and high electrical conductivity (≈ 5000 $\Omega^{-1}cm^{-1}$) at room temperature are promising properties for thermoelectric applications. Layered sodium cobalt oxides crystallize in variants of the CdI_2 structure type with CoO_2 layers alternatively stacked along the *c*-axis with Na (Figure 1.11). CoO_2 layers consist of edge-sharing CoO_6 octahedra.

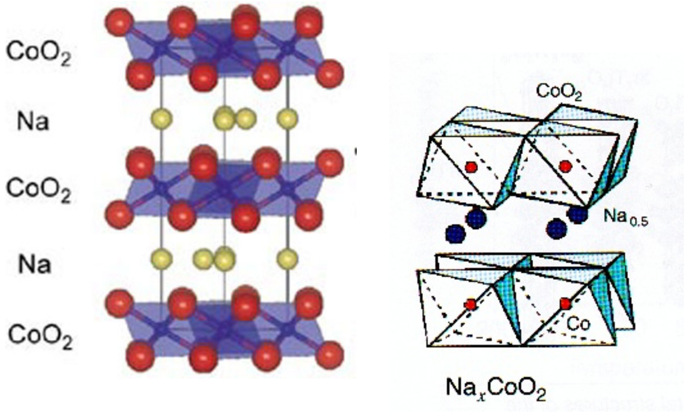

Figure 1.11 Crystal structure of layered sodium cobalt oxide.[62, 63]

Layered calcium cobalt oxides form a slightly different structure. It is known to be a misfit-layer structure with hexagonal CoO_2 layers, related to the CdI_2 type, and square Ca_2CoO_3 layers related to the NaCl type.[61, 64] The Ca_2CoO_3 layers between the CoO_2 layers result in a highly distorted interface and a *b*-axis lattice misfit (Figure 1.12).

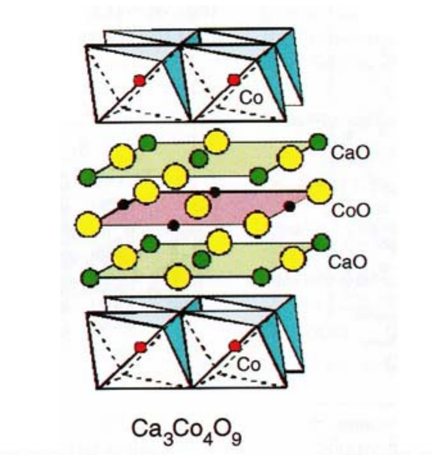

Figure 1.12 Crystal structure of $Ca_3Co_4O_9$[62].

Interesting structural features of layered cobalt oxides make them attractive for thermoelectric studies. The edge-shared CoO_6 layers serve as electronic transport layers, and sodium and Ca_2CoO_3 layers can act as phonon scattering regions and reduce thermal conductivity.[64] The research on the synthesis and improvement of the oxide materials for thermoelectric applications is currently the main subject of interest for many research groups.

1.6 References

[1] G. M. Masters, *Renewable and Efficient Electric Power Systems*, John Wiley & Sons, Inc., Hoboken, New Jersey, **2004**.

[2] T. B. Johansson, *Renewable Energy: Sources for Fuel and Electricity*, Island Press, Washington, D.C., **1993**.

[3] M. Winter, R. J. Brodd, *Chem. Rev.* **2004**, *104*, 4245.

[4] E. J. Winder, A. B. Ellis, G. C. Lisensky, *J. Chem. Ed.* **1996**, *73*, 940.

[5] D. M. Rowe, *CRC Handbook of Thermoelectrics*, CRC Press, Boca Raton, FL, **1995**.

[6] F. J. DiSalvo, *Science* **1999**, *285*, 703.

[7] T. M. Tritt, M. A. Subramanian, *Mat. Res. Bull.* **2006**, *31*, 188.

[8] http://www.melcor.com/.

[9] T. J. Seebeck, *Magnetic Polarization of metals and minerals*, Abhand. Deut. Akad. Wiss, Berlin, **1822**.

[10] J. C. Peltier, *Ann. Chem.* **1834**, *LVI*, 371.

[11] A. F. Ioffe, *Semiconductor Thermoelements and Thermoelectric Cooling*, Infosearch, London, **1957**.

[12] W. Thomson, *Proc. Roy. Soc. Edinburgh* **1851**, 91.

[13] E. Altenkirch, *Phis. Z.* **1909**, *10*, 560.

[14] E. Altenkirch, *Phis. Z.* **1911**, *12*, 920.

[15] H. J. Goldsmid, *Thermoelectric Refrigeration*, Plenum Press, New York, NY, **1964**.

[16] H. J. Goldsmid, R. W. Douglas, *Br. J. Appl. Phys.* **1954**, *5*, 386.

[17] A. F. Ioffe, S. V. Airapetyants, A. V. Ioffe, N. V. Kolomoets, L. S. Stilbans, *Dokl. Akad. Nauk. SSSR* **1956**, *106*, 931.

[18] http://www.globalte.com/.

[19] J. Yang, T. Caillat, *Mat. Res. Bull.* **2006**, *31*, 224.

[20] G. D. Mahan, J. O. Sofo, *Proc. Nat. Acad. Sci. U.S.A.* **1996**, *93*, 7436.

[21] G. S. Nolas, J. Sharp, H. J. Goldsmid, *Thermoelectrics, Basic principles and new materials developments*, Springer, New York, NY, **2001**.

[22] G. J. Snyder, T. S. Ursell, *Phys. Rev. Lett.* **2003**, *91*, 148301.

[23] N. F. Mott, H. Jones, *The Theory of the Properties of Metals and Alloys*, Dover Publications Inc., New York, NY, **1958**.

[24] D. D. Pollock, *"Thermoelectricity" Theory, Thermometry, Tool*, ASTM Publications, Philadelphia, PA, **1985**.

[25] T. K. Reynolds, J. G. Bales, R. F. Kelley, F. J. DiSalvo, in *Chemistry, Physics, and Materials Science of Thermoelectric Materials, Beyond Bismuth Telluride* (Eds.: M. G. Kanatzidis, S. D. Mahanti, T. P. Hogan), Kluwer Academic/Plenum Publishers, Traverse City, MI., **2002**.

[26] C. Kittel, *Introduction to Solid State Physics*, 7th ed., John Wiley & Sons, Inc., New York City, NY, **1996**.

[27] R. E. Peierls, *Ann. Physik* **1929**, *3*, 1055.

[28] T. L. Hill, *An Introduction to Statistical Thermodynamics*, Dover Publications, Inc., New York, NY, **1986**.

[29] D. G. Cahill, R. O. Pohl, *Ann. Rev. Phys. Chem.* **1988**, *39*, 93.

[30] G. A. Slack, in *CRC Handbook of Thermoelectrics* (Ed.: D. M. Rowe), CRC Press,

Boca Raton, FL, **1995**, pp. 407.
[31] G. D. Mahan, *Solid State Phys.* **1998**, *51*, 82.
[32] A. P. Cracknell, *J. Phys. C:* **1973**, *6*, 826.
[33] R. J. Elliott, *Phys. Rev.* **1954**, *96*, 280.
[34] M. S. Dresselhaus, Y.-M. Lin, O. Rabin, M. R. Black, S. B. Cronin, G. Dresselhaus, in *Chemistry, Physics and Materials Science of Thermoelectric materials: Beyond Bismuth Telluride* (Eds.: M. G. Kanatzidis, S. D. Mahanti, T. P. Hogan), Kluwer Academic/Plenum Publishers, Traverse City, MI., **2002**.
[35] L. D. Hicks, M. S. Dresselhaus, *Phys. Rev. B* **1993**, *47*, 16631.
[36] T. C. Harman, P. J. Taylor, D. L. Spears, M. P. Walsh, *International Conference on Thermoelectrics* **1999**, *18th*, 280.
[37] R. Venkatasubramanian, in *Semiconductors and Semimetals, Recent Trends in Thermoelectric Materials Research III, Vol. 71* (Ed.: T. M. Tritt), Academic Press, San Diego, Ca., **2001**, pp. 175.
[38] R. Venkatasubramanian, E. Slivola, T. Colpitts, B. O'Quinn, *Nature* **2001**, *413*, 597.
[39] G. D. Mahan, L. M. Woods, *Phys. Rev. Lett.* **1998**, *80*, 4016.
[40] A. Shakouri, J. E. Bowers, *International Conference on Thermoelectrics* **1997**, *16th*, 636.
[41] B. C. Sales, D. Mandrus, B. C. Chakoumakos, V. Keppens, J. R. Thompson, *Phys. Rev. B* **1997**, *56*, 15081.
[42] G. S. Nolas, D. T. Morelli, T. M. Tritt, *Annu. Rev. Mat. Science* **1999**, *29*, 89.
[43] C. Uher, in *Semiconductors and Semimetals, Recent Trends in Thermoelectric Materials Research I, Vol. 69* (Ed.: T. M. Tritt), Academic Press, San Diego, Ca., **2001**, p. 139.
[44] B. C. Sales, D. Mandrus, R. K. Williams, *Science* **1996**, *272*, 1325.
[45] A. Borshchevsky, T. Caillat, J. P. Fleurial, *International Conference on Thermoelectrics* **1996**, *15th*, 112.
[46] B. C. Sales, in *Handbook on the Physics and the Chemistry of Rare earths, Vol. 33* (Eds.: J. K. A. Gschneidner, J.-C. G. Bünzli, V. K. Pecharsky), Elsevier Science, Amsterdam, Netherlands, **2003**.
[47] G. S. Nolas, M. Kaeser, R. T. I. Littleton, T. M. Tritt, *Appl. Phys. Lett.* **2000**, *77*, 1855.
[48] J. S. Dyck, W. Chen, C. Uher, L. Chen, X. Tang, T. Hirai, *J. Appl. Phys.* **2002**, *91*, 3698.
[49] X. F. Tang, L. D. Chen, J. Wang, Q. J. Zhang, T. Goto, T. Hirai, *J. Alloys Compd.* **2005**, *394*, 259.
[50] M. Puyet, A. Dauscher, B. Lenoir, M. Dehmas, C. Stiewe, E. Muller, J. Hejtmanek, *J. Appl. Phys.* **2005**, *97*, 083712/1.
[51] G. S. Nolas, J. Poon, M. G. Kanatzidis, *Mat. Res. Bull.* **2006**, *31*, 199.
[52] E. A. Skrabek, D. S. Trimmer, in *CRC Handbook of Thermoelectrics* (Ed.: D. M. Rowe), CRC Press, Boca Raton, FL, **1995**, pp. 267.
[53] D.-Y. Chung, T. Hogan, P. Brazis, M. Rocci-Lane, C. Kannewurf, M. Bastea, C. Uher, M. G. Kanatzidis, *Science* **2000**, *287*, 1024.
[54] D.-Y. Chung, T. P. Hogan, M. Rocci-Lane, P. Brazis, J. R. Ireland, C. R. Kannewurf, M. Bastea, C. Uher, M. G. Kanatzidis, *J. Am. Chem. Soc.* **2004**, *126*, 6414.
[55] K. F. Hsu, S. Loo, F. Guo, W. Chen, J. S. Dyck, C. Uher, T. Hogan, E. K.

Polychroniadis, M. G. Kanatzidis, *Science* **2004**, *303*, 818.
[56] E. Quarez, K.-F. Hsu, R. Pcionek, N. Frangis, E. K. Polychroniadis, M. G. Kanatzidis, *J. Am. Chem. Soc.* **2005**, *127*, 9177.
[57] P. F. P. Poudeu, J. D'Angelo, A. D. Downey, J. L. Short, T. P. Hogan, M. G. Kanatzidis, *Angew. Chem. Int. Ed.* **2006**, *45*, 3835.
[58] T. Fujii, I. Terasaki, in *Chemistry, Physics and Materials science of thermoelectric materials: Beyond Bismuth Telluride* (Eds.: M. G. Kanatzidis, S. D. Mahanti, T. P. Hogan), Kluwer academic/ Plenum publishers, New York, Traverse city, MI., **2003**, p. 71.
[59] I. Terasaki, Y. Sasago, K. Uchinokura, *Phys. Rev. B* **1997**, *56*, R12685.
[60] R. Funahashi, I. Matsubara, H. Ikuta, T. Takeuchi, U. Mizutani, S. Sodeoka, *Jap. J. Appl. Phys. Lett.* **2000**, *39*, L1127.
[61] A. C. Masset, C. Michel, A. Maignan, M. Hervieu, O. Toulemonde, F. Studer, B. Raveau, J. Hejtmanek, *Phys. Rev. B* **2000**, *62*, 166.
[62] K. Koumoto, I. Terasaki, R. Funahashi, *Mat. Res. Bull.* **2006**, *31*, 207.
[63] K. Takada, H. Sakurai, E. T. Muromachi, F. Izumi, R. A. Dilanian, T. Sasaki, *Nature* **2003**, *422*, 53.
[64] Y. Miyazaki, K. Kudo, M. Akoshima, Y. Ono, Y. Koike, T. Kajitani, *Jap. J. Appl. Phys. Lett.* **2000**, *39*, L531.

Chapter 2

2. Experimental methods and property measurements

2.1 Synthetic methods

All samples were prepared under exclusion of oxygen and moisture in an argon filled glove box, by mixing stoichiometric ratios of the starting materials. Since it is important to avoid the presence of oxygen and moisture, the reactions were either sealed under vacuum or prepared under argon flow. The vacuum needed for sealing the samples was obtained by using Edward's rotary oil pump (RV5). The vacuum pressure was in the order of 10^{-3} mbar and measured by Edward's Active gauge controller. There are several methods available to prepare solids and usually the desired final form of the product defines the synthesis method. In this chapter, synthesis methods and techniques for preparation and characterization of samples will be briefly discussed.

2.1.1 Direct (ceramic) method

The most common and widely used method for preparation of solid materials is direct reaction of solid components at high temperature.[1] Solids usually do not react with each other at room temperature even if the products are thermodynamically favored. It is necessary to have high temperature in order to have a proper rate of the reaction. It should be mentioned here that in spite of the fact that elevated temperatures are necessary to initiate the reaction, both thermodynamic and kinetic factors are important. To have a better understanding about solid state reactions, let us consider the solid reaction of two crystals, A and B, with a contact across one face (Figure. 2.1).[1] Without melting, the reaction starts at the points of contact. As the reaction proceeds further, the product will form in the middle

(C) and the components must diffuse through the new phase. In this type of reaction the first step is the formation of nucleation site at the interface of the A and B. This might be a difficult process since it may need some structural reorganization.

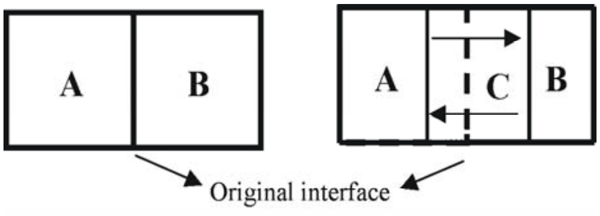

Figure. 2.1 Reaction of two components A and B sharing one face and product layer C after the formation.

After formation of phase C there will be two interfaces available, one between A and C and the second between B and C. The reaction proceeds from this point by counter-diffusion of ions or atoms A and B through the product C. As the reaction proceeds the product layer C is becoming thicker resulting in longer diffusion length and slower rate of reaction. For simple cases, where the rate of the reaction is controlled by lattice diffusion through a planar layer, the rate can be expressed by the equation below:[1]

$$\frac{dx}{dt} = \frac{k}{x}$$

Where x is the thickness of the product layer, t is the time and k is the rate constant. As a general rule in high temperature solid-state reactions, two-thirds of the melting temperature (ºC) of one component should be hot enough to activate the diffusion process of the reaction, but as the reaction proceeds, ions or atoms are usually trapped in appropriate lattice points of the product, needing very high temperatures to get enough energy to diffuse through the product layer.[2] In conclusion, the rate of a solid-state reaction depends on three factors, regardless of the fact that products are thermodynamically favored:

1. the area of contact between the components
2. the rate of nucleation
3. diffusion rates of ions through different existing phases

2.1.2 Chemical vapor transport

In a typical chemical vapor transport reaction, a solid reversibly reacts with a gaseous compound/element to form a gaseous product which undergoes reverse reaction at a different place in the system.[3] The equilibrium between this reaction and the reverse reaction is temperature dependent; hence the vapor phase concentration will change with temperature. This is basically the driving force for mass transport by diffusion from T_1 to T_2.[4] The heterogeneous reaction between a solid and a reactive gas phase, acting like a solvent, offers numerous and interesting results (Figure 2.2).

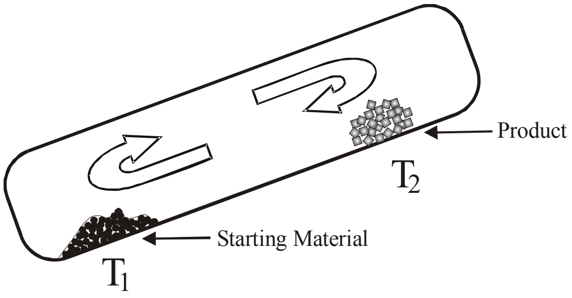

Figure 2.2 A typical chemical transport reaction the arrows show gas motion by thermal convection $T_1>T_2$.

For an exothermic reaction, gas migration is toward the high temperature region, and for an endothermic reaction, gas migration is in opposite direction. The overall chemical vapor transport reaction happens when a gaseous compound is produced at one side and consumed at the other side, where the partial pressure of the gas gives rise to the mass transfer between the two temperature regions. Depending on the materials, different transport agents are possible. In this thesis iodine was used as transport agent in a closed system.

In general, transport reactions in closed systems can be described in four steps:

1. the reaction between starting material and gaseous phase until equilibrium between these two phases is achieved
2. mass transport by gas diffusion to the region with different temperature
3. deposition of the product
4. diffusion of gaseous transport agent back to starting materials

2.1.3 Flux methods

High temperatures are needed to cause sufficient diffusion for a solid-solid reaction to take place in a typical solid-state reaction.[5] Because of high temperature, the reaction proceeds to the thermodynamically preferred products. Since thermodynamically stable compounds are often simple binary or ternary compounds with high lattice energy, they often form first, instead of the desired higher materials. One way to overcome this problem would be to lower the activation energy (E_a) in order to increase diffusion at lower temperature. Lowering reaction temperature in many cases may result in formation of new compounds. Using molten solids (flux) is a common procedure to reduce reaction temperature. Molten solids act like a solvent and reduce reaction temperature. This method is being used since long time for growing single crystal.[6-11] When the flux is used as solvent and simultaneously as reactant, it is called a reactive flux.[12] Salt fluxes are common materials for growing single crystals, in spite of the fact that they usually have high melting points because of their high lattice energies, but eutectic combinations of binary salts often result in lower melting points than typical solid-state reactions. Molten salts have been an important tool for growing large and high quality single crystals and new materials. In recent years, use of molten metals as flux for the synthesis of new materials received special attention.[13-17] These fluxes are primarily used for growing single crystals, but in some cases they acted as reactive fluxes and led to the synthesis of new materials. In order to use a metal as flux, several points have to be considered:

1. the metal should have a reasonably low melting point that can be achieved by normal heating equipment
2. the metal should have large difference between its melting point and boiling point temperatures
3. it should be possible to separate the metal from the product
4. the metal should not form highly stable binary compounds with any of the reactants

2.2 Analysis methods

After synthesis, analysis of products is the most important part of the research. Structural determination can be exhausting and very time consuming. Choosing the right method of analysis will help to save time and result in more accurate structure and property determination. Different analysis methods will be discussed in this section.

2.2.1 X-ray diffraction

Since the discovery of the X-ray by German physics professor Wilhelm Conrad Roentgen (1845-1923)[18] in his laboratory at Würzburg, great interest and developments of possible applications of X-ray have been grown over the years. Discovery of the X-ray has made a revolution in medical sciences and opened a new and important field in structural determination and material characterization for scientists in different fields, especially the chemists and material scientists.[19] In 1912 Laue and his research associates discovered that crystals could diffract X-ray beams.[20, 21] This opened a new door for scientists to investigate different crystals and their structures and gave them the knowledge of atom arrangements in crystals, and made a revolution in modern science, especially in chemistry, solid-state physics and solid-state chemistry. During World War I Debye and Scherrer in Germany and Hull in United States found the diffracted X-ray beam from a finely ground crystalline powder can be used for structural determination of solid powders.[22] The diffraction pattern of a crystal is a transformation of an ordered atomic structure into reciprocal space rather than a direct image of atomic structure. The electrons in atoms scatter X-rays, and Laue defined the relationship between incident and diffracted beam:[23]

$$a(\cos \psi_1 - \cos \varphi_1) = h\lambda$$

$$b(\cos \psi_2 - \cos \varphi_2) = k\lambda$$

$$c(\cos \psi_3 - \cos \varphi_3) = l\lambda$$

a, b and c are the dimensions of the unit cell, $\psi_{1\text{-}3}$ and $\varphi_{1\text{-}3}$ are the angles for the incident and diffracted beams, respectively, from the parallel rows of atoms in three crystallographic directions. h, k and l are Miller indices, integer values that are unique for each diffraction peak, and λ is the radiation wavelength of the incident beam. Based on the Laue equation, sharp peaks can be observed when all three equations are satisfied. More useful information from X-ray powder diffraction can be obtained by using the relationship introduced by Bragg in 1913.[24] According to Bragg, diffraction can be considered to occur from a series of crystallographic planes. This means all planes with identical Miller indices are parallel with inter planar distance d_{hkl}. In order to see reflection from these parallel planes, the incident beam should have a special angle (θ). The relationship between this angle and wavelength of the incident beam is called Bragg's law and can be easily deduced (Figure 2.3).

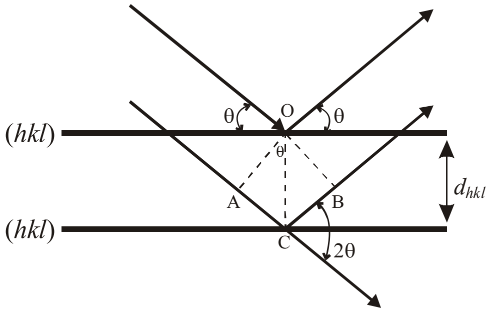

Figure 2.3 Bragg's diffraction condition from parallel *hkl* planes.

Based on simple geometry, ∠AOC=∠BOC= θ, so AC=BC. For positive interference, the phase difference of the two beams must be a multiply of λ, hence 2AC=nλ with n being an integer number. With $\frac{AC}{d} = \sin\theta$, by replacing for AC in this equation one obtains Bragg's law:[25]

$$2d \sin\theta = n\lambda$$

n, the order of the Bragg reflection, is an integer number, which is included in the crystallographic definition of d. Diffraction will be observed when this equation is satisfied and it can happen when d, θ and λ change. Intensity of diffraction depends on the crystal structure and the atoms, i.e., their atomic number and location in the unit cell.

2.2.2 Powder X-ray diffraction (PXRD)

A sample with random orientation of crystals between 0.1 to 10 µm is called a powder sample. When an X-ray beam strikes this polycrystalline sample, the beam is scattered in all directions, with each plane of atoms separated by different lattice spacing in the crystal leading to a cone of diffraction (Figure 2.4).[26]

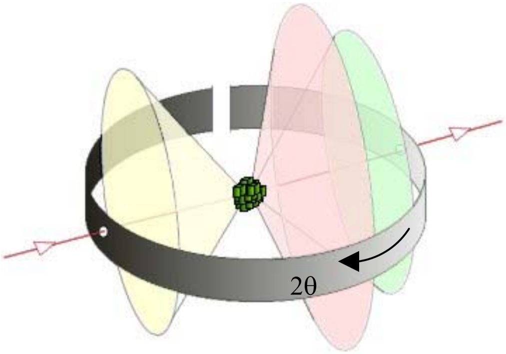

Figure 2.4 Powder diffraction cones produced by a polycrystalline sample.[26]

The diffraction is usually described in reciprocal space by an Ewald sphere, a sphere with radius 1/λ that starts at the origin of the reciprocal space. For each reciprocal lattice point that is located on this sphere, Bragg's law is satisfied and diffraction is observed. In a powder diffraction experiment, diffraction cones are represented as a function of Bragg angle (2θ) for the polycrystalline sample. In order to collect this information as a powder diffraction experiment, the measurements are performed only along a narrow rectangle center (gray shaded area in Figure 2.4) of the equatorial plane of the Ewald sphere. Scattering intensity is usually shown as the total number of accumulated diffraction counts, and all the reflection intensities are relative not absolute (Figure 2.5).[22]

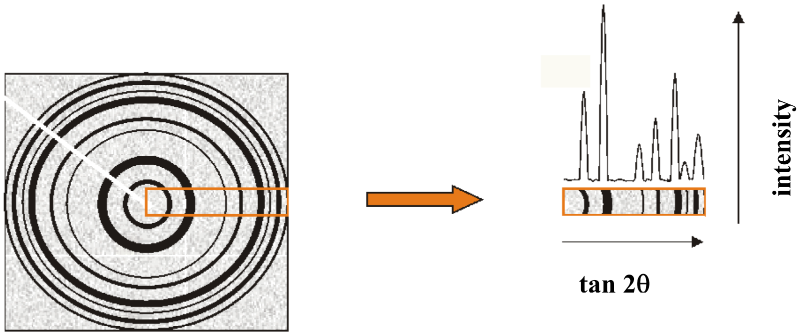

Figure 2.5 The X-ray diffraction pattern recorded on a CCD detector.[27]

Fourier transformation is used to transform diffraction information from direct crystal space into reciprocal space and yield intensity data in reciprocal space. Appropriate detectors will register intensities $I_{(hkl)}$, which are directly proportional to the squares of crystallographic structure factors $F_{(hkl)}$. The intensity is proportional to $|F|^2$:

$$\left|F_{hkl}\right| \propto \sqrt{I_{hkl}}$$

$$F_{hkl} = \sum_{i} f_i exp 2\pi i(hx_i + ky_i + lz_i)$$ [28]

Where f_i is the atomic scattering factor for atom *i*, *hkl* are the Miller indices and *xyz* are the relative atomic positions in the unit cell. In order to perform crystal structure determination not only the absolute value of structure factor ($|F|$), but also the phase of the structure factor is needed. The electron density in a crystal can be explained by:[25]

$$\rho_{(xyz)} = \frac{1}{V}\sum_{h}\sum_{k}\sum_{l} F_{(hkl)} exp - 2\pi\pi(hx + ky + lz)$$

$\rho_{(xyz)}$ is the electron density at the point x, y, z in the unit cell. For polycrystalline samples, the 3-dimensional intensities in reciprocal space are averaged over identical d* values and transformed into a 1-dimensional pattern (Figure 2.5). The detector is an important part of any diffraction analysis system and it measures the position and intensity of diffracted beams. Different kinds of detectors exist. The first and oldest X-ray detector, which was in use for a long period of time, is photographic film. This kind of detector is no longer in common use since the method is time consuming and does not provide high resolution. Other kinds of detectors, which are more commonly used, are position sensitive detectors (PSD) (Figure 2.6), charge coupled devices (CCD) and image plate detectors (IPD).[29] Detectors that cover diffraction in one direction are called line detectors while those that cover the diffractions in two dimensions are called area detectors.

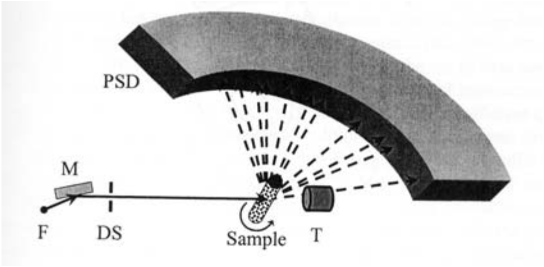

Figure 2.6 The schematic of a typical curved position sensitive detector (PSD).[27]

Positions, intensities and shapes of Bragg's reflections can describe an X-ray powder pattern. These parameters are affected by:

1. space group
2. unit cell parameters
3. types of atoms and their distribution in unit cell

Each parameter mentioned above is affected by properties of the crystal. Unit cell parameters (unit cell dimensions and angles between the axis, $a, b, c, \alpha, \beta, \gamma$) affecting peak positions, coordinates of atoms and their scattering factors (x, y, z, f) affect intensities and crystallinity. Disorders and defects change the peak shapes. All powder X-ray measurements in this thesis were performed by utilizing the INEL powder diffractometer with position-sensitive detector and Cu Kα radiation (Figure 2.7).

Figure 2.7 INEL powder diffractometer (left) with curved position sensitive detector (right).

2.2.3 X-ray Single crystal analysis

X-rays diffracted by the lattice of a crystal produce a pattern that can be analyzed to reveal the nature of that lattice. X-ray diffraction data can be used to determine the locations of atoms within the unit cell of a crystal. A grown crystal of sufficient size and quality can be used in order to obtain accurate information and correct crystal structure. The atom types, connectivity, distances and angles between the atoms in a crystal can be established by this method. There are wide ranges of methods and equipments for single crystal studies. A four-circle diffractometer with an area detector is common equipment for crystal structure study. The combination of these two equipment, results in measuring diffracted X-ray beam intensity as function of the four angles ($2\theta, \phi, \chi, \Omega$) (Figure 2.8).[19]

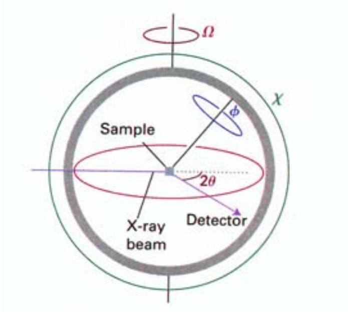

Figure 2.8 Schematic view of a four-circle diffractometer for single crystal analysis.[19]

In the Department of Chemistry at the University of Waterloo, single crystal X-ray diffraction data collection is performed by utilizing graphite-monochromatized Mo Kα radiation (λ=0.71073 Å) on a Bruker Smart APEX CCD diffractometer (Figure 2.9). The SMART[30] software is used for data collection.

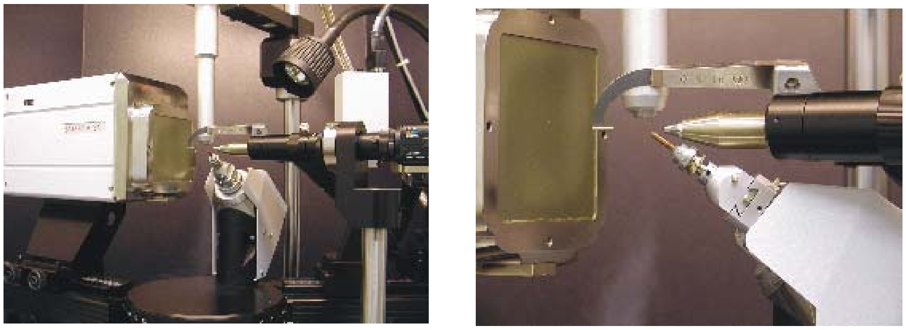

Figure 2.9 Bruker Smart APEX CCD and four-circle diffractometer.

Usually the collected data has to undergo some corrections, this is called data reduction. This process includes two corrections, Lorentz correction (*L*) and polarization correction (*p*).

$$\left|F_{hkl}\right| = \sqrt{\frac{KI_{hkl}}{Lp}}$$

K is scaling factor. The program SAINT[31] is used for cell refinement and data reduction. It is also necessary to apply an absorption correction to the collected data, since most of the structures in this research involve heavy elements, i.e. strong absorbers. The program SADABS[31] is used for absorption correction. After data reduction it is time to start solving the crystal structure. Generally there are two main methods for doing this, Patterson methods and direct methods. Patterson method relies on the presence of a heavy atom in the cell. Since in our systems usually several heavy atoms exist, the chosen method for solving crystal structure is direct method. This method is used when all atoms have similar scattering power. With this method an electron density map of the unit cell can be calculated. Quality of collected data can be evaluated by the internal residual value (R_{int}):

$$R_{\text{int}} = \frac{\sum\left|F_o^2 - F_{o(\text{mean})}^2\right|}{\sum F_o^2}$$

F_o is the observed structure factor. All the crystal structure determinations in this research are being done by using least-square method with the program SHELXTL.[32] In this method allowing for systematic changes of the atomic positions will result in best agreement between calculated and observed structure factor (F_c, F_o). The quality of the refinement is evaluated by the difference between the observed and calculated structure factors, which is called residual factor and usually defined: R_1, wR_2

$$R_1 = \frac{\Sigma \left\| F_o \right| - \left| F_c \right\|}{\Sigma \left| F_o \right|}$$

$$wR_2 = \sqrt{\frac{\sum w(F_o^2 - F_c^2)^2}{\sum w(F_o^2)}}$$

F_o is observed structure factor and F_c is the calculated structure factor and w is the weighting parameter. The goodness of fit (GOOF) is described based on F^2:

$$\mathrm{GOOF} = \sqrt{\frac{\sum w(F_o^2 - F_c^2)^2}{\mathrm{n} - \mathrm{p}}}$$

n and p are the number of reflections and the number of refined parameters, respectively.

2.2.4 Rietveld profile analysis

Improvement of new and existing technologies depends heavily on development and performance of the existing and the new materials. Detailed and accurate information of the crystal structure and the properties of these materials are very important. X-ray single crystal analysis usually provides the most useful information for structural determination, but a good quality crystal with appropriate size is needed for successful and useful structural determination. Growing large and high quality crystals is not always an easy task. Finding a method that can use data collected from powder diffraction experiment, when only small crystals exist, seems to be a useful method. In late 1960s, Dr. Hugo Rietveld[33] proposed a method (he called it profile refinement method), which could use data from powder diffraction experiment and refine the crystal structure by using the least-square refinement method that minimizes the difference between the observed and calculated profiles. This method was initially only applied to neutron data due to their simple peak shape. By using different peak-shape functions such as Lorentzian and pseudo-Voigt instead of just Gaussian functions, application of this method was extended to laboratory X-ray diffractometers by Malmros and Thomas[34]in 1977. It should be mentioned that successful structural analysis by Rietveld method is directly related to the quality of powder diffraction data. For structural refinement by this method, some postulations (a model of crystal structure) are necessary. This model has approximations on unit cell dimensions and atomic coordinates, and it should have the same space group. The refinement will be satisfactory when the best fit between the observed and the calculated model is achieved.[35]

$$S = \sum_i w_i (y_{i(obs)} - y_{i(calc)})^2 = Minimum$$

w_i is weighting factor for each observed point and is equal to $w_i = 1/y_i$. $y_i(obs)$ and $y_i(calc)$ are observed and model calculated intensities at each step for i data points. The computer program for structural analysis and refinement used in this thesis is GSAS (General Structure Analysis System).[36]

2.2.5 Neutron Diffraction

Neutron diffraction can provide the same structural information as X-ray diffraction (electron diffraction). Structural determination for materials that are sensitive to the X-ray beams is being carried by neutron diffraction. Due to the lesser interaction of neutron beam with the solids compared to the X-ray. Since neutrons interact with nuclei of the atoms, the method can be used for identification of light atoms such as hydrogen, or to differentiate between atoms with similar X-ray scattering factors[37] like neighboring atoms. Two methods exist for neutron beam generation, a) by slowing down neutrons generated in a nuclear reactor b) spallation, where accelerated beams of protons are radiated to the nuclei of heavy elements, which results in neutron beam generation.[38] The instrumentation for neutron diffraction is similar to the instrument for X-ray diffraction only in much larger scale (Figure 2.10). Since neutrons carry magnetic spin, they can be used for magnetic property measurements. Moreover because of their electric neutrality they can penetrate deeply and yield information on bulk samples.

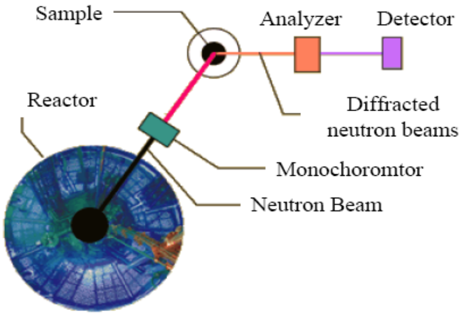

Figure 2.10 Schematic view of neutron diffraction instrument.[39]

Dr. Ian Swainson form NRC, in Chalk River Laboratories performed the neutron measurement discussed in this thesis, and the neutron diffraction data were collected on the C2 constant wavelength (1.32778 Å) diffractometer at room temperature.

2.2.6 Energy Dispersive X-ray (EDX) analysis

One of the useful technologies that come with SEM (Scanning Electron Microscopy) is Energy Dispersive X-ray analysis (EDX), which allows elemental analysis without destroying the sample. When a high-energy electron beam (10-20 kV) hits the atom at the point of contact, secondary and backscattered electrons are emitted from the surface. Secondary electrons leave holes in the electron shell. When electrons from the outer shell drop into these holes in the inner shell, X-rays are generated. The energy of the X-ray beam depends on the material. The energy, wavelength and the shell are unique for each atom.[40] EDX spectrum shows accumulation of the X-ray for each element in its corresponding energy level (Figure 2.11).

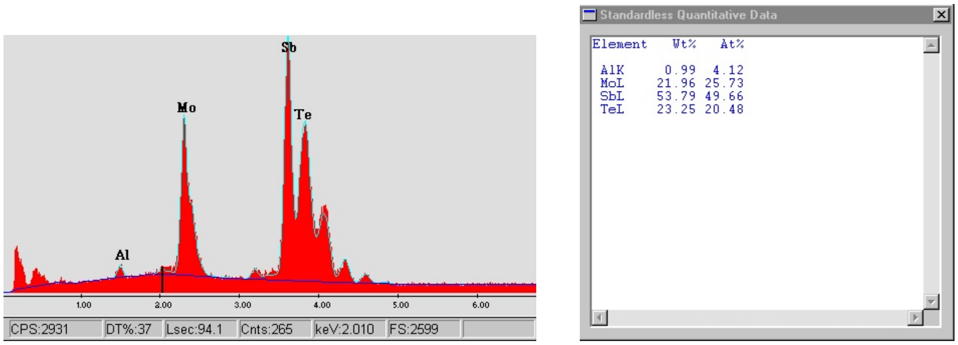

```
Element   Wt%   At%

 AlK     0.99   4.12
 MoL    21.96  25.73
 SbL    53.79  49.66
 TeL    23.25  20.48
```

Figure 2.11 EDX spectrum and quantitative analysis.

Since the X-rays generated are formed by interaction of high-energy electron beams with sample surface, elemental analysis is possible for very small areas of the sample. By calculating the area under the peaks of each identified element and considering accelerating voltage of the beam, quantitative analysis can be performed. The intensity of the EDX spectra represents the concentration of the related element in the testing area. Quantitative analysis can be performed both by a standard or standard less method. The EDX analysis in this thesis has done by using a scanning electron microscope (LEO 1530) integrated with EDX Pegasus 1200.

2.3 Physical property measurements and characterization methods

Physical properties indicate the performance of the materials as possible choice for thermoelectric applications like power generators or cooling devices. Accuracy and consistency in these measurements are vital for thermoelectric characterization of materials. The power factor (σS^2)[41] is usually an indication of performance for thermoelectric materials and can be deduced by measuring electrical conductivity and Seebeck coefficient. Finally thermal conductivity (κ) data are required as well to calculate the figure of merit of a material in different temperatures defined as $ZT = T\frac{\sigma S^2}{\kappa}$. Physical properties for selected samples were carried out on hot-pressed samples at Clemson University. The samples were ground and then pressed into round pellets. Thereafter the samples were hot-pressed utilizing Thermal Technology® HP20-4560-20 machine at high temperature (depends on compound stability) and high pressure. For density measurements, all samples were weighted and their dimensions were measured with a caliper.

2.3.1 Electrical conductivity measurements

The four-point probe method (Figure 2.12) was used for all conductivity measurements.

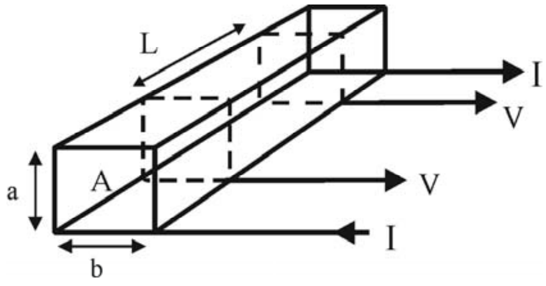

Figure 2.12 Four-point probe method for electrical conductivity measurements.

The sample in powder form was pressed into a bar shape pellet, and four electrical silver wire contacts were attached to the sample by utilizing a silver paint (Leitsilber 200 silver paint, TED PELLA INC.). Then, the pellet was placed in an evacuated chamber, which is cooled by a helium compressor to obtain temperature dependent values for the resistance of the sample. The power source provides the current, which goes through the samples from the two ends of the pellet. The voltage is measured at the two middle contacts. Resistance (R) is calculated by dividing the measured value of the voltage (V) by the current (I). With the known values of dimensions (a, b, L) for the contacts, the specific resistivity (ρ) can be calculated, and the electrical conductivity (σ) is equal to the inverse of the specific resistivity:

$$R = \frac{V}{I} \qquad \rho = R \times \frac{A}{L} \qquad \sigma = \frac{1}{\rho}$$

The electrical conductivity is a function of carrier mobility (μ), carrier concentration (n) and electron charge ($\bar{e}$):

$$\sigma = n\mu\bar{e}$$

For metals, conductivity decreases by increasing the temperature, since the carrier mobility in metals exhibits higher temperature dependence than the number of charge carriers, and the mobility decreases by increasing temperature because of increasing phonon vibration in metals. On the other hand, for semiconductors the number of charge carriers plays a more important role in electrical conductivity. Increasing temperature results in increasing conductivity. This difference results in two different slopes for conductivity of a material. Electrical conductivity measurements of hot-pressed samples were carried out at Clemson University. The samples were measured between 8-310 K using a custom-designed machine.[42] A closed-cycle (crycooler) refrigeration system was used for lowering temperature, and the equipment was connected to a computer via a GPIB connection and LabView® software for automated measurements. Standard four-probe method was used for measurements and the direction of the current is reversed to subtract off any thermal voltages. The sample current was determined by measuring the voltage across a standard resistor in series with the sample.

2.3.2 Hall measurements

The Hall coefficient (R_H) was measured on a Quantum Design PPMS® using a 5-probe configuration[43] at Clemson University. The magnetic field sweeps between ±3.0 Tesla and the R_H is calculated from the slope of the crossways of Hall resistivity vs. magnetic field. The carrier concentration is calculated from:

$$n_C = \frac{N_A}{R_H \times F}$$

where n_C is the charge carrier concentration, N_A is Avogadro’s number and F is Faraday's constant. The Hall mobility is calculated from:

$$\mu = \frac{R_H}{\rho}$$

where R_H is the Hall coefficient and ρ is the specific resistivity.

2.3.3 Seebeck coefficient measurements

The Seebeck coefficient is the ratio of the voltage difference to the temperature difference between the two sides of a material. Thomas John Seebeck discovered this effect in 1821.[44] When a temperature gradient is applied between the two ends of a sample, a voltage will be generated and the ratio of generated voltage to temperature difference is measured as Seebeck coefficient ($S = \frac{\Delta V}{\Delta T}$). All the Seebeck measurements in this thesis were carried out by the SB-100 Seebeck controller from MMR technologies Inc. The pressed rectangular shape sample is placed on a Seebeck stage for measurements (Figure 2.13). The stage has two pairs of thermo-couples, first, silver and a reference and second, silver and sample material.

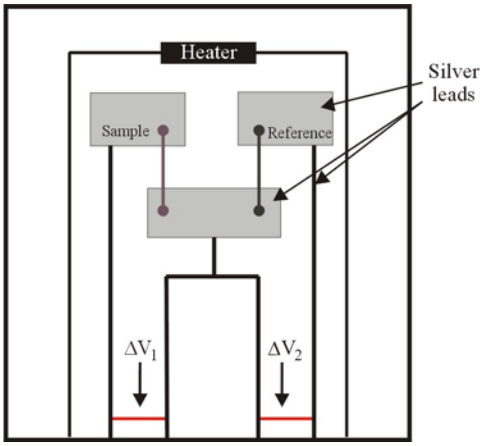

Figure 2.13 MMR Seebeck stage.

A computer controls the temperature on the Seebeck stage via a small heater. The temperature difference that is generated is a function of applied power (P) to the heater. When the power is applied to the heater, the voltage can be measured for the sample and reference, ΔV_1 and ΔV_2, respectively.

$$\Delta V_1 = S_1 \times \Delta T(P) \qquad \Delta V_2 = S_2 \times \Delta T(P)$$

$$S_1 = S_2 \times \frac{\Delta V_1}{\Delta V_2}$$

Usually small temperature differences are used for measurements, causing small values for V_1 and V_2, which result in low accuracy. Also instrumental errors and thermo-voltage effects of wires and connectors should be considered to prevent substantial offset voltages ($\Delta V_1^\circ, \Delta V_2^\circ$). By measuring the sample and the reference at two different temperature offsets using two different powers, P_1 and P_2, and then using the difference signal, this problem can be eliminated:

$$\Delta V_1(P_1) = S_1 \times \Delta T(P_1) + \Delta V_1^\circ \qquad \Delta V_2(P_1) = S_2 \times \Delta T(P_1) + \Delta V_2^\circ$$

$$\Delta V_1(P_2) = S_1 \times \Delta T(P_2) + \Delta V_1^\circ \qquad \Delta V_2(P_2) = S_2 \times \Delta T(P_2) + \Delta V_2^\circ$$

Then S maybe calculated:

$$S_1 = S_2 \times \frac{\Delta V_1(P_1) - \Delta V_1(P_2)}{\Delta V_2(P_1) - \Delta V_2(P_2)}$$

Seebeck coefficient measurements on hot-pressed samples were carried out at Clemson University. The thermoelectric voltages and the temperature gradient were measured by soldering the sample between two copper blocks. A differential thermocouple and a heater were attached to these copper blocks for measuring temperature and applying appropriate voltages. A temperature gradient of 5 K or some percentage of the sample temperature ($\Delta T \approx$

2-5% T) was produced along the length of the sample by a 100Ω chip resistor and measured by a 3 mil AuFe (0.07 at. % Fe) versus Chromel differential thermocouple. The Seebeck coefficient was calculated by the ratio of the thermoelectric voltage to the temperature gradient while zero current was injected.

2.3.4 Thermal conductivity measurements

The property of a material that indicates its ability to conduct heat is called the thermal conductivity. One of the widely used methods in measuring thermal conductivity is flash method for thermal diffusivity measurements. Thermal diffusivity and specific heat (C_v) of a material can be measured by this method. This method was developed in the US radiological defense laboratory by G. L. Abbott.[45] In this technique one face of the sample is radiated by a short laser pulse or xenon flash lamp. An IR detector detects the temperature raise on the other side of the sample (Figure 2.14).

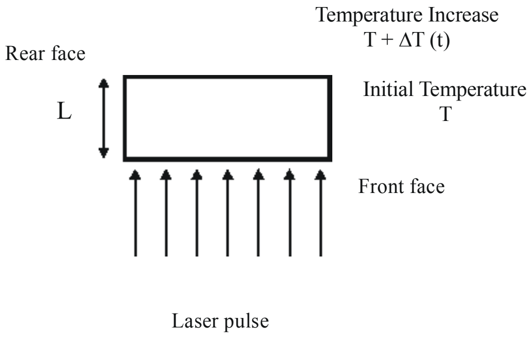

Figure 2.14 Flash method.[41]

The thermal diffusivity (α) can be calculated from the thickness (L) of the sample and the time ($t_{1/2}$) required to reach half of the maximum temperature increase. Dimensionless parameter V is a function of the sample thickness, L, and the time, t:[46]

$$V(L,t) = \frac{T(L,t)}{T_m}$$

where T(L, t) is the temperature at time t with the sample thickness L and T_m is the maximum temperature of the rear face. The second dimensionless parameter is ω:

$$\omega = \frac{\pi^2 \alpha t}{L^2}$$

$$V(L,t) = 1 + 2\sum_{n=1}^{\infty}(-1)^n \exp(-n^2\omega)$$

V can vary from 0 to 1. In practical applications halftime $t_{1/2}$ is used so V=0.5 and ω=1.37. The α can be deduced by:

$$\alpha = \frac{1.37L^2}{\pi^2 t_{1/2}}$$

$$\alpha = 0.1388 \times \frac{L^2}{t_{1/2}}$$

Thermal diffusivity can be measured at different temperatures. When the samples specific heat (C_p) and density (ρ) are known, it is possible to calculate thermal conductivity (κ).

$$\kappa = \alpha \times \rho \times C_p$$

There are two ways to calculate the specific heat:

1. experimental measurements
2. Dulong-Petit law

C_p can be measured by ratio method. The amount of energy required for increasing the temperature of one gram or one mole of a material at constant pressure by one degree is called specific heat.[47]

$$C_p = \frac{dH(T)}{dT} \cdot \frac{1}{m}$$

where dH is the change in enthalpy and dT is the change in temperature. It is possible to measure specific heat by using a standard material with known C_p value. Differential scanning calorimetry measurements for a standard material and sample can be used for C_p measurements by ratio method:

$$C_{p,\,sample} = \frac{m_{standard}}{m_{sample}} \cdot \frac{DSC_{sample} - DSC_{baseline}}{DSC_{standard} - DSC_{baseline}} \cdot C_{p,\,standard}$$

where m is the mass for the sample and the standard.[48] The molar specific heats of most solids are almost constant at high temperatures and this fact is in agreement with Dulong–Petit law on specific heat of solids.[49] Based on Dulong–Petit law, specific capacity of solids at high temperature can be calculated by a simple relationship:

$$C_p = \frac{3R}{M_M}$$

where R is the gas constant ($jmol^{-1}K^{-1}$) and M_M is the molar mass ($Kgmol^{-1}$) of the compound. The thermal conductivity measurements in this study were carried out by Flash Line 3000 thermal diffusivity system from ANTER corp.

Low temperature thermal conductivities of hot-pressed samples were carried out at Clemson University. Thermal conductivity was measured using the steady state technique from 10 K to 300 K using a custom-designed sample puck that plugs into the cold finger of a closed cycle refrigerator.[50] The sample is mounted on a stable temperature copper base, with two #38 Cu-wires attached to the sample using Stycast® epoxy resin on which a 1-mil Cn-Cromega-Cn thermocouple is attached. A 120 Ω strain gauge is attached on the top of the sample with a thin layer of epoxy to provide heating power ($P=I^2R$). The heater current is determined by measuring the voltage across a standard resistor in series with the heater. The resulting temperature gradient (ΔT) is measured using the thermocouple. The base temperature is held to within ±20 mK over the entire measurement sequence. The ΔT is also stabilized to within 20 mK for the ΔT measurement. A power vs. ΔT sweep is performed at each stable temperature (T_0), where the slope of the power vs. ΔT yields the thermal conductance of the material at that temperature ($T=T_0+ ½ \Delta T$). The linearity of the power vs. ΔT curve is examined to ensure the minimum radiation losses. Accurate measurements of the sample dimensions and minimizing the heat loss due to convection, conduction and radiation, will result in precise thermal conductivity values.

2.3.5 Electronic structure and calculations

It is very important for chemists, especially solid-state chemists, to have a good understanding of the properties of condensed materials. The electronic structure of materials includes valuable information that can help to improve and prepare new materials. Solving the Schrödinger equation for many-body wave functions provides insight into the electronic structure of a compound. To do so, appropriate approximations and simplifications need to be applied to this calculation, e.g. Hartree-Fock[51, 52] approximation, Born-Oppenheimer[53] approximation and separated Hamiltonian to independent components. Solving Schrödinger equation for any solid-state material in comparison with molecular calculations seems to be impossible.

It is beneficial to understand the basis of the electronic structure in the molecules before move to the solid-state, where more theories are involved. Molecular orbital (MO) theory is based on the linear combination of atomic orbitals (LCAO). The total number of MO is equal to the total number of atomic orbitals used in their construction. This linear combination of atomic orbitals will result in bonding, antibonding or nonbonding molecular orbitals. Considering a chain of equally spaced hydrogen atoms can help to extend the MO theory toward solids. By using translational symmetry it is possible to write out all of the orbitals for a chain of equally spaced hydrogen atoms with lattice points labeled by index n (n=0, 1, 2, …) (Figure 2.15).

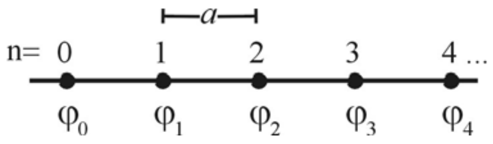

Figure 2.15 Chain of hydrogen atoms.

For every lattice point there is a function (a H 1*s* orbital), φ_1, φ_2, φ_3, etc., with "*a*" as lattice spacing. By considering molecular symmetry and symmetry elements, all molecular orbitals can be found or constructed. The symmetry-adapted functions ψ_k are called Bloch functions:[54]

$$\psi_k = \sum_n e^{ikna} \varphi_n$$

Bloch's theorem uses translational symmetry to generate the crystal wave function in all three crystallographic directions. In this theory, the quantum number *k* is introduced, which defines the reciprocal space. Depending on *k* values, different combinations of orbitals are possible. Figure 2.16 exhibits the two combinations for *k* = 0 and *k* = π/*a*.

$$k = 0 \quad \psi_0 = \sum_n e^0 \varphi_n = \sum_n \varphi_n$$

$$= \varphi_0 + \varphi_1 + \varphi + \varphi_3 + \varphi_4 + \ldots$$

$$k = \frac{\pi}{a} \quad \psi_{\pi/a} = \sum_n e^{\pi i n} \varphi_n = \sum_n (-1)^n \varphi_n$$

$$= \varphi_0 - \varphi_1 + \varphi_2 - \varphi_3 + \varphi_4 - \ldots$$

Figure 2.16 Orbital combination at point *k* = 0 (top) and *k* = π/*a* (bottom).

The *k* value is valid within a part of the reciprocal space called the Brillouin zone. The first Brillouin zone is a Wigner-Seitz cell[55] in the reciprocal space. Wigner-Seitz cell is a geometrical construction used in the study of crystalline materials (Figure 2.17). For constructing the first Brillouin zone, one first chooses a reciprocal lattice point, and then connects it with all nearest points. By connecting all of the planes that cut the vectors in half, a closed volume, the first Brillouin zone, is created within the reciprocal space.

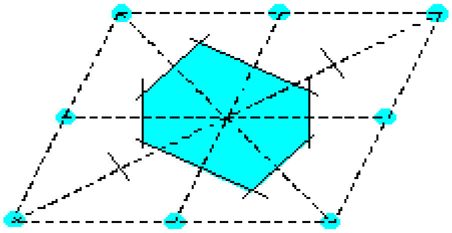

Figure 2.17 Wigner-Seitz cell of a two-dimensional lattice.

Band structure calculations will be possible by letting *k* take all the possible values in the Brillouin zone and represent the band structure in all three dimensions within the Brillouin zone. The shape of the Brillouin zone depends on the Bravais lattice. The special points of high symmetry in the Brillouin zone have their own names (S, R, N, M,…) and are used for band structure calculations.[56] A large number of *k* points will result in more accurate calculations of the total energy of a crystal. Brillouin zones for selected Bravais lattices are shown in Figure 2.18.

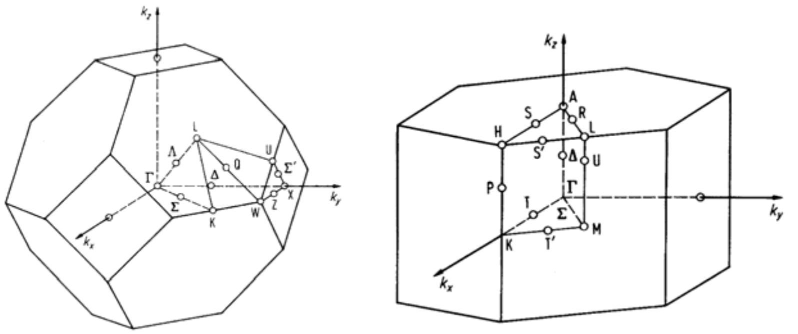

Figure 2.18 First Brillouin zone for face centered cubic (fcc) (left) and hexagonal Bravais lattice (right).

k may adapt values between –π/a and π/a (-π/a ≤ *k* ≤ π/a) in the first Brillouin zone.[57] There is an energy level for each value of *k* (E(*k*)) with a degenerate pair of energy levels for *k* and –*k*. Graphs of E(*k*) vs. *k* are called band structures (Figure 2.19).

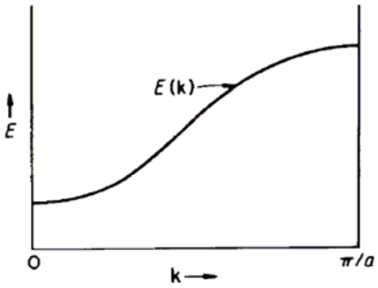

Figure 2.19 Plot of E(*k*) vs. *k* (band structure).[57]

A useful diagram that can be obtained from electronic structure calculations is the density of states (DOS). The density of states diagram is a plot of the number of energy levels, N(E), as a function of energy, E.[58] It is possible to consider one orbital or group of orbitals as the frontier orbitals or the valence orbitals responsible for geometry and reactivity in a molecule. In solids, there are N unit cells (N may be of the order of Avogadro's number) with n number of atomic orbitals, and it is rare that a single orbital or just a small group of orbitals out of N×n orbitals in a solid have the power to direct a geometry or reactivity. One can overcome this problem by considering not just one level but all the levels in an energy range. The density of states is the number of energy levels between E and E+dE.[57] Since the energy levels are along the *k* axis, the DOS can be related to the E(*k*) curves or band structure. The DOS(E) is proportional to the inverse of the slope of E(*k*) (Figure 2.20). This implies that the flat bands have larger DOS than the steep bands.

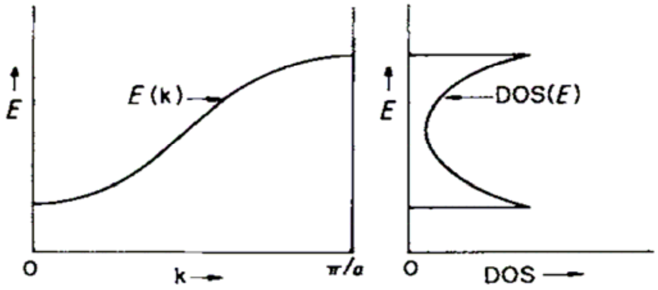

Figure 2.20 Relationship between DOS and band structure for hypothetical chain of hydrogen atoms.[59]

The DOS curve refers to the total number of levels in an infinitesimally small energy range, and the integral of the DOS up to the Fermi level corresponds to the total number of occupied states.

In MO theory, bonding characteristics depend on orbitals interactions. The distribution of an electron in a simple two-center molecular orbital ($\psi = c_1\varphi_1 + c_2\varphi_2$) is given by $|\psi|^2$:

$$\int |\psi|^2 d\tau = 1 = \int |c_1\varphi_1 + c_2\varphi_2|^2 d\tau = c_1^2 + c_2^2 + 2c_1c_2S_{12}$$

$2c_1c_2S_{12}$ is the quantity associated with interaction and it is called the overlap population and was suggested by Mulliken.[60] In the crystal, the sums of all contributions for each atomic orbital for several *k* points in the first Brillouin zone are calculated. The Crystal Orbital Overlap Population (COOP)[61] is the integration of the Mulliken overlap population (MOP)[62] of all states in a certain energy interval. When the overlap integral possesses a positive value, the interaction is bonding and negative, antibonding. Figure 2.21 presents the relationship between the band structure, the DOS and the COOP curves of a simple chain of hydrogen atoms. A specific bond is needed for the calculation of a COOP curve. Considering the interaction between the nearest hydrogen atoms (1 and 2), one can construct the COOP curve for this interaction. The bottom of the band is bonding, the middle nonbonding and the top is antibonding. For a different interaction e.g., between 1 and 3, the interaction is different (the bottom and the top of the band are bonding), as is the COOP curve (dashed line).

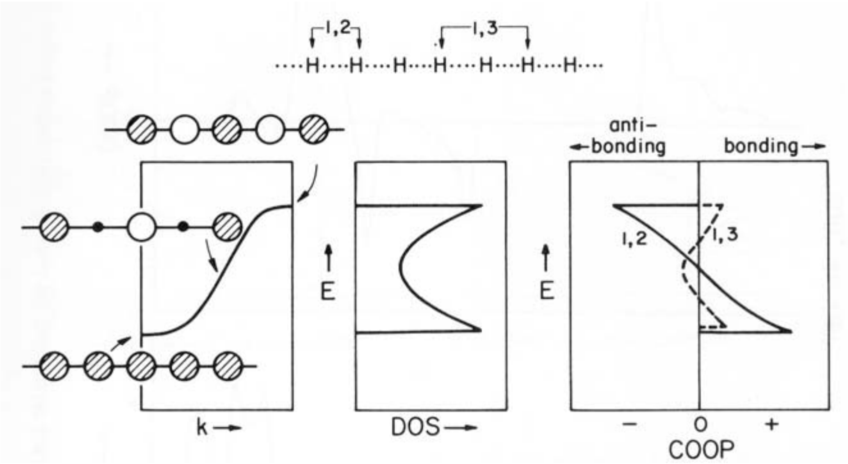

Figure 2.21 Band structure, density of states and COOP curves for a chain of hydrogen atoms.[57]

The intensity of the COOP curves depends on the number of states in that energy range and the magnitude of the overlap. The Crystal Orbital Hamilton Population (COHP) curves[63] and the integrated COHP values (ICOHPs)[64] were also used for investigation of different bond interactions and their strengths in some of the compounds. A COHP curve indicates bonding, nonbonding and antibonding energy regions in a specific energy range while, an integration over all filled states will result in ICOHP values, and these values are in analogy to the Mulliken overlap populations (MOP) obtained from crystal orbital overlap population (COOP) curves. The signs of the ICOHP values are different from MOP. Negative ICOHP values show the bonding character of an interaction; moreover, ICOHP values have units of eV per bond and MOP values units of electrons per bond.

For electronic structure calculations in this research, the Tight-Binding Linear Muffin-Tin Orbital method (TB LMTO) with the Atomic Spheres Approximation (ASA)[65, 66] was used. Therein, the density functional theory is used with the local density approximation (LDA).[67] Since it uses the linear method for calculations, it is much faster than the augmented plane wave approach (APW).[54] The LMTO method is particularly good for close packed structures. The integrations in *k* space were performed by an improved tetrahedron method [68] on *k* points evenly spread throughout the first Brillouin zone.

2.4 References

[1] U. Schubert, N. Hüsing, *Synthesis of Inorganic Materials*, 2nd ed., Wiley-VCH, Weinheim, Germany, **2005**.

[2] A. Wold, K. Dwight, *Solid State Chemisrty, Synthesis structure and properties of selected oxidesand sulfides*, Chapman Hall, New York, NY, **1993**.

[3] W. R. Wilcox, *Chemical vapor transport, secondary nucleation, and mass transfer in crystal growth*, M. Dekker, New York, NY, **1976**.

[4] H. Schäfer, *Chemical transport reactions*, Academic Press, New York, NY, **1964**.

[5] C. E. Housecroft, A. G. Sharpe, *Inorganic Chemistry*, 2nd ed., Pearson Education Ltd., Essex, **2005**.

[6] K. Nakano, H. Hayashi, T. Imura, *J. Cryst. Growth* **1974**, *24/25*, 679.

[7] H. Moissan, *The Electric Furnace*, (translated by A. T. de Mouilpied), Arnold, London, **1904**.

[8] R. H. Deitch, *Crystal Growth*, Pergamon, Oxford, **1975**.

[9] D. Elwell, H. J. Scheel, *Crystal Growth form High-Temperature solutions*, Academic Press, New York, NY, **1975**.

[10] J. Osugi, R. Namikawa, Y. Tanaka, *Rev. Phys. Chem. Jpn* **1967**, *36*, 35.

[11] W. Jeitschko, P. C. Donohue, *Acta Crystallogr. B* **1972**, 1893.

[12] M. G. Kanatzidis, R. Pottgen, W. Jeitschko, *Angew. Chem. Int. Ed.* **2005**, *44*, 6996.

[13] A. C. Payne, A. E. Sprauve, M. M. Olmstead, S. M. Kauzlarich, J. Y. Chan, B. A. Reisner, J. W. Lynn, *J. Solid State Chem.* **2002**, *163*, 498.

[14] T. P. Braun, F. J. DiSalvo, *J. Alloys Compds.* **2000**, *307*, 111.

[15] M. A. Zhuravleva, X.-Z. Chen, X. Wang, A. J. Schultz, J. Ireland, C. R. Kannewurf, M. G. Kanatzidis, *Chem .Mater.* **2002**, *14*, 3066.

[16] V. I. Zaremba, U. C. Rodewald, R. Hoffmann, Y. M. Kalychak, R. Pöttgen, *Z. Anorg. Allg. Chem.* **2003**, *629*, 1157.

[17] H. Hillebrecht, K. Gebhardt, *Angew. Chem. Int. Ed.* **2001**, *40*, 1445.

[18] P. P. Ewald, *Fifty years of X-ray diffraction*, International Union of Crystallography, Utrecht, **1962**.

[19] P. Atkins, T. Overton, J. Rourke, M. Weller, F. Armstrong, *Inorganic Chemistry*, 4th ed., Freeman and company, New York, NY, **2006**.

[20] W. Massa, *Crystal Structure Determination*, 2nd ed., Springer, Heidelberg, **2004**.

[21] M. v. Laue, *Sitz. math. phys. Klasse Bayer. Akad. Wiss.* **1912**.

[22] L. V. Azaroff, M. J. Buerger, *The Powder method in x-ray crystallography*, McGraw-Hill Book company INC., New York, NY, **1958**.

[23] A. R. West, *Solid State Chemistry and its applications*, John Wiley & sons Ltd., Wiltshire, UK, **1997**.

[24] W. L. Bragg, *Proc. Camb. Phil. Soc.* **1913**, *17*, 43.

[25] L. Smart, E. Moore, *Solid State Chemistry, An introduction*, 2nd ed., CHAPMAN & HALL, London, **1996**.

[26] http://www.matter.org.uk/diffraction/x-ray/powder_method.htm.

[27] P. Y. Zavalij, V. K. Pecharsky, *Fundamentals of Powder diffraction and structural charcterization of materials*, Kluwer Academic Publishers, Boston, MA, **2003**.

[28] G. H. Stout, L. H. Jensen, *X-ray Structure Determination, a practical guide*, 2nd ed.,

John Wiley & Sons, Inc., New York, NY, **1989**.
[29] R. Rudman, *J. Chem. Ed.* **1967**, A187.
[30] SMART, 4 ed., Simens Analystical X-ray Instruments Inc., Madison, WI, **1995**.
[31] SAINT, 4 ed., Siemens Analytical X-ray Instruments Inc., Madison, WI., **1995**.
[32] G. M. Sheldrick, *SHELXTL*, Version 5.12 ed., Siemens Analytical X-Ray Systems, Madison, WI., **1995**.
[33] H. M. Rietveld, *J. Appl. Crystallogr.* **1969**, *2*, 65.
[34] G. Malmros, J. O. Thomas, *J. Appl. Crystallogr.* **1977**, *10*, 7.
[35] R. A. Young, *The Rietveld Method*, Oxfor University press, Oxford, **2002**.
[36] A. C. Larson, R. B. von Dreele, Los Alamos National Laboratory: Los Alamos, NM, **2000**.
[37] C. N. R. Rao, J. Gopalakrishnan, *New directions in solid state chemistry*, 2nd ed., Cambridge University Press, New York, NY, **1997**.
[38] C. C. Wilson, *Single Crystal Neutron Diffraction from Molecular Materials*, World Scientific, River Edge, New Jersey, **2000**.
[39] http://www.physik.uni-augsburg.de/exp2/spektroskopie/xas.en.shtml.
[40] http://www.siliconfareast.com/edxwdx.htm.
[41] D. M. Rowe, *Thermoelectrics Handbook, Macro to Nano*, CRC, Boca Raton, FL, **2006**.
[42] A. L. Pope, R. T. I. Littleton, T. M. Tritt, *Rev. Sci. Instrum.* **2001**, *72*, 3129.
[43] H. Zhang, J. He, B. Zhang, Z. Su, T. M. Tritt, N. Soheilnia, H. Kleinke, in *Proc. Materials science & Technology 2006, Vol. II*, MS&T Publication, Cincinnati, OH, **2006**.
[44] T. J. Seebeck, *Magnetic Polarization of metals and minerals*, Abhand. Deut. Akad. Wiss, Berlin, **1822**.
[45] W. J. Parker, W. J. Jenkins, C. P. Butler, G. L. Abbott, *J. Appl. Phys.* **1961**, *32*, 1679.
[46] R. Taylor, in *CRC Hand book of thermoelectrics* (Ed.: D. M. Rowe), CRC Press, Boca Raton, Florida, **1995**, p. 165.
[47] A. Tari, *The Specific Heat of Matter at Low Temperatures*, Imperial College Press, London, **2003**.
[48] J. Blumm, E. Kaisersberger, *J. Therm. Anal. and Calorimetry* **2001**, *64*, 385.
[49] A. T. Petit, P. L. Dulong, *Annal. Chim. Phys.* **1819**, *10*, 395.
[50] A. L. Pope, B. Zawilski, T. M. Tritt, *Cryogenics* **2001**, *41*, 725.
[51] D. R. Hartree, *Poc. Cambridge Phil. Soc.* **1928**, *24*, 89.
[52] V. Fock, *Z. Phys.* **1930**, *61*, 126.
[53] M. Born, J. R. Oppenheimer, *Annl. Phys.* **1927**, *84*, 457.
[54] R. Dronskowski, *Computaional Chemistry of Solid State Materials*, WILEY-VCH, Weinheim, **2005**.
[55] E. Wigner, F. Seitz, *Phys. Rev.* **1933**, *43*, 804.
[56] C. J. Bradley, A. P. Cracknell, *The Mathematical Theory of Symmetry in Solids*, Clarendon Press, Oxford, **1972**.
[57] R. Hoffmann, *Solids and Surfaces: A Chemist's View of Bonding in Extended Structures*, VCH Publishers, Inc., New York, NY, **1988**.
[58] L. Smart, E. Moore, *Solid State Chemistry: an introduction*, Chapman & Hall, London, UK, **1996**.
[59] R. Hoffmann, *Angew. Chem. Int. Ed. Engl.* **1987**, *26*, 846.

[60] J. K. Burdett, *Chemical Bondings in Solids*, Oxford University Press, Inc., New York, NY., **1995**.
[61] T. Hughbanks, R. Hoffmann, *J. Am. Chem. Soc.* **1983**, *105*, 3528.
[62] R. S. Mulliken, *J. Chem. Phys.* **1955**, *23*, 2343.
[63] R. Dronskowski, P. E. Blöchl, *J. Phys. Chem.* **1993**, *97*, 8617.
[64] G. A. Landrum, R. Dronskowski, *Angew. Chem. Int. Ed.* **2000**, *39*, 1560.
[65] O. K. Andersen, *Phys. Rev. B* **1975**, *12*, 3060.
[66] H. L. Skriver, *The LMTO Method*, Springer, Berlin, Germany, **1984**.
[67] L. Hedin, B. I. Lundqvist, *J. Phys. C* **1971**, *4*, 2064.
[68] P. E. Blöchl, O. Jepsen, O. K. Andersen, *Phys. Rev. B* **1994**, *49*, 16223.

Chapter 3

3. Ternary group 4 antimonides

There are two common research strategies in this study. 1. Modifying existing materials to improve their performance. 2. Exploring new materials for potential thermoelectric applications. Good thermoelectric materials are narrow band gap-semiconductors consisting of heavy elements, relatively good electrical conductivity and a moderate Seebeck coefficient.[1] Large numbers of the commercially available materials are antimony and tellurium compounds e.g. $LaFe_3CoSb_{12}$,[2] $Bi_{2-x}Sb_xTe_3$, $Bi_2Te_{3-x}Se_x$, [3] $CsBi_4Te_6$,[4] $AgPb_mSbTe_{m+2}$.[5] Large molar masses and proper electronegativity difference to cation, for these elements make them good candidates for thermoelectric research. As part of our research strategy, the possibility of chemical and structural modification of some existing materials with the properties not appropriate for thermoelectric applications are being investigated. Proper changes (e.g. doping) in crystal and electronic structure of a compound can result in creation of a band gap, size change of an existing band gap or favorable change in transport properties of a material.

Stability at high temperatures, cost efficiency and non-toxicity of oxide materials are some of the attractive features in thermoelectric research. $TiSb_2$[6] is a metallic compound and has poor thermoelectric properties. Modifying structure and properties of $TiSb_2$ by addition of oxygen to make an electron precise compound with possible semiconducting properties was the initial motivation of this research. The metallic property of $TiSb_2$ is the result of the orbital overlap between Sb-5*p* states and Ti-3*d* states. Ideally by introducing the oxygen, the energy of Ti-3*d* states will be raised by mixing with O-2*p* states, which may result in depopulation of Ti-3*d* states and opening a small band gap (Figure 3.1). Several samples were prepared for synthesis of hypothetical electron precise ternary compounds of Ti, Sb and O. Table 3.1 lists some of these reactions.

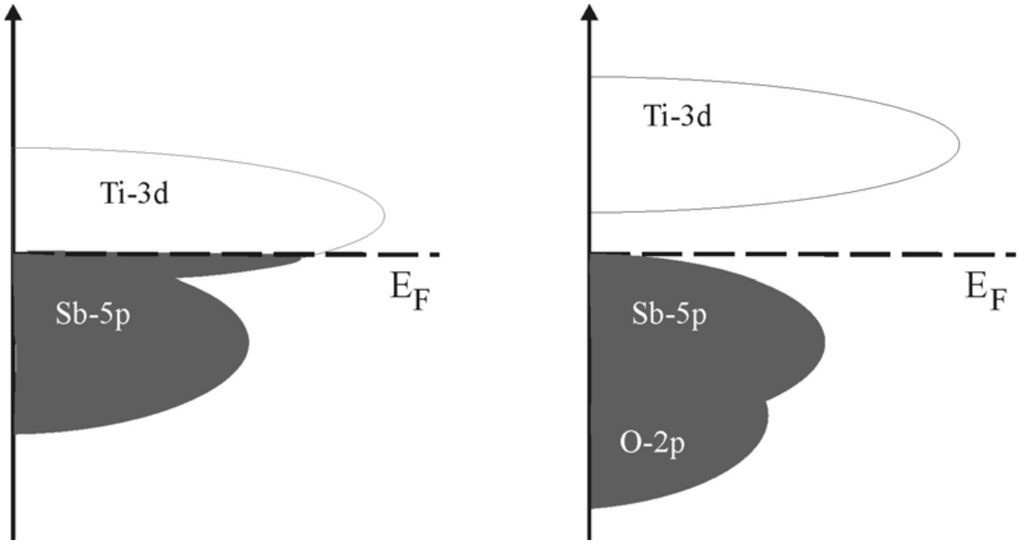

Figure 3.1 Hypothetical effect of O-2p orbital on DOS of $TiSb_2$ (left).

	Starting materials	Target Stoichiometry	Major products
1	$2.125TiO_2$+2Sb+1.375Ti	"$Ti_{3.5}Sb_2O_{4.25}$"	$TiSb_2$, Ti_2O_3
2	$1.75TiO_2$+Sb+0.75Ti	"$Ti_{2.5}SbO_{3.5}$"	$TiSb_2$, Ti_2O_3
3	$2.2TiO_2$+0.4Sb+0.6Ti	"$Ti_{2.8}Sb_{0.4}O_{4.4}$"	$TiSb_2$, Ti_2O_3
4	$1.3TiO_2$+1.6Sb+0.9Ti	"$Ti_{2.2}Sb_{1.6}O_{2.6}$"	$TiSb_2$, Ti_2O_3

Table 3.1 Starting material, target stoichiometry and major phase product of ternary Ti_x Sb_y O_z.

Unfortunately we were not able to prepare any of our target stoichiometries. Changing starting material, reaction conditions and synthesis method did not help for the preparation of our target materials. $ZrSb_2$[7] was the next candidate for the same investigation.

$ZrSb_2$ has been used as starting material for several research projects,[8-10] but it was never investigated as a potential material that can be modified for thermoelectric applications. The so-called α-form of $ZrSb_2$ is the more common phase compared to "β-$ZrSb_2$", which was described to exist as slightly Sb deficient on one of the two Sb sites.[11]

Several samples were prepared for investigation of possible ternary compound of Zr, Sb and O. Table 3.2 lists the target stoichiometry and the major observed phases for each sample.

O: Sb Ratio	Starting Materials	Target Stoichiometry	Major Products
1:4	$3.5Zr + 0.25Sb_2O_4 + 3.5Sb$	“$Zr_{3.5}OSb_4$”	"β-$ZrSb_2$"
1:3	$2.75Zr + 0.25Sb_2O_4 + 2.5Sb$	“$Zr_{2.75}OSb_3$”	α&β-$ZrSb_2$[7, 11]
1:2	$2Zr + 0.25Sb_2O_4 + 1.5Sb$	“Zr_2OSb_2”	"β-$ZrSb_2$"
1:1	$1.25Zr + 0.25Sb_2O_4 + 0.5Sb$	“$Zr_{1.25}OSb$”	$ZrSi_{0.7}Sb_{1.3}$[12]
2:3	$3.25Zr + 0.5Sb_2O_4 + 2Sb$	“$Zr_{3.25}O_2Sb_3$”	"β-$ZrSb_2$"
3:2	$3Zr + 0.75Sb_2O_4 + 0.5Sb$	“$Zr_{3.25}O_3Sb_2$”	$ZrSi_{0.7}Sb_{1.3}$

Table 3.2 List of target stoichiometry and major products for $Zr_xO_ySb_z$.

X-ray powder diffraction revealed "β-$ZrSb_2$" as major phase in several samples and α-$ZrSb_2$ as the second phase in some of the other samples. Since "β-$ZrSb_2$" (TiNiSi type[13]) does not form as the major phase without the presence of oxygen, a single crystal was separated for further investigations. Unfortunately the quality of separated single crystal was not good enough for structural determination. The chemical transport reaction, with iodine as transport reagent, was used to grow single crystals with better qualities. The sample was investigated by EDAX since evidence of tube attack was observed, i.e. the sample reacted with the reaction container (silica tube) containing silicon and oxygen. The obfuscated tube at the bottom where the sample is located is the evidence of this phenomenon. The results of EDAX investigations revealed the presence of Zr, Si and Sb in the ratio of 33:5:62 (in at-%). Single crystal analysis revealed important information on structure and composition of "β-$ZrSb_2$". Synthesis will be discussed first followed by single crystal analysis, structural description and complementary reactions in support of the structural refinement of so-called "β-$ZrSb_2$".

3.1 Synthesis, analysis and crystal structure

3.1.1 Synthesis

A series of reactions were prepared to address the question whether silicon, oxygen or iodine need to be present for the formation of "β-ZrSb$_2$". Table 3.3[14] shows the list of reactions prepared. Different possibilities were considered for preparation of samples; silicon was purposefully added to a sample in exclusion of oxygen and iodine, another sample was prepared without the presence of any other elements. The use of different reaction containers (ceramic crucible) was also investigated. All the samples were prepared by mixing stoichiometric amounts of elements. All elements used were acquired from Aldrich and Alfa Aesar with purities above 99%. The reaction temperatures were in the 650 to 1000 ºC range.

Reaction Number	Starting material	T (ºC)	Major phase	Reaction Container
1	Zr + 0.1Si + 1.9Sb	800	$ZrSi_\delta Sb_{2-\delta}$	Ceramic crucible
2	Zr + 0.2Si + 1.8Sb	1000	$ZrSi_\delta Sb_{2-\delta} + ZrSi_{0.7}Sb_{1.3}$	Silica tube
3	Zr + 0.3Si + 1.7Sb	800	$ZrSi_\delta Sb_{2-\delta} + ZrSi_{0.7}Sb_{1.3}$	Silica tube
4	Ti + 0.1Si + 1.9Sb	700	$TiSb_2$ + Si	Silica tube
5	Hf + 0.1Si + 1.9Sb	800	$HfSb_2$ + Si	Silica tube
6	Zr + 0.2Ge + 1.8Sb	650	$ZrGe_\delta Sb_{2-\delta}$	Silica tube
7	Hf + 0.2Ge + 1.8Sb	700	$HfGe_\delta Sb_{2-\delta}$	Silica tube
8	Zr + Sb	700	α-ZrSb$_2$	Ceramic crucible
9	Zr + Sb	700	α-ZrSb$_2$ + $ZrSi_\delta Sb_{2-\delta}$	Silica tube

Table 3.3 Selected stoichiometries prepared for phase determination.

The TiNiSi type was identified in all reactions with silicon and germanium, independent of the temperature and reaction container and it showed neither oxygen nor iodine was required for its formation. This phase was so called "β-ZrSb$_2$" or "β-HfSb$_2$". On the basis of reactions 2 and 3 in Table 3.3, δ can not reach 0.2. For $\delta \geq 0.2$ two major phases of $ZrSi_\delta Sb_{2-\delta}$ (TiNiSi type[13]) and $ZrSi_{0.7}Sb_{1.3}$[12] (ZrSiS type[15]) were observed. Replacing Zr with Ti and Hf in the Si containing reactions did not lead to the formation of the TiNiSi type. On the other hand we were successful in preparing pure samples of the TiNiSi type with Zr and Hf using Ge instead of Si (reactions 6 and 7). The Ge containing compounds exhibit large phase ranges.

3.1.2 Analysis

X-ray powder diffraction was used for phase determination on all samples. Comparison between experimental powder diagrams with reference powder diagrams was used for phase identifications. Figure 3.2 shows an experimental X-ray powder diagram in comparison with reference powder diagram from the database.

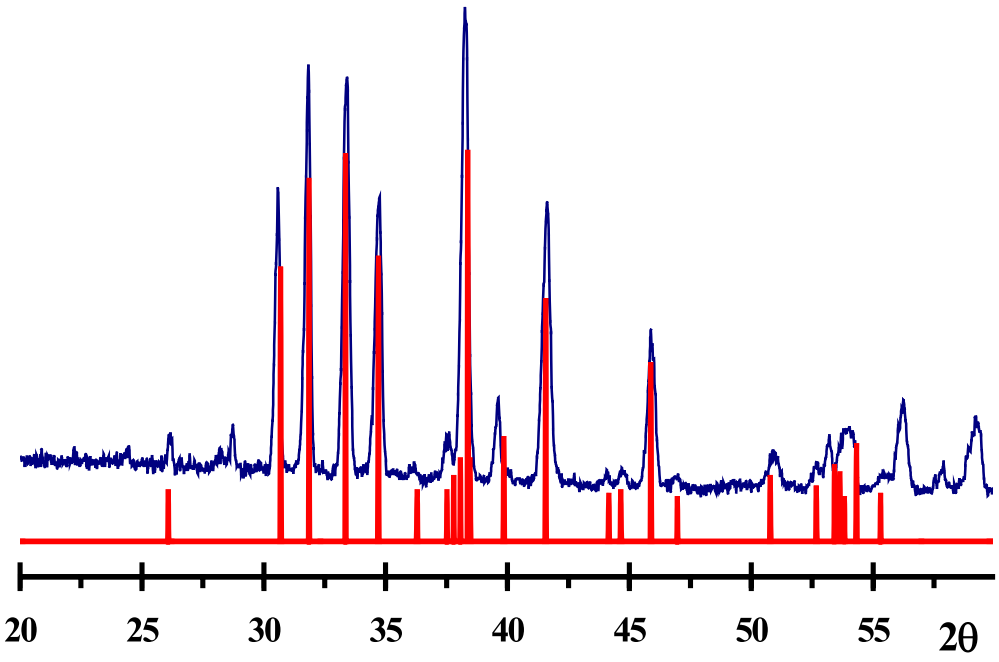

Figure 3.2 X-ray powder diffraction comparison between $ZrGe_{0.2}Sb_{1.8}$ (Blue) and "β-$ZrSb_2$" (Red).

3.1.3 Crystal structure

Four different single crystals were used for this study, one from a transport reaction of Zr and Sb and the other three from the reactions 3, 6 and 7 (Table 3.3). All four cases showed the same space group (#62-*Pnma*), the space group of the TiNiSi type. In the previously published report[11] on the structure of "β-$ZrSb_2$" a deficiency of Sb1 was discussed because of the large thermal parameter. Large temperature factor on Sb1 position is an indication of smaller electron density on that position. The possibility of Sb deficiency was tested for both Sb1 and Sb2 sites in our samples. Evidently the Sb2 site is fully occupied and the uncertainty is on the Sb1 site. Since Energy Dispersive X-ray analysis (EDX) showed the existence of silicon in the crystalline sample, the possibility of mixed Si/Sb on Sb1 site was investigated. The atomic positions published for "β-$ZrSb_2$" were used allowing for mixed Si/Sb and Ge/Sb occupancies, on both Sb sites. In each case the refinements converged to satisfying residual values. The refinement also showed that only one Sb site, Sb1, can incorporate tetrel atoms. Because of this mixed occupancy, this site will be named Q1 (Table 3.4).

atom	site	x	y	z	U_{eq}(Å^2)
Zr	4c	0.2605(2)	¼	0.1630(1)	0.0067(3)
Q1([21.1(5)/78.9] [Ge/Sb])	4c	0.8732(1)	¼	0.0442(1)	0.0091(3)
Sb2	4c	0.9281(1)	¼	0.64544(9)	0.0083(2)

Table 3.4 Position parameters and equivalent displacement parameters for $ZrGe_{0.21}Sb_{1.79}$.

It is noted that the lattice dimensions shrink with increasing Si content (Table A. 2). As for the phase range in case of Si, we could see only a small range for silicon (6.6-11.5%). More crystallographic information can be found in the Appendix. "β-$ZrSb_2$" can only be formed when mixed occupancy between A (A=Si, Ge) and Sb occurs and the results from the addition of A to the binary mixture of Zr and Sb are proofs of this fact. Therefore there is no such binary zirconium antimonide called "β-$ZrSb_2$"; this is actually a ternary phase with general formula of $ZrA_{\delta}Sb_{2-\delta}$ ($HfGe_{0.2}Sb_{1.8}$) with mixed occupancy of A and Sb on one site.

In early 1990s Franzen and Köckerling introduced the concept of mixed occupancy in metal-rich compounds.[16, 17] The DFSO (Differential Fractional Site Occupancy) concept was based on stabilization of materials because of mixed occupancy on metal sites. The DFSO concept was first observed in some metal-rich sulfides ($Nb_{1.72}Ta_{3.28}S_2$,[18] $Nb_{0.95}Ta_{1.05}S$,[19] $Nb_{4.92}Ta_{6.08}S_4$[20] and $Nb_{6.74}Ta_{5.26}S_4$[21]). The ratios of mixed occupancies and the preferred sites, depending on entropic stabilization and bonding capabilities between different metals on different sites will change.[22]

Although examples of anionic DFSO materials are not very common,[23] this concept can be applied to mixing the anionic elements. Mixed occupancy of Se and Te atoms on various sites in different ratios in $Ta_5Se_{1.2}Te_{1.8}$[24] and of Sb and Se in $Zr_7Sb_{1.6}Se_{2.4}$[9] are some of the examples for mixing anionic elements. As for mixed Si/Sb occupancies, two compounds are known, $ZrSi_{0.7}Sb_{1.3}$[12] and $Ti_5Si_{1.3}Sb_{1.7}$[25], while $ZrGe_{0.21}Sb_{1.79}$ and $HfGe_{0.2}Sb_{1.8}$ are the first examples with mixed Ge/Sb occupancies.

There is one independent position for each atom kind in TiNiSi structure type. In case of $ZrA_{\delta}Sb_{2-\delta}$, there is the Zr site, Q1 site for Si/Sb or Ge/Sb mixed occupancy and fully occupied Sb2 site (Table 3.4). Figure 3.3 shows a projection onto the *a*, *c* plane. The zirconium atom is located in a tricapped trigonal prism with four vertices occupied by Q1 and five vertices occupied by Sb2 (Figure 3.4). The Zr–Q1 bonds are significantly shorter than the Zr–Sb2 bonds, a trend not observed in isostructural binary (Co_2Si type[26]) compounds. Also, the Zr–Q1 distances decrease with increasing Si content (Table 3.5). The same trend is also observed for the unit cell volumes that decrease from $ZrSi_{0.06}Sb_{1.94}$ [0.2838(1) nm^3] to $ZrSi_{0.11}Sb_{1.89}$ [0.28014(1) nm^3].

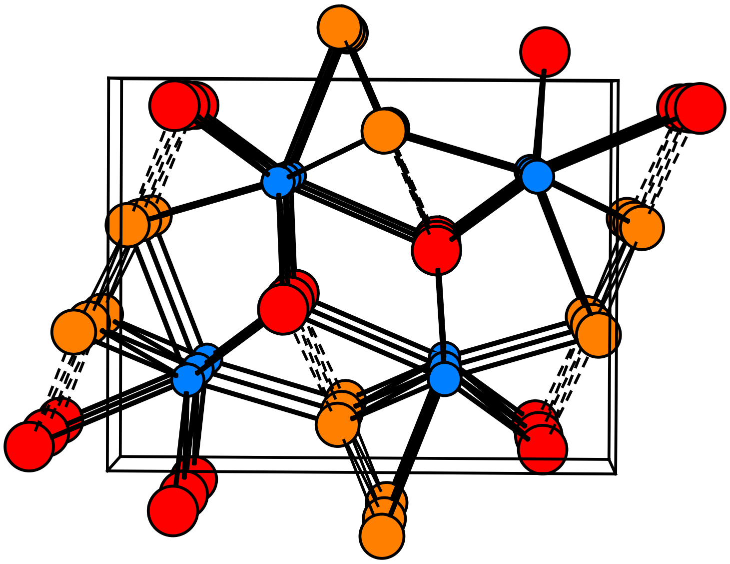

Figure 3.3 Crystal structure of $ZrA_{\delta}Sb_{2-\delta}$ in projection along *b* axis: red circles Sb2, blue circles Zr and orange circles Q1 (A/Sb).

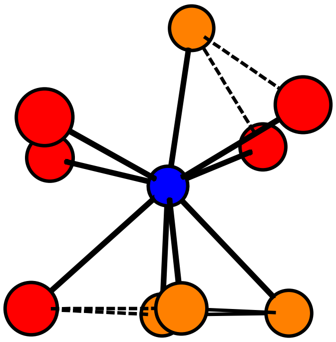

Figure 3.4 Tri-capped trigonal prism around Zr atom.

Distance	no	$ZrSi_{0.07}Sb_{1.93}$	$ZrSi_{0.12}Sb_{1.88}$	$ZrGe_{0.21}Sb_{1.79}$	$HfGe_{0.20}Sb_{1.80}$
M–Q1	1	2.931(2)	2.922(1)	2.922(2)	2.897(2)
M–Q1	2	2.984(1)	2.9722(7)	2.965(1)	2.953(1)
M–Q1	1	3.093(2)	3.076(1)	3.049(2)	3.044(2)
M–Sb2	2	3.038(1)	3.0274(7)	3.017(1)	3.003(1)
M–Sb2	2	3.062(1)	3.0492(7)	3.027(1)	3.022(1)
M–Sb2	1	3.218(2)	3.201(1)	3.198(2)	3.179(2)
Q1–Q1	2	2.886(1)	2.8670(8)	2.838(2)	2.835(2)
Q1–Sb2	2	3.149(1)	3.1350(7)	3.111(1)	3.121(2)

Table 3.5 Selected inter atomic distances (Å) for $MA_{\delta}Sb_{2-\delta}$.

It would be beneficial to have a better understanding about the (α-)$ZrSb_2$ crystal structure. The crystal structure of (α-)$ZrSb_2$ was described by Kjekshus[7] in 1972. There are four crystallographically independent Sb sites (Table 3.6) that create two different substructures.

atom	site	x	y	z	U(Å^2)
Zr1	4m	0.2509(11)	0.5231(19)	0.0	0.28(4)
Zr2	4m	0.0067(11)	0.3277(20)	0.0	0.26(4)
Sb1	4m	0.4414(9)	0.6145(13)	0.0	0.32(5)
Sb2	4m	0.1569(9)	0.8393(14)	0.0	0.33(5)
Sb3	4m	0.1986(8)	0.2320(13)	0.0	0.33(4)
Sb4	4m	0.3978(9)	0.0105(13)	0.0	0.33(5)

Table 3.6 Positional parameters and temperature factors for $ZrSb_2$.

One substructure is an Sb_2 pair; formed by the Sb4 atoms, and the other three Sb atoms form an infinite Sb stripe as second substructure. Figure 3.5 shows the crystal structure of $ZrSb_2$.

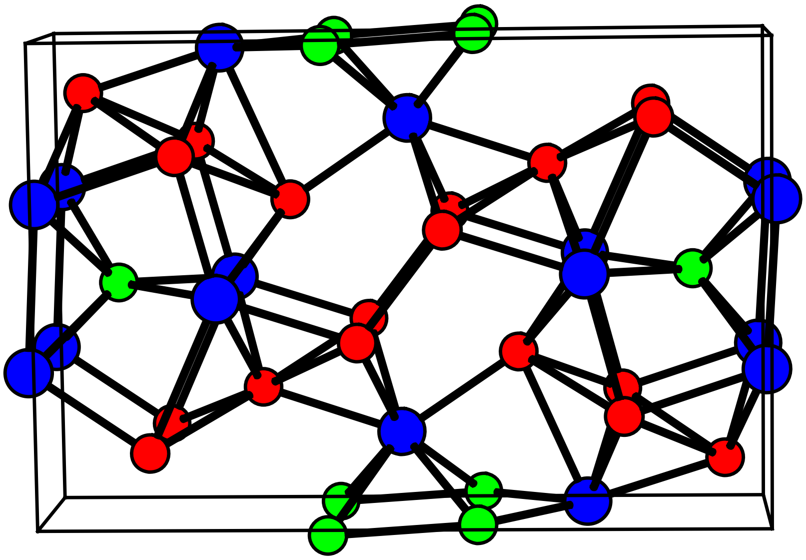

Figure 3.5 Crystal structure of $ZrSb_2$ along c axis, blue circles are Zr; green circles are Sb4 and red circles are Sb1, Sb2 and Sb3.

Bonding in several networks of heavy main group elements was studied and analyzed by Hoffmann et al.[27] This study included the substructure of $ZrSb_2$ and so-called "β-$ZrSb_2$". The Sb_2 pair that is formed by Sb4 atoms in $ZrSb_2$, has a bond of 3.07 Å. Such distances are often referred to as half bonds,[10, 28-30] while single bonds are between 2.80 and 2.90 Å, as in the Zintl compound KSb (2.83-2.85 Å).[31] Considering a half bond for the $(Sb4)_2$ dumbbell (Figure 3.6), and assuming full octet around Sb atoms, each pair of Sb atoms get a charge of -5.

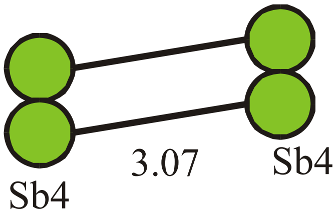

Figure 3.6 Pairs of Sb4 atoms.

The other Sb atoms form an infinite Sb stripe, with inter-atomic distances of 2.88, 3.09 and 3.1 Å, which can be considered as single and half bonds respectively (Figure 3.7).

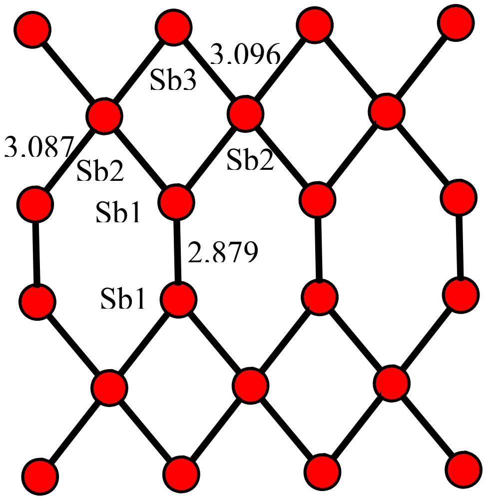

Figure 3.7 Infinite Sb stripe with different Sb–Sb lengths.

Each Sb1 atom participates in one short single bond and two long half bonds, which assign charge of -1 to these atoms. Moreover the Sb2 atom participates in four long half bonds, which assign -1 charge to these atoms as well, and Sb3 participates in two long half bonds with -2 as charge. The overall charge can be considered as $(\mathrm{Zr}^{3.25+})_2\mathrm{Sb1}^{1-}\mathrm{Sb2}^{1-}\mathrm{Sb3}^{2-}\mathrm{Sb4}^{2.5-}$.

For $\mathrm{ZrA}_\delta\mathrm{Sb}_{2\text{-}\delta}$ there are only two atom sites for A and Sb, Q1 (A/Sb) and Sb2 sites. These form a one-dimensional stripe, where each Q1 atom forms two short single bonds to the neighboring Q1 sites (2.84–2.89 Å) and two longer half bonds to the Sb2 sites (3.11–3.15 Å), while the Sb2 atom participates only in two Sb2–Q1 bonds (Figure 3.8).

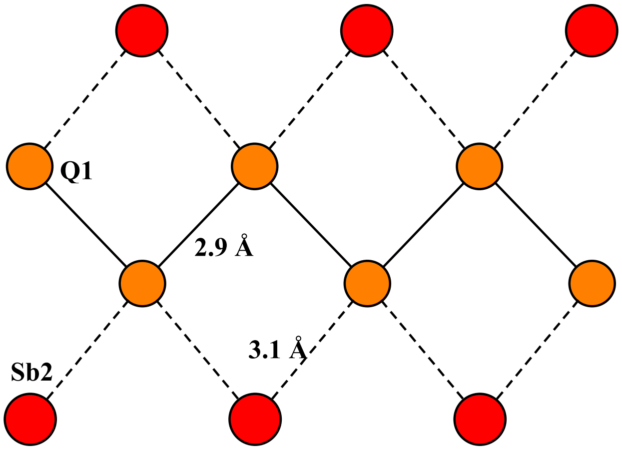

Figure 3.8 Anionic Substructure of $\mathrm{ZrA}_\delta\mathrm{Sb}_{2\text{-}\delta}$ (horizontal: *b* axis).

Assuming the validity of the octet rule, the general formula $\mathrm{Zr}^{2+\delta+}(\mathrm{A}^-)_{\delta^-}(\mathrm{Sb1}^0)_{1-\delta}\mathrm{Sb2}^{2-}$ can be deduced. Although this result is an approximation, it does explain why the tetrel atom (A) prefers the Q1 site, since tetrel atom has fewer valence electrons. It may also explain structural change with larger Sb replacements, since all Q1 sites in ZrSb_2 consist of at least six valence electrons and may thus be less suited for a tetrel atom.

3.2 Electronic structure and physical properties

3.2.1 Electronic structure

To have a better understanding about the electronic structure and differences between the "β-$ZrSb_2$" and $ZrA_{\delta}Sb_{2-\delta}$, density of states were calculated and compared by using the LMTO method. Previous density of states calculations based on the extended Hückel approximation[32, 33] gave comparable results.[11] Calculations were carried out for "β-$ZrSb_2$" and "$ZrGe_{0.25}Sb_{1.75}$". Figure 3.9 shows the density of states for the two structures.

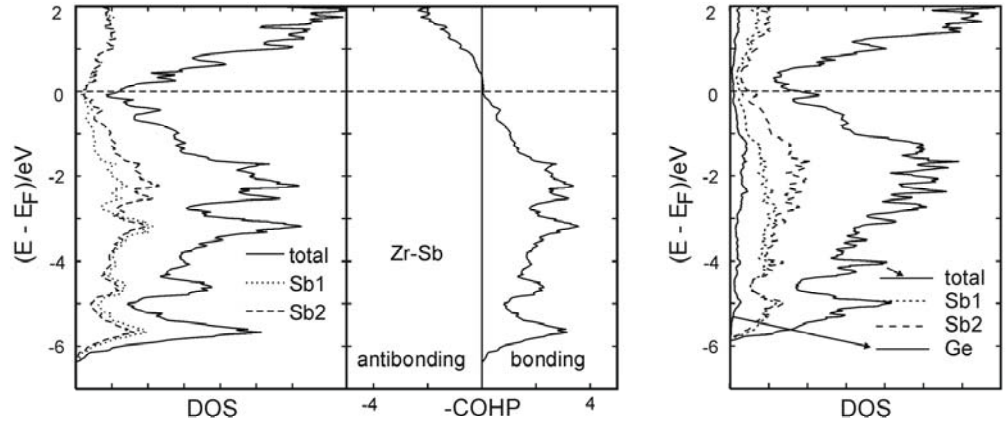

Figure 3.9 Density of states of "β-$ZrSb_2$" with its corresponding Zr-Sb COHP (left) and density of states of "$ZrGe_{0.25}Sb_{1.75}$".

The DOS of "β-$ZrSb_2$" consists of two peaks that overlap. The large peak is dominated by Sb-p states with some Zr contribution from covalent Zr-Sb mixing, which starts below -6 eV and overlaps with Zr-d states. This peak overlap leads to a local nonzero minimum directly at the Fermi level and metallic properties of "β-$ZrSb_2$". A comparison between DOS of Sb1 and Sb2 shows that Sb2 has more valence electrons than Sb1. This is consistent with the valence electron counting mentioned above, yielding five valence electrons for Sb1 and seven for Sb2.

Analysis of the COHP[34] (crystal orbital Hamilton population) curves for "β-ZrSb$_2$" (center of Figure 3.9) reveals a transition between bonding and antibonding character directly at Fermi level for Zr–Sb. This means lowering or raising electron concentration will result in weaker Zr–Sb bonding, if the electronic structure would remain unchanged. Comparing DOS of "β-ZrSb$_2$" and "ZrGe$_{0.25}$Sb$_{1.75}$" reveals the great similarity between the two and hence the validity of the approximation. A shift in the Fermi level from the local nonzero minimum toward the Sb dominated peak can be observed for the DOS of "ZrGe$_{0.25}$Sb$_{1.75}$". Fixing the Fermi level at 0 eV, shows a shift up by about 0.4 eV in DOS of "ZrGe$_{0.25}$Sb$_{1.75}$" compared to the DOS of "β-ZrSb$_2$". Comparing the different bonding interactions of the anionic substructures shows more differences between the two cases. The COHP curves of all different interactions are shown in Figure 3.10.

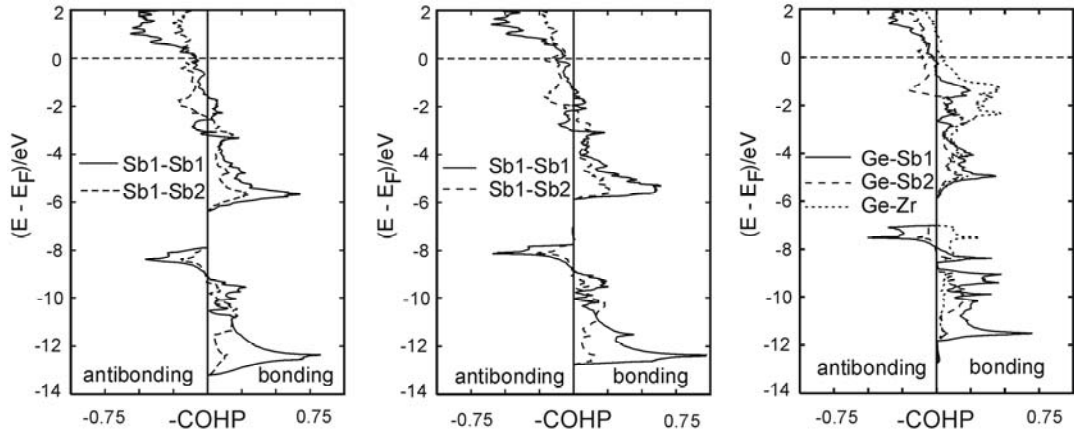

Figure 3.10 The COHP curves of "β-ZrSb$_2$" for Sb–Sb (left), the COHP curves of "ZrGe$_{0.25}$Sb$_{1.75}$" for Sb–Sb (middle) and the COHP curves of Ge–Sb and Ge–Zr for "ZrGe$_{0.25}$Sb$_{1.75}$" (right).

The COHP curves for both Sb–Sb interactions of both cases show that the filled bonding states outweigh the antibonding states. The antibonding states are filled for both Sb-*s* and the Sb-*p* region. For the shorter bond (2.9 Å, solid line), the ratio of filled bonding to filled antibonding states is much higher comparing to the longer bond (3.1 Å, dotted line), and antibonding states occur at the Fermi level in both cases. This means lowering the valence-electron concentration would depopulate the Sb-Sb antibonding states and thus strengthen the bonds. The crystal orbital overlap population (COOP[35]) curves obtained via the extended Hückel calculations,[11] show nonbonding interactions (even slightly bonding) for the Sb1-Sb1 at the Fermi level, in contrast to the COHP analysis for Sb1-Sb1 interactions. Also COOP curves show that Sb-*s* peak is completely bonding, as for COHP curves shows, both filled bonding and antibonding states for Sb-*s* states. The Mulliken overlap population (MOP)[36] for the short Sb1–Sb1 bonds of "β-$ZrSb_2$" (0.43 electrons/bond) is more than twice the MOP of the longer bond (0.17 electrons/bond). The integrated COHP (ICOHP) values show a larger difference between the short and the longer bonds (-1.39 eV for the short bond and -0.45 eV for the longer bond). ICOHP values have typically larger absolute values than MOP's[37, 38] with different units. Bonding character has negative sign for ICOHP values.[39]

The Sb1–Sb1 interactions change by incorporation of Ge atoms into the Sb strip. Higher absolute values of ICOHP (-1.43 and -0.49 eV) indicate fewer filled antibonding states because of the reduced number of valence electrons for "$ZrGe_{0.25}Sb_{1.75}$" compared to "β-$ZrSb_2$". COHP curves of Ge-containing bonds are shifted toward higher energies comparing to Sb1 of "β-$ZrSb_2$". The Ge-*p* peak has maximum around -2 eV, while the Sb-*p* peak is centered around -3 eV, as evident from the Zr–Ge and the Zr–Sb interactions. This can be explained by the lower electronegativity of Ge compared to Sb. The ICOHP values of the Sb–Ge bonds, compared to the Sb–Sb bonds, are of the same order, -1.31 eV for Sb1–Ge and -0.49 eV for Sb2–Ge and -1.43 eV for Sb1–Sb1 and -0.49 eV for Sb2–Sb1. This may explain the possibility of mixing Ge and Sb atoms on one site, despite differences in atomic radii (Pauling [40] radii: r_{Ge}=1.24 Å and r_{Sb}=1.39 Å) and valence electrons.

3.2.2 Physical properties

Physical property measurements can confirm the results form electronic structure calculations. The electrical conductivity (Figure 3.11) and the Seebeck coefficient (Figure 3.13) were measured for $ZrGe_{0.2}Sb_{1.8}$. Both measurements confirmed the metallic behavior of this compound and validity of the results predicted by electronic structure calculations.

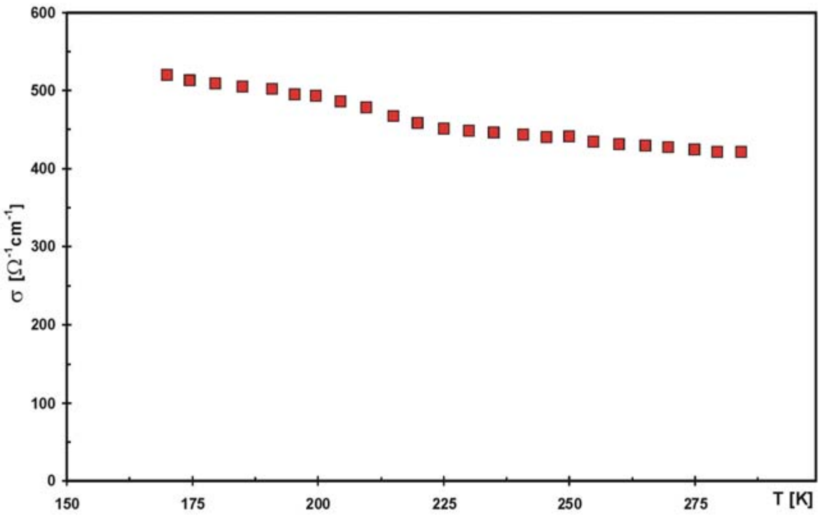

Figure 3.11 Electrical conductivity of $ZrGe_{0.2}Sb_{1.8}$.

Electrical conductivity in metals decrease with increasing temperature. The carrier mobility will decrease by increasing the temperature and carrier concentration is not affected by a temperature increase. This trend is obvious for $ZrGe_{0.2}Sb_{1.8}$, pointing toward metallic behavior as was anticipated. This compound showed a higher absolute resistance value (2.4 mΩcm) compared to elemental zirconium (0.04 mΩcm).

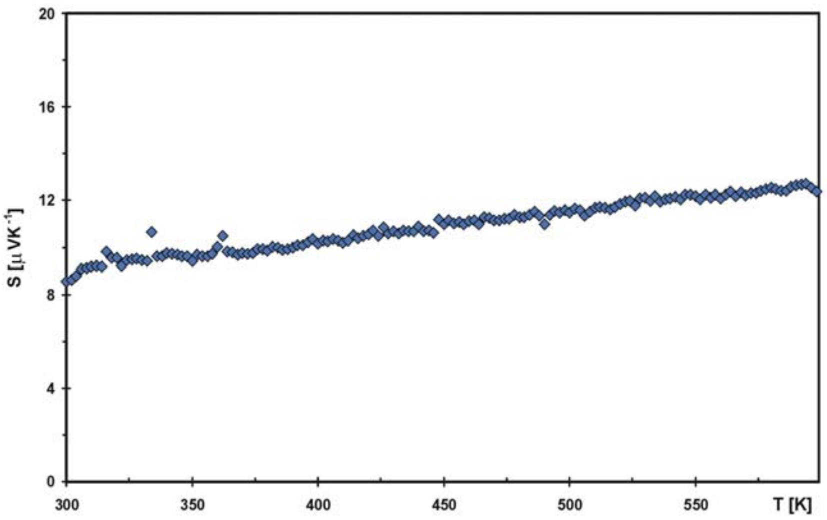

Figure 3.12

Figure 3.13 Seebeck coefficient of $ZrGe_{0.2}Sb_{1.8}$.

Metals usually have small Seebeck coefficient values. The Seebeck coefficient measured for $ZrGe_{0.2}Sb_{1.8}$ (+8.5 to +12.5 μV/K between 300 and 600 K) is another indication of metallic behavior of these compounds.

3.3 References

[1] D. M. Rowe, *CRC Handbook of Thermoelectrics*, CRC Press, Boca Raton, FL, **1995**.
[2] A. Borshchevsky, T. Caillat, J. P. Fleurial, *International Conference on Thermoelectrics* **1996**, *15th*, 112.
[3] G. S. Nolas, J. Sharp, H. J. Goldsmid, *Thermoelectrics, Basic principles and new materials developments*, Springer, New York, NY, **2001**.
[4] D.-Y. Chung, T. Hogan, P. Brazis, M. Rocci-Lane, C. Kannewurf, M. Bastea, C. Uher, M. G. Kanatzidis, *Science* **2000**, *287*, 1024.
[5] K. F. Hsu, S. Loo, F. Guo, W. Chen, J. S. Dyck, C. Uher, T. Hogan, E. K. Polychroniadis, M. G. Kanatzidis, *Science* **2004**, *303*, 818.
[6] M. Armbrüester, R. C. Gil, U. Burkhardt, Y. Grin, *Z. Krist. New Cryst. Struct.* **2004**, *219*, 209.
[7] A. Kjekshus, *Acta Chem. Scand.* **1972**, *26*, 1633.
[8] H. Kleinke, *Chem. Commun.* **1998**, 2219.
[9] H. Kleinke, B. Harbrecht, *Z. Anorg. Allg. Chem.* **1999**, *625*, 1873.
[10] H. Kleinke, *J. Am. Chem. Soc.* **2000**, *122*, 853.
[11] E. Garcia, J. D. Corbett, *J. Solid State Chem.* **1988**, *73*, 452.
[12] R. Lam, A. Mar, *J. Solid State Chem.* **1997**, *134*, 388.
[13] C. B. Shoemaker, D. P. Shoemaker, *Acta Crystallogr.* **1965**, *18*, 900.
[14] N. Soheilnia, A. Assoud, H. Kleinke, *Inorg. Chem.* **2003**, *42*, 7319.
[15] A. J. Klein Haneveld, F. Jellinek, *Recl. Trav. Chim. Pays-Bas* **1964**, *83*, 776.
[16] X. Yao, G. Marking, H. F. Franzen, *Ber. Bunsenges.* **1992**, *96*, 1552.
[17] M. Köckerling, H. F. Franzen, *Croat. Chem. Acta* **1995**, *68*, 709.
[18] X. Yao, H. F. Franzen, *J. Am. Chem. Soc.* **1991**, *113*, 1426.
[19] X. Yao, G. J. Miller, H. F. Franzen, *J. Alloys Compd.* **1992**, *183*, 7.
[20] X. Yao, H. F. Franzen, *J. Solid State Chem.* **1990**, *86*, 88.
[21] X. Yao, H. F. Franzen, *Z. Anorg. Allg. Chem.* **1991**, *598-599*, 353.
[22] K. W. Richter, H. Fritz Franzen, *J. Solid State Chem.* **2000**, *150*, 347.
[23] H. Kleinke, *Trends Inorg. Chem.* **2001**, *7*, 135.
[24] M. Conrad, B. Harbrecht, *Z. Anorg. Allg. Chem.* **1997**, *623*, 742.
[25] H. Kleinke, *Can. J. Chem.* **2001**, *79*, 1338.
[26] S. Geller, V. M. Wolontis, *Acta Cryst.* **1955**, *8*, 83.
[27] G. Papoian, R. Hoffmann, *J. Am. Chem. Soc.* **2001**, *123*, 6600.
[28] H. Kleinke, *Eur. J. Inorg. Chem.* **1998**, 1369.
[29] G. Bolloré, M. J. Ferguson, R. W. Hushagen, A. Mar, *Chem. Mater.* **1995**, *7*, 2229.
[30] G. A. Papoian, R. Hoffmann, *Angew. Chem. Int. Ed.* **2000**, *39*, 2408.
[31] W. Hönle, H.-G. von Schnering, *Z. Kristallogr.* **1981**, *155*, 307.
[32] R. Hoffmann, *J. Chem. Phys.* **1963**, *39*, 1397.
[33] M.-H. Whangbo, R. Hoffmann, *J. Am. Chem. Soc.* **1978**, *100*, 6093.
[34] R. Dronskowski, P. E. Blöchl, *J. Phys. Chem.* **1993**, *97*, 8617.
[35] T. Hughbanks, R. Hoffmann, *J. Am. Chem. Soc.* **1983**, *105*, 3528.
[36] R. S. Mulliken, *J. Chem. Phys.* **1955**, *23*, 2343.

[37] C.-S. Lee, H. Kleinke, *Eur. J. Inorg. Chem.* **2002**, 591.
[38] C.-S. Lee, A. Safa-Sefat, J. E. Greedan, H. Kleinke, *Chem. Mater.* **2003**, *15*, 780.
[39] G. A. Landrum, R. Dronskowski, *Angew. Chem. Int. Ed.* **2000**, *39*, 1560.
[40] L. Pauling, *The Nature of the Chemical Bond*, 3rd ed., Cornell University Press, Ithaca, NY, **1948**.

Chapter 4

4. Ir_3Ge_7 type materials

Most of the compounds with Ir_3Ge_7 structure can be classified as Zintl phases[1] with covalently bonded anionic substructures and unique structural and physical properties.[2] High symmetry crystal structure, heavy elements and cubic void in the crystal structure for accommodating proper "rattlers" are some of the unique features of this structure type. Three members of this structure type, Mo_3Sb_7, $Nb_3Sb_2Te_5$ and Re_3As_7, were investigated for their thermoelectric properties. Results of these investigations are presented in this chapter.

4.1 Synthesis and analysis

All the samples were prepared in an argon-filled glove box. The reactions were carried out in evacuated silica tubes, starting from elements (Mo: powder, -100 mesh, 99.95%, Alfa Aesar; Nb: powder, -325 mesh, 99.8%, Alfa Aesar; Re: powder, -325 mesh, 99.99%Alfa Aesar; Sb: powder, -100, 99.5%, Alfa Aesar; Te: -200 mesh, 99.8%, Sigma Aldrich; Ge: powder, -100 mesh, 99.999% Alfa Aesar; As: lump, 99.999%, Alfa Aesar). The compounds are synthesized by heating the desired stoichiometric ratios of the elements.

Samples of $Mo_3Sb_\delta Te_{7-\delta}$ with $0 \leq \delta \leq 1.6$ were prepared by heating the elemental mixture at 680-700 ºC for a period of 7-10 days in resistance furnaces. The sample was ground and mixed, then put back in the furnace for another 3-4 days for better homogeneity. Sample purity was examined by X-ray powder diffraction using the INEL diffractometer with position sensitive detector. The purity of samples were re-examined by standardless energy dispersive spectroscopy (EDS, LEO 1530, with integrated EDAX Pegasus 1200), and no impurity was observed. Samples with general formula of $A_xMo_3Sb_7$ (A=Mg, Ni, Cu) were also prepared by mixing stoichiometric values of elements. Several block shape to cubic shape single crystals were separated and mounted on glass fibers for single crystal X-ray diffraction studies. The X-ray data were collected with the use of graphite-monochromatized Mo, $K_{\alpha1}$ radiation (λ=0.71073 Å) at room temperature on a BRUKER Smart APEX CCD diffractometer, by scans of 0.3° in ω in two groups of 606 frames at $\phi = 0^{o}$ and 60°.

$Nb_3Sb_{2-\delta}Te_{5+\delta}$ with $-½ \leq \delta \leq ½$ attempted by mixing stoichiometric ratios of elements in evacuated silica tubes. δ values were varied in steps of 0.1. The reaction temperature was between 680-700 ºC. All of the samples were analyzed by X-ray powder diffraction. With $\delta = 0$, the powder diagram showed the pure sample with only the reflections of $Nb_3Sb_2Te_5$. In all other samples either $NbSb_2$ or $NbTe_2$ was found, and annealing for long time at different temperatures did not yield phase pure samples. The pure phase $Nb_3Sb_2Te_5$ was analyzed by standard less energy dispersive spectroscopy and showed homogeneous distribution of Nb, Sb and Te throughout the sample. The crystal structure was determined from a block-shaped crystal of the phase pure sample.

Series of $Re_3Ge_\delta As_{7-\delta}$ samples with $0 \leq \delta \leq 1$ were prepared with δ values varied in steps of 0.2. Preparation of Re and As in sealed silica tube showed evidence of reaction between the sample and the silica tube (obfuscated tube). In order to prevent this problem, all of the samples were prepared by mixing stoichiometric values of elements and pressed in round shape pellets, then placed in a ceramic crucible and sealed in a silica tube under vacuum. The samples were heated for a week between 600-700 ºC. Phase purity of all samples were checked and analyzed by X-ray powder diffraction. The upper limit of Ge is reached when δ=1. For δ >1, the excess germanium was observed as germanium arsenide outside of the ceramic tube, in the silica tube. All attempts to grow a large, high quality crystal for single crystal X-ray structural determination were not successful. It is almost impossible to distinguish between Ge and As with X-ray diffraction since their difference is only one electron, but the neutron scattering length for Re, Ge and As (Re: +9.2 fm, Ge: +8.19 fm, As: +6.58 fm, fm= 10^{-15}m) are significantly different. Thus neutron diffraction was used for accurate structural determination. The neutron diffraction data were collected on the C2 constant wavelength (λ=1.3302 Å) diffractometer at room temperature at Chalk River Laboratories.

4.2 Crystal structure

4.2.1 Mo_3Sb_7, $Mo_3Sb_5Te_2$, Crystal structure

The first member of Ir_3Ge_7 structure type in this study is Mo_3Sb_7. It has a cubic body-centered unit cell with space group $Im\bar{3}m$.[3] The structure contains a three-dimensional Sb atom network with Mo atoms filling square antiprismatic voids in this network. Each Mo atom is connected to eight Sb atoms. Eight Mo–Sb bonds represent the shortest distances in the structure, four Mo–Sb with distance of 2.79 Å and four with 2.81 Å. These bonds are slightly longer than the sum of the single bond radii of 2.68 Å (Pauling[4] radii: r_{Mo}=1.29; r_{Sb}=1.39 Å). The two $MoSb_8$ antiprisms are connected by sharing a square face and making a pair of $MoSb_8$ unit with Mo–Mo distance of 3.00 Å. These $MoSb_8$ pairs are connected to each other by forming intermediate Sb–Sb bonds and making a cubic void of Sb_8 between these pairs. These chains run along all three crystallographic axes (Figure 4.1).[5] In the structure of Mo_3Sb_7, homonuclear bonds between Mo–Mo and Sb–Sb are also present. Table 4.1 shows atomic positions of Mo_3Sb_7.

Atom	Site	*x*	*y*	*z*
Mo	12e	0.3432(2)	0	0
Sb1	12d	¼	0	½
Sb2	16f	0.16220(8)	0.16220(8)	0.16220(8)

Table 4.1 Atomic positions of Mo_3Sb_7.

The Sb1–Sb1 distances in the shared face (dashed lines in figure 4.1) are 3.38 Å, thus much longer than the distances between Sb2–Sb2 atoms (3.1 Å). The parallel running chains are interconnected through the shortest Sb2–Sb2 bond (2.91 Å). Sb–Sb single bonds are usually in the range between 2.8 to 2.9 Å (2.83 to 2.85 Å in Zintl phase KSb[6]) comparable to the short Sb2–Sb2 bond (2.91 Å). The longer Sb2–Sb2 bonds (3.10 Å) are often described as half bonds (one electron per bond).[7-9] The long Sb1–Sb1 distance (3.38 Å) corresponds to a weakly bonding interaction. The common single bond distances for Mo–Mo in compounds such as $MoSb_2Se$ and β-$MoTe_2$[10] are between 2.81 and 2.90 Å. In spite of the long interaction between Mo–Mo in Mo_3Sb_7 (3.0 Å), it is considered as bonding interaction. The distance between the center of the cubic void to the Sb2 atom is 2.69 Å and distance to the Mo atom is 3.25 Å.

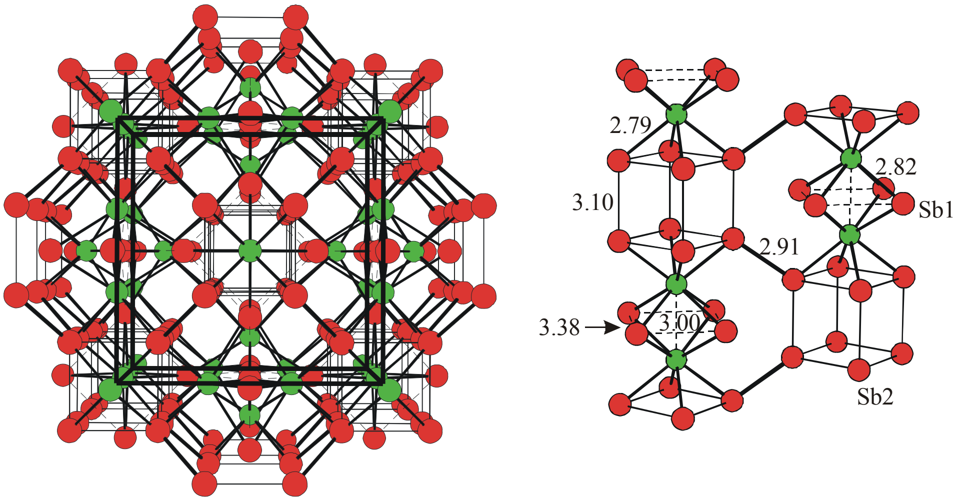

Figure 4.1 Crystal structure of Mo_3Sb_7 (left) onto the *a,b* plane and interconnected chains of $MoSb_8$ square antiprisms (left) and selected bond length. Green circles, Mo; red circles, Sb.

Mo_3Sb_7 with 53 valence electrons is metallic.[2] Replacing two Sb with Te will result in semiconducting ternary compound of $Mo_3Sb_5Te_2$ with 55 valence electrons. Typically for compounds with two anionic constituents of neighboring groups, the atom with the smaller electronegativity prefers the site with more and shorter anion-anion contacts, as may be seen in the NbPS type with its many examples,[11-13] and similarly in the Zintl phases Na_4KGeAs_3[14] and Cs_5GeAs_3[15]. Based on these facts we assume that Sb/Te replacement will happen on the Sb1 position since there are no interactions between the Sb1 atoms. The Sb1 site (Wyckoff notation 12d) was considered as mixed occupied by 50% Sb and 50% Te.

Rietveld refinement resulted in acceptable residual factor proving the partial replacement of Te with Sb on Sb1 site (Table 4.2). Crystal structure of $Mo_3Sb_5Te_2$ is presented in Figure 4.2, highlighting the partially cation-filled cubic void.

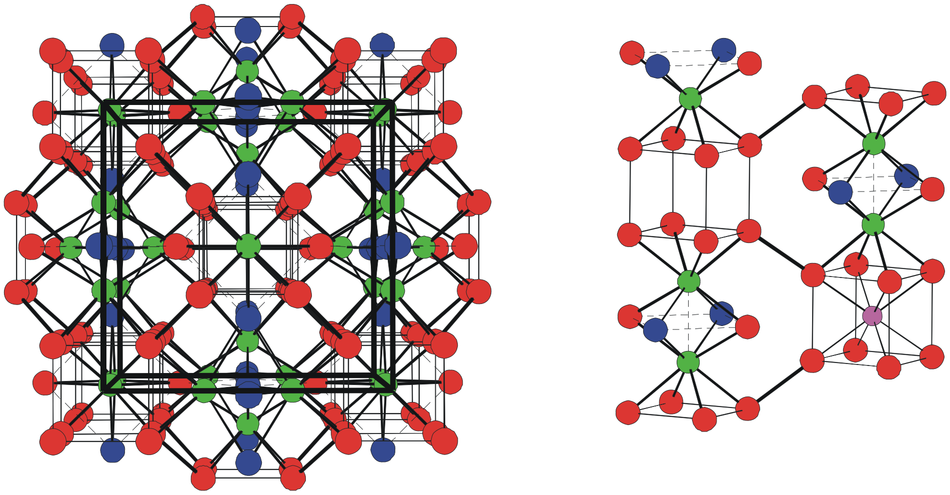

Figure 4.2 Crystal structure of $Mo_3Sb_5Te_2$ (left) and interconnected chains of $MoSb_6Te_2$ square antiprisms with cation (*A*) filled cubic voids (left). Green circles, Mo; red circles, Sb; blue circles, Te; purple circle, cation *A*.

The cubic voids created by Sb2–Sb2 bond, are one of the special features of this structure. They provide a possibility of cation incorporation and creation of rattling for further reduction of lattice thermal conductivity. Cation incorporation results in some structural changes. A list of lattice dimensions and atomic positions as well as occupancies are presented in Table 4.2.[16] Crystallographic data for $A_\delta Mo_3Sb_7$ can be found in Table A. 3.

A	Occupancy (*A*)	*a*(Å)	*x*(Mo)	*x*(Sb2)
Mo_3Sb_7	0	9.559(3)	0.3432(2)	0.16220(8)
$Mo_3Sb_5Te_2$	0	9.536(1)	0.3407(5)	0.1634(2)
Mg	14(4)%	9.5740(7)	0.3433(1)	0.16237(5)
Ni	8(2)%	9.5734(6)	0.3432(2)	0.16235(9)
Cu	8(1)%	9.5829(9)	0.3431(1)	0.16239(4)

Table 4.2 Cell dimensions, atomic positions [*A* on Wyckoff site 2*a*(0,0,0)] and occupancy factors of $A_\delta Mo_3Sb_7$.

In binary Mo_3Sb_7, the distance between each corner and the center of the cube is 2.69 Å. Appropriate cations with reasonable *A*–Sb distance can fit into these cubic voids, e.g. Mg with the shortest Mg–Sb bond in Mg_3Sb_2 (2.82 Å),[17] Ni with Ni–Sb bond in $NiSb_2$ (2.44 Å)[18] and Cu with Cu–Sb bond in Cu_2Sb (2.62 Å).[19] Because of the large distances between *A* and Mo (*A*–Mo 3.28 Å) and *A* and Sb2 (*A*–Sb2 2.69 Å) only small structural changes (slight enlargement of the cell) were observed. The position of both *A* (0,0,0) and Sb1 (¼, 0, ½) are fixed, while the Mo (*x*, 0, 0) and the Sb2 (*x*, *x*, *x*) atoms have one free parameters (Table 4.2). Table 4.3 shows the interatomic distances between atoms for different *A* cations.

Bond	No	no *A*	*A*=0.07 Mg	*A*=0.04 Ni	*A*=0.04 Cu
Mo–Mo	1	2.998(4)	3.001(3)	3.002(4)	3.007(2)
Mo–Sb1	4	2.821(1)	2.8250(7)	2.825(1)	2.8284(6)
Mo–Sb2	4	2.793(2)	2.7986(9)	2.798(2)	2.8005(8)
Sb1–Sb1	2	3.380(1)	3.385(1)	3.385(1)	3.3881(6)
Sb2–Sb2	1	2.907(3)	2.906(2)	2.907(3)	2.908(2)
Sb2–Sb2	3	3.101(2)	3.109(1)	3.109(2)	3.1124(9)
A–Mo	2	–	3.286(1)	3.286(1)	3.2879(6)
A–Sb2	8	–	2.6925(9)	2.692(1)	2.6954(8)

Table 4.3 Interatomic distances (Å) for $A_\delta Mo_3Sb_7$.

4.2.2 $Nb_3Sb_5Te_2$, Crystal structure

The crystal structure of $Nb_3Sb_2Te_5$ was determined from a block-shaped crystal of the phase pure sample. The atomic positions refined for Mo_3Sb_7 were used for the refinement within the space group $Im\bar{3}m$. The Sb2 site (Wyckoff notation 16f) was treated as mixed occupied by 50% Sb and 50% Te to obtain the correct formula, $Nb_3Sb_2Te_5$. The final residual value for this refinement was R1=0.033. To check the Sb/Te ordering, the noncentrosymmetric space group, $I\bar{4}3m$ where the original 16f site is split into two 8c sites, was tested and the residual value (R1= 0.029) was much lower. Table 4.4 shows the atomic positions and thermal displacement parameters of $Nb_3Sb_2Te_5$. Details of crystallographic data for this compound are listed in Table A. 4.

Atom	site	*x*	*y*	*z*	$U_{eq}/Å^2$
Nb	12e	0.3467(9)	0	0	0.0046(2)
Te1	12d	¼	½	0	0.0060(2)
Te2	8c	0.16615(9)	0.16615(9)	0.16615(9)	0.0058(4)
Sb2	8c	0.8366(1)	0.8366(1)	0.8366(1)	0.0070(4)

Table 4.4 Atomic positions and displacement parameters of $Nb_3Sb_2Te_5$.

$Nb_3Sb_2Te_5$ crystallizes in a noncentrosymmetric variant of Ir_3Ge_7 type. The Nb atom is surrounded by eight anions, NbE_8 (E= Sb, Te) in form of a square antiprism. Two NbE_8 units share a square face that consists of Te atoms, resulting in a Nb–Nb bond of 3.089 Å. Figure 4.3 shows the crystal structure of $Nb_3Sb_2Te_5$, chains of Nb_3Sb_2Te and their selected bond lengths. Selected bond lengths for $Nb_3Sb_2Te_5$ are shown in Table 4.5.

Bond	no	distance (Å)
Nb–Sb2	2	2.8716(8)
Nb–Te2	2	2.8854(7)
Nb–Te1	4	2.9001(5)
Nb–Nb	1	3.089(2)
Te1–Te1	2	3.471(1)
Sb2–Te2	1	2.898(1)
Sb2–Te2	3	3.2361(7)

Table 4.5 Interatomic distances in $Nb_3Sb_2Te_5$.

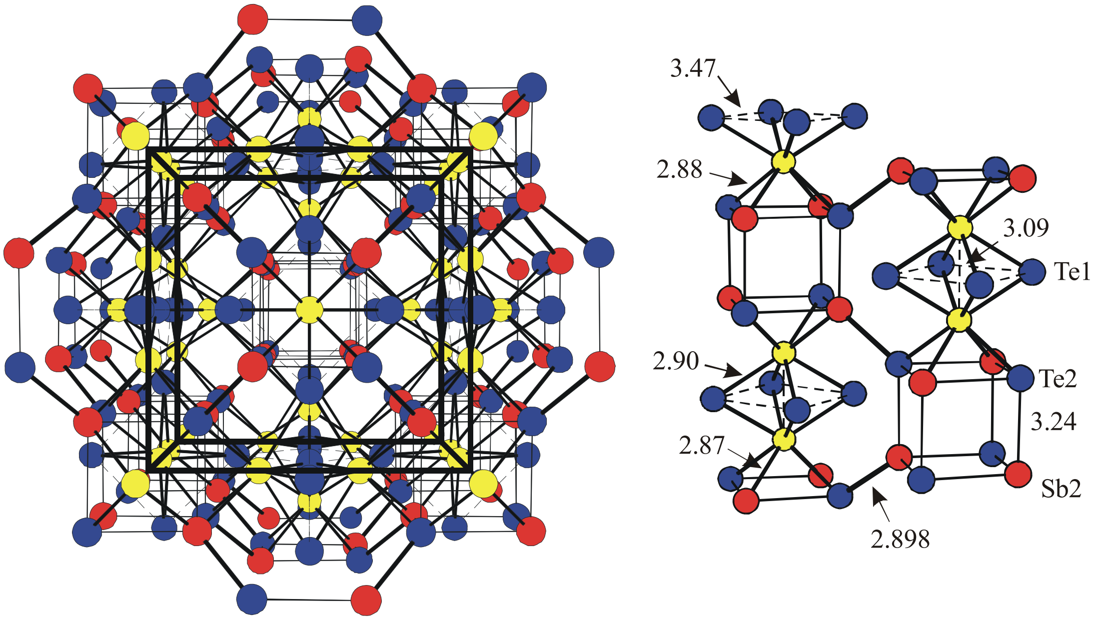

Figure 4.3 Crystal structure of $Nb_3Sb_2Te_5$ onto the *a*, *b* plane and chains of $Nb_3Sb_2Te_5$ with pairs of $NbSb_2Te_6$ square antiprism, yellow circles, Nb; blue circles, Te; red circles, Sb.

All the attempts for preparation of cation intercalated $Nb_3Sb_2Te_5$ were unsuccessful and no phase pure sample was prepared.

4.2.3 Re_3GeAs_6, Crystal structure

$Re_3Ge_\delta As_{7-\delta}$ samples with $\delta = 0$, 0.2, 0.4, 0.6, 0.8 and 1 were synthesized by heating the elements in the desired stoichiometric ratios in evacuated silica tubes. The purity of the products was examined by powder X-ray diffractometer. No sign of side products was detected. All powder diagrams exhibited shifts toward smaller 2θ angles compared to Re_3As_7, referring to the enlargement of the unit cell and confirming the structure type. Because of the small size of the crystals, all attempts for preparation and separation of large crystals for single crystal X-ray analysis were unsuccessful. The neutron diffraction data were collected on the C2 constant wavelength (1.3302 Å) diffractometer for 12 hours at room temperature[20] at Chalk River Laboratories. Structural refinement was carried out by Rietveld method using GSAS[21] on collected neutron diffraction data. Two models were examined for refinement of Re_3GeAs_6. For the first model, Ge atoms share the same position as As1 atoms (Wyckoff position 12d, 33.3% Ge and 66.7% As). The refinement based on this model resulted in R_p=3.78% (Table 4.6).

Atom	site	*x*	*y*	*z*	U_{eq}/Å^2	occ.
Re	12e	0.3417(2)	0	0	0.0016(3)	1
E1	12d	¼	0	½	0.0110(5)	0.333Ge 0.667As
As2	16f	0.1661(2)	0.1661(2)	0.1661(2)	0.0033(5)	1

Table 4.6 Atomic positions and displacement parameters for Re_3GeAs_6based on Ge/As mix occupancy on E1 site.

As for the second model, Ge atoms share the same position as As2 atoms (Wyckoff position 16f, 25% Ge and 75% As) with R_p=3.58% (Table 4.7).

Atom	site	*x*	*y*	*z*	$U_{eq}/Å^2$	occ.
Re	12e	0.3413(2)	0	0	0.0017(3)	1
As1	12d	¼	0	½	0.0054(5)	1
E2	16f	0.1663(2)	0.1663(2)	0.1663(2)	0.0073(4)	0.25Ge 0.75As

Table 4.7 Atomic positions and displacement parameters for Re_3GeAs_6based on Ge/As mix occupancy on E2 site.

The refinement based on second model (Figure 4.4) shows smaller residual factor and reasonable displacement parameters ($\frac{U_{As1}}{U_{E2}} = 0.74$ compared to $\frac{U_{E1}}{U_{As2}} = 3.33$ in the first model). Crystallographic data for Re_3GeAs_6 can be found in Table A. 5. All attempts to refine occupancies failed.

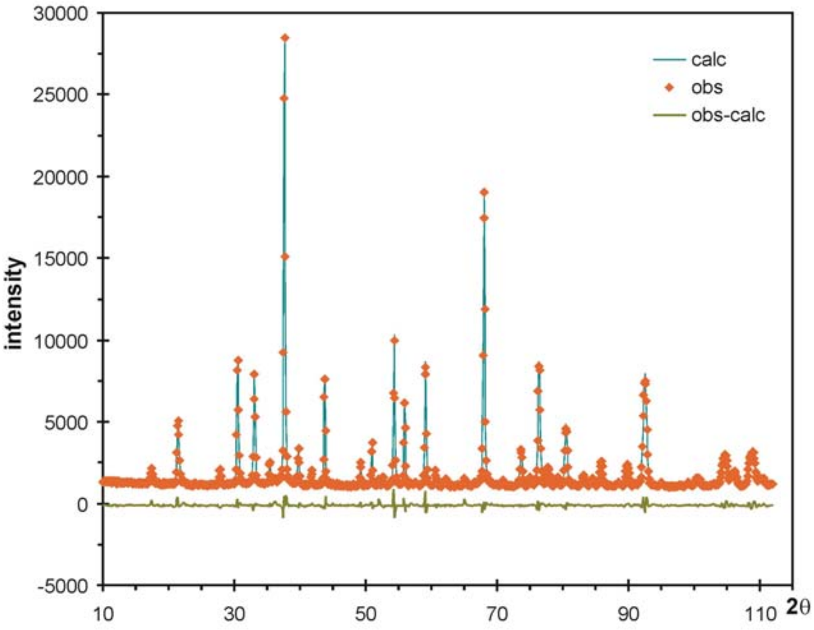

Figure 4.4 Rietveld refinement with neutron data for Re_3GeAs_6.

Re_3GeAs_6 has cubic structure with space group *Im*$\bar{3}$*m*, isostructural with Mo_3Sb_7 (Figure 4.1). Crystal structure of Re_3GeAs_6 is presented in Figure 4.5.

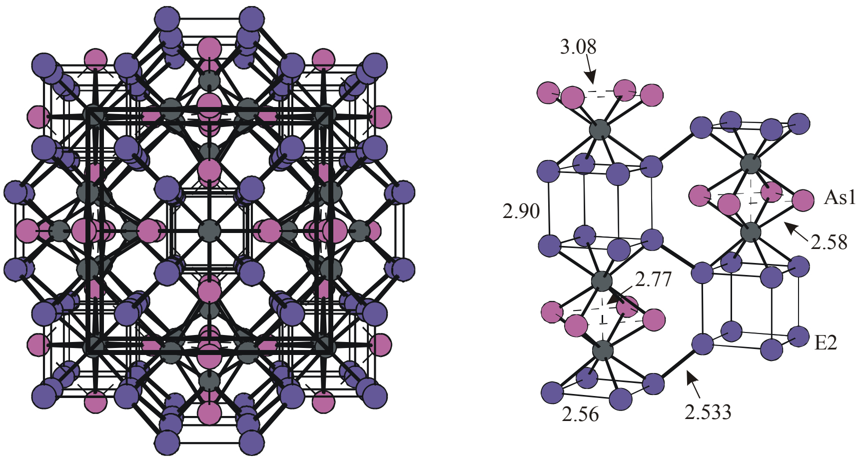

Figure 4.5 Crystal structure of Re_3GeAs_6 (left) and chains of Re_3GeAs_6 (right). Re, grey circles; As1, purple circles; E2, blue circles.

The E2–E2 bond, connecting two chains, is the shortest bond in the structure (2.53 Å), and it is slightly longer than single bond between Ge and As (Pauling single bond radii, Ge=1.24 Å and As=1.21 Å). There are weak interactions between As and Ge atoms. The distance between the Re atoms is long (2.77 Å compared to 2.63 Å for Re–Re single bond in $Re_6Se_8Te_7$[22] or 2.68 Å in Re_2Te_5[23]) but they have stronger interactions (ICOHP= -1.678 eV Table 4.13) compared to Mo–Mo in Mo_3Sb_7 (3.00 Å compared to 2.81 Å for Mo–Mo single bond in $MoSb_2Se$[24] and 2.90 Å in β-$MoTe_2$[10] with ICOHP= -1.235 eV). Selected bond lengths for Re_3GeAs_6 can be found in Table 4.8.

Bond	No	distance (Å)
Re–Re	1	2.772(4)
Re–As1	4	2.586(1)
Re–E2	4	2.560(2)
As1–As1	2	3.08716(3)
E2–E2	1	2.533(5)
E2–E2	3	2.904(3)

Table 4.8 Interatomic distances in Re_3GeAs_6.

The unit cell of Re_3GeAs_6 (a= 8.73180(7) Å) is slightly larger than Re_3As_7 (a= 8.7162(7) Å), which may be a consequence of Ge being larger than As (Pauling radii, Ge=1.24 Å and As =1.21 Å). The distance between the center of the cubic void and E2 atoms of the cube is large enough (2.52 Å) to accommodate a number of cations (Mg^{2+}, Fe^{2+}, Co^{2+}, Ni^{2+},…) for possible further lowering of the thermal conductivity. A Rietveld refinement based on X-ray data was also carried out for $Re_3Ge_{0.6}As_{6.4}$ to confirm the structure and yield an acceptable R_p value (8.37%). Atomic positions and occupancies (unrefined) are shown in Table 4.9.

Atom	site	*x*	*y*	*z*	U_{eq}/Å^2	occ.
Re	12e	0.3407(2)	0	0	0.0128(5)	1
As1	12d	¼	0	½	0.0129(9)	1
E2	16f	0.1659(2)	0.1659(2)	0.1659(2)	0.0162(9)	0.15Ge 0.85As

Table 4.9 Atomic positions and displacement parameters for $Re_3Ge_{0.6}As_{6.4}$.

Rietveld refinement based on X-ray data for $Re_3Ge_{0.6}As_{6.4}$ (Table A. 6) is shown in Figure 4.6. The X-ray data were collected on INEL powder diffractometer with position sensitive detector at room temperature for 16 hours.

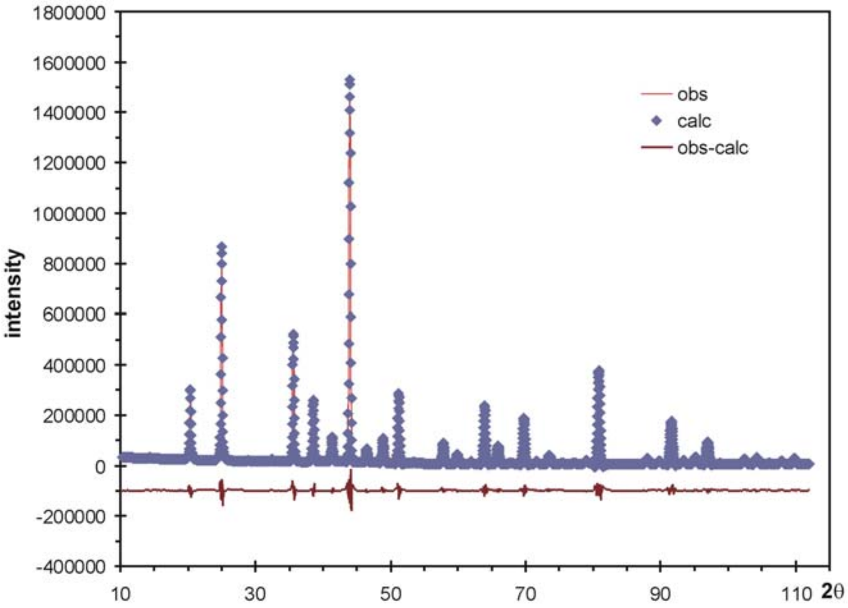

Figure 4.6 Rietveld refinement with X-ray data for $Re_3Ge_{0.6}As_{6.4}$.

4.3 Electronic structure

4.3.1 Electronic structure of Mo_3Sb_7 and $Mo_3Sb_5Te_2$

Electronic structure calculation for Mo_3Sb_7 clearly shows the metallic nature of this compound. Several bands cross the Fermi level, E_F, showing the metallic behavior of Mo_3Sb_7 (Figure 4.7).[5] The existence of a band gap just above the Fermi level and presence of numerous flat bands around the Fermi level are some of the interesting features of this compound that make it an attractive material for thermoelectric research.

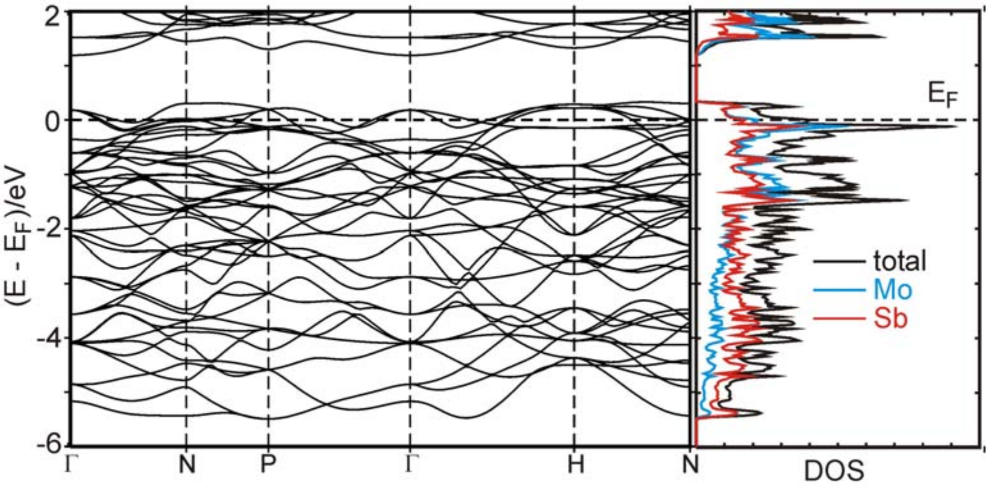

Figure 4.7 Density of states (DOS) (left) and band structure (right) of Mo_3Sb_7.

The size of the gap just above the Fermi level (E_F) is around 0.9 eV. Both atoms, Mo and Sb, contribute significantly to the density of states around the Fermi level. The Mo *d* states are major contributors to the bands around the Fermi level, as well as the Sb *p* states to a lesser extent. The Sb contributions are mostly located well below Fermi level. The COHP curves (Figure 4.8) clearly show that Mo–Sb have the strongest interactions, compared to Mo–Mo and Sb–Sb interactions.

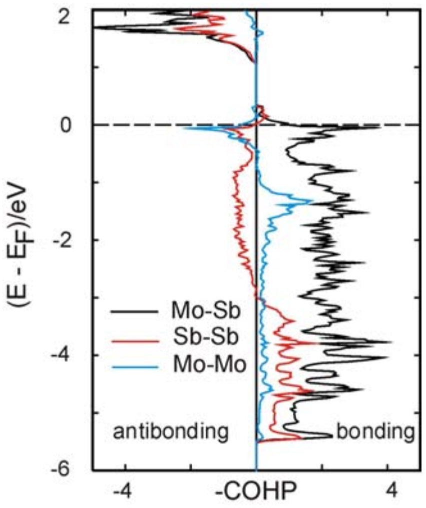

Figure 4.8 Crystal Orbital Hamilton Population (COHP) Curves for Mo_3Sb_7.

Bonding and antibonding states for homonuclear interactions below Fermi level are filled. The COHP curves also show that only bonding states for Mo–Sb interactions are filled. Table 4.10 shows different interaction distances and their ICOHP values. The negative ICOHP values for all interactions show the bonding nature of the bonds.

Bond	no	distance (Å)	ICOHP (eV)
Mo–Mo	1	2.998	-1.2347
Mo–Sb1	4	2.821	-1.7059
Mo–Sb2	4	2.793	-1.9483
Sb1–Sb1	2	3.380	-0.0838
Sb2–Sb2	1	2.907	-0.7776
Sb2–Sb2	3	3.101	-0.4503

Table 4.10 Bond distances and ICOHP values for Mo_3Sb_7.

Increasing valence electron in Mo_3Sb_7 will result in raising the Fermi level into the band gap and increase bonding between Mo and Sb, and Sb and Sb atoms by filling more bonding states. On the other hand filling antibonding states of the Mo–Mo interactions will result in a weaker Mo–Mo bonding. Elongation of the Mo–Mo bond (3.05 Å compared to the 3.00 Å in Mo_3Sb_7) after partial replacement of Sb with Te supports this prediction. Similarity of Sb and Te is an advantage that one can use to increase the valance electrons in Mo_3Sb_7.

They both have very similar sizes (Pauling radii, Sb: 1.39 Å; Te: 1.37 Å) and partial replacement of Sb with Te will not affect the band dispersion very much. Because of higher electronegativity of Te, the positions with weaker interaction between the two atoms were chosen for electronic structure calculation of $Mo_3Sb_5Te_2$ (Sb1 position). Introducing Te atoms in this model destroys the 3-fold rotation axis and reduces the symmetry to tetragonal crystal system with space group *I*4/*mmm*. Band structure and density of states for $Mo_3Sb_5Te_2$ are shown in Figure 4.9.

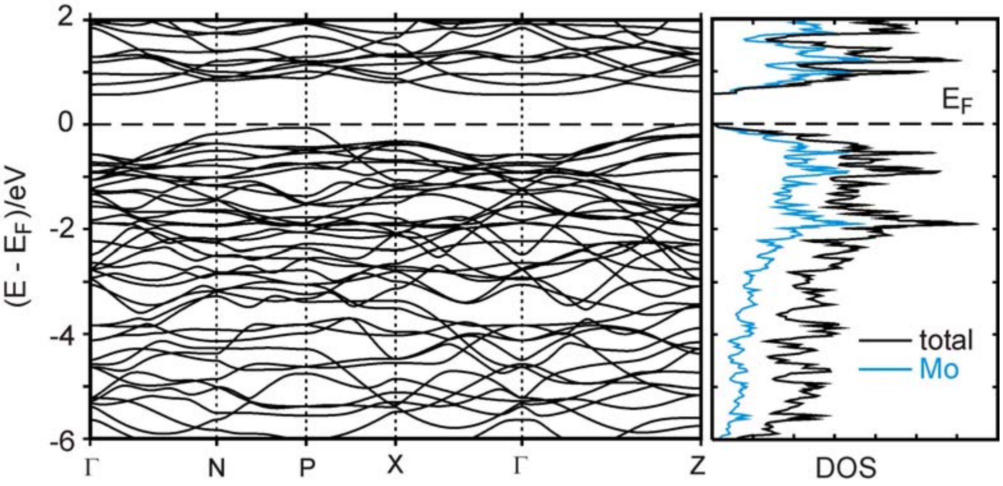

Figure 4.9 Band structure and density of states for $Mo_3Sb_5Te_2$.

There are two major differences between the band structure of $Mo_3Sb_5Te_2$ and Mo_3Sb_7. First the Fermi level falls right into the band gap in the former, but not in the later, and second, the size of the band gap decreases from 0.9 eV in Mo_3Sb_7 to 0.4 eV in $Mo_3Sb_5Te_2$. Both changes are desirable for improvement of thermoelectric properties. The filled antibonding states of the Mo–Mo interactions below the Fermi level in COHP curves (Figure 4.10) are the evidence of weaker interaction between Mo–Mo in $Mo_3Sb_5Te_2$.

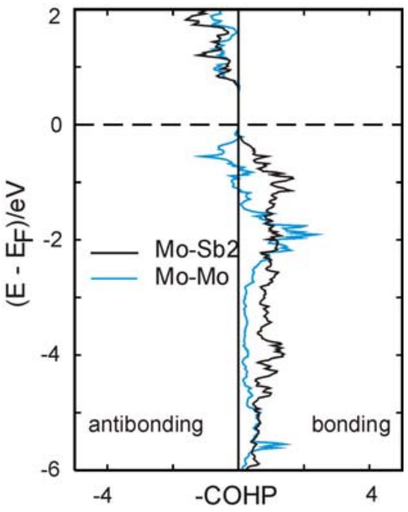

Figure 4.10 COHP curves for interactions for Mo–Sb2 and Mo–Mo.

To study the effect of cation intercalation, we calculated the electronic structure of $A_{\delta}Mo_3Sb_7$ with δ= 0.125, 0.25 and 0.5. The structure parameters of Mo_3Sb_7 were used for the calculation, and the (0, 0, 0) position was filled completely with cation *A* (*A*=Mg, Ni, Cu). Since there is only one void per primitive unit cell, the general formula will be $A_{0.5}Mo_3Sb_7$. Filling all voids with cations will not cause any changes to the space group but investigation of half or less filled voids needs enlargement of the cell and symmetry reduction ($A_{0.25}Mo_3Sb_7$ for half filled and $A_{0.125}Mo_3Sb_7$ for ¼ filled void). It is not possible to simulate $Mg_{0.0625}Mo_3Sb_7$ since the unit cell would be too large, i.e. there would be too many valence orbitals for calculations (one filled out of 16 available sites with 96 Mo atoms and 224 Sb atoms). Calculated density of states for different cations are shown in Figure 4.11.[16]

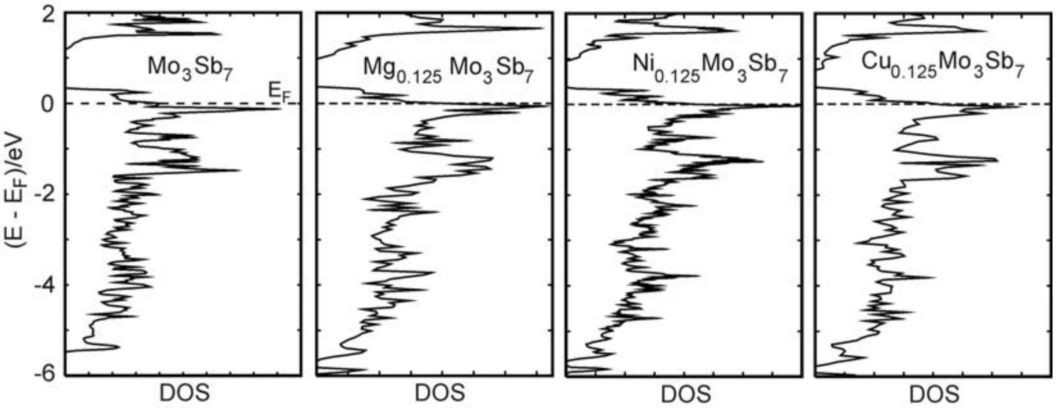

Figure 4.11 Density of states for $A_{0.125}Mo_3Sb_7$, A= Mg, Ni, Cu.

The density of states for all cases shows a band gap slightly above the Fermi level and more important a decrease in the size of the gap. The band gap in cation-intercalated compounds is around 0.5 eV for Mg and Ni and around 0.4 eV for Cu, compared to 0.9 eV for Mo_3Sb_7. To find the reason for the gap size reduction, the band structures of Mo_3Sb_7 and $Mg_{0.5}Mo_3Sb_7$ are compared in Figure 4.12.

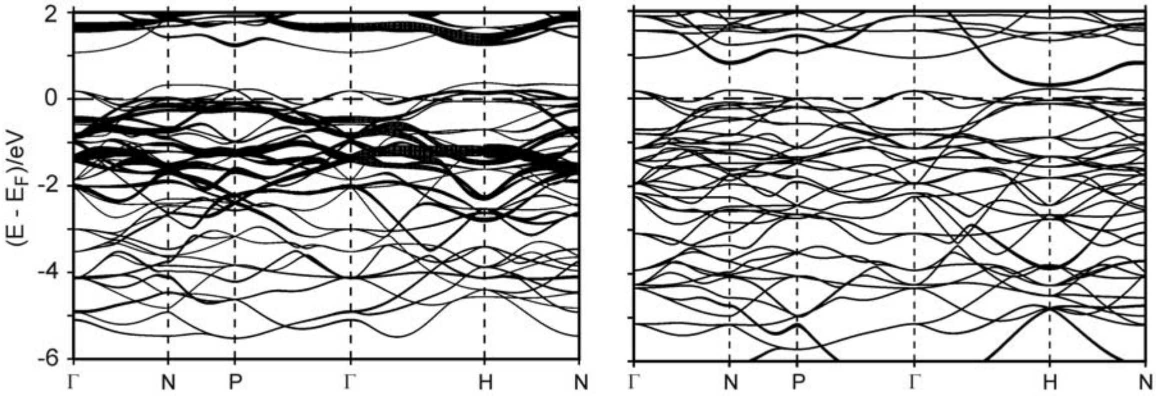

Figure 4.12 Band structure of Mo_3Sb_7 with *fat band* representation of d_Z^2 orbital contribution (left) and of $Mg_{0.5}Mo_3Sb_7$ with *fat band* representation of Mg *s* orbital (right).

For better understanding of the electronic structure the *fat band* representation[25] was used to show the contributions of Mo d_z^2 to the Mo_3Sb_7 band structure (left part of Figure 4.12) and the Mg *s* contributions to the $Mg_{0.5}Mo_3Sb_7$ band structure (right part of the Figure

4.12). The *fat band* representation is a graphical demonstration of band related to a particular orbital. Each band is given a width proportional to the corresponding orbital. The energies of the highest filled bands are the same, and the gap size reduction is the result of lowering the lowest unoccupied bands at both N and H points of the first Brillouin zone (Figure 4.13).[26] The notations for the cubic body-centered Bravais lattice were taken from Bradley and Cracknell.[27]

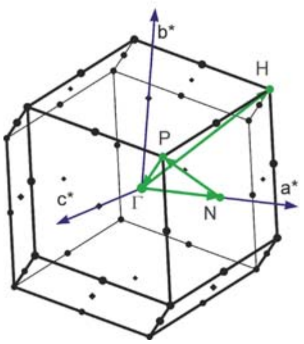

Figure 4.13 The first Brillouin zone for cubic body-centered lattices.

The smallest direct gap is the result of stabilization of Mo d_{z^2} by interacting with Mg *s* orbitals at point H in the first Brillouin zone. Higher Mg content results in smaller band gap size (Figure 4.14). This is a beneficial effect since small band gaps are favorable for thermoelectric properties.

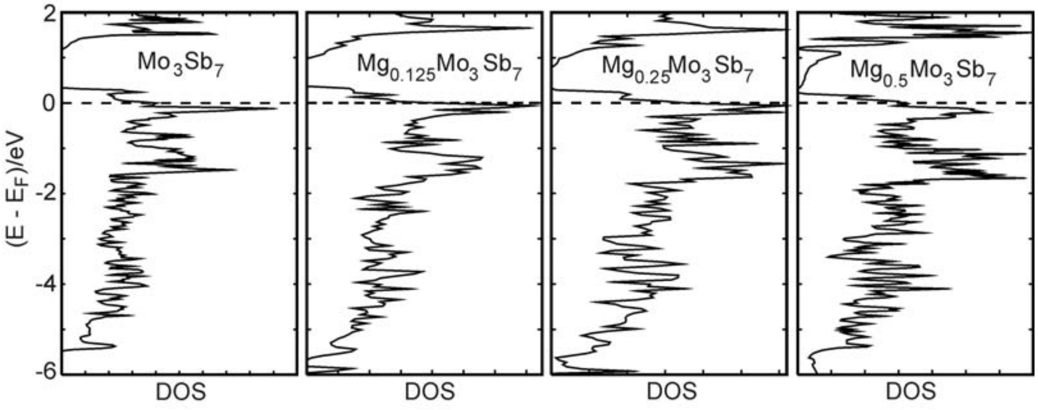

Figure 4.14 Density of states for Mo_3Sb_7 (left) and hypothetical "$Mg_\delta Mo_3Sb_7$" (right).

To investigate the effect of cation intercalation on different atomic interactions, COHP curves for $Mg_{0.5}Mo_3Sb_7$ were studied (Figure 4.15).

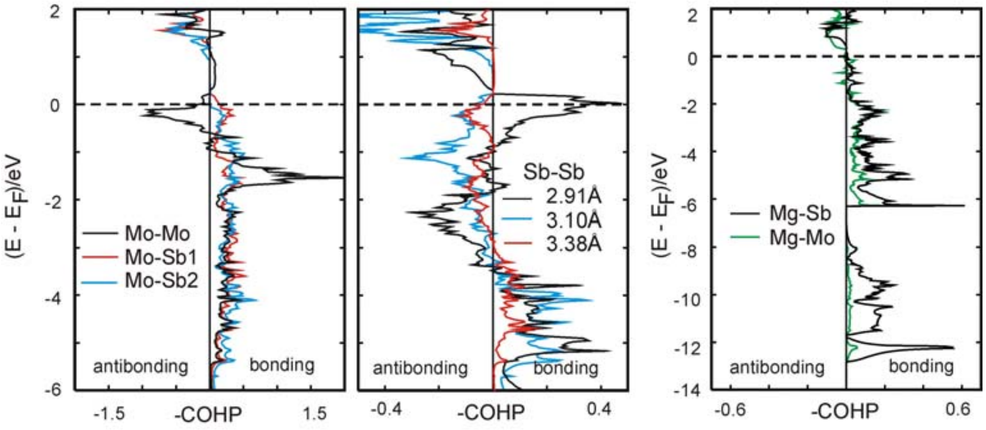

Figure 4.15 COHP curves for different interaction in $Mg_{0.5}Mo_3Sb_7$.

COHP curves for all homo nuclear interactions (Mo–Mo and three different Sb–Sb interactions) show that significant amounts of antibonding states are filled, but in overall all of the interactions have bonding character. These curves also indicate that almost all bonding states for hetronuclear interactions (Mg–Mo, Mg–Sb, Mo–Sb1, Mo–Sb2) are filled. To investigate the effect of cation intercalation on the atomic interactions, a proper procedure would be the comparison between ICOHP values in different situations. A comparison in ICOHP values for different interactions between Mo_3Sb_7 and $Mg_{0.5}Mo_3Sb_7$ are shown in Table 4.11.

Bond	no	distance (Å) Mo_3Sb_7	distance (Å) $Mg_{0.07}Mo_3Sb_7$	ICOHP (eV) Mo_3Sb_7	ICOHP (eV) $Mg_{0.5}Mo_3Sb_7$
Mo–Mo	1	2.998(4)	3.001(3)	-1.235	-1.213
Mo–Sb1	4	2.821(1)	2.8250(7)	-1.706	-1.672
Mo–Sb2	4	2.793(2)	2.7986(9)	-1.948	-1.889
Sb1–Sb1	2	3.380(1)	3.385(1)	-0.084	-0.081
Sb2–Sb2	1	2.907(3)	2.906(2)	-0.778	-0.813
Sb2–Sb2	3	3.101(2)	3.109(1)	-0.450	-0.335
Mg–Mo	2	–	3.286(1)	–	-0.352
Mg–Sb2	8	–	2.6925(9)	–	-1.187

Table 4.11 Inter atomic distances and ICOHP values for Mo_3Sb_7 and $Mg_{0.5}Mo_3Sb_7$.

The interaction between Mo–Mo in $Mg_{0.5}Mo_3Sb_7$ is slightly weaker (-1.213 eV) and the bond distance is also longer (3.001 Å) compared to Mo_3Sb_7 (-1.235 eV and 2.998 Å). This indicates that empty *s* orbital of cation can interact with Mo d_{z^2} orbital and result in weaker interactions between the two Mo atoms. The ICOHP value for Mg–Sb2 of -1.19 eV is indicative of a strong bonding interaction. Addition of cation also affects the Mo–Sb interactions. All of the Mo–Sb interactions in $Mg_{0.5}Mo_3Sb_7$ are weaker and slightly longer compared to Mo_3Sb_7. The ICOHP value for the short Sb2–Sb2 (2.906 Å) of -0.813 eV in $Mg_{0.5}Mo_3Sb_7$ indicates stronger interaction.

4.3.2 Electronic structure of $Nb_3Sb_2Te_5$

Electronic structure calculations for $Nb_3Sb_2Te_5$ reveal a band gap just above the valence band, confirming that this compound is a semiconductor with 55 valence electrons. Band structure calculations show the gap exist between the lowest point of the conduction band at P point (¼, ¼, ¼) and the highest point of the valence band at H point (½, -½, ½) of the first Brillouin zone.[27] Since the maximum and the minimum are not at the same point, the gap can be considered as an indirect band gap. Compared to $Mo_3Sb_5Te_2$ this compound has a larger band gap (0.9 eV compared to 0.45 eV). Figure 4.16 shows band structure and the density of states for $Nb_3Sb_2Te_5$.[28]

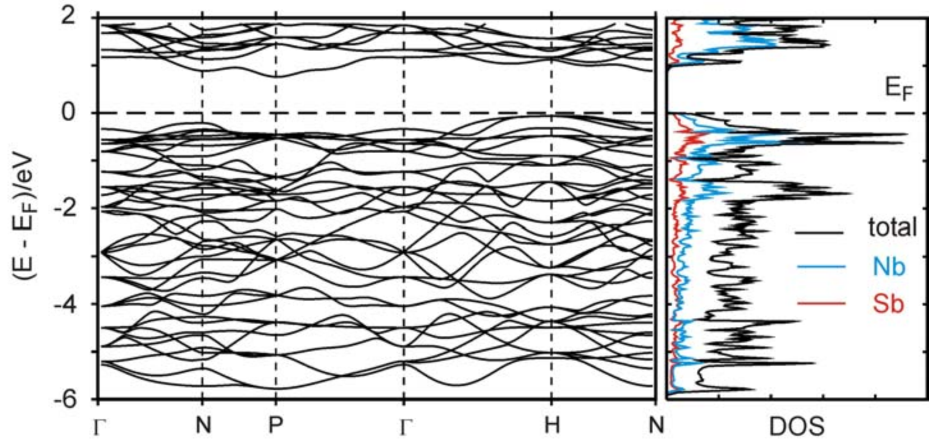

Figure 4.16 Band structure (left) and density of states (right) for $Nb_3Sb_2Te_5$.

COHP curves were used to examine different interactions. Different COHP curves are shown in Figure 4.17. Only for Nb–Nb interactions all bonding states are filled. COHP curves for the long interatomic distance between Te1–Te1 (3.471 Å) shows almost equal filling of bonding and antibonding states. Table 4.12 lists different interactions with their distances and integrated COHP values (ICOHP) for these interactions.

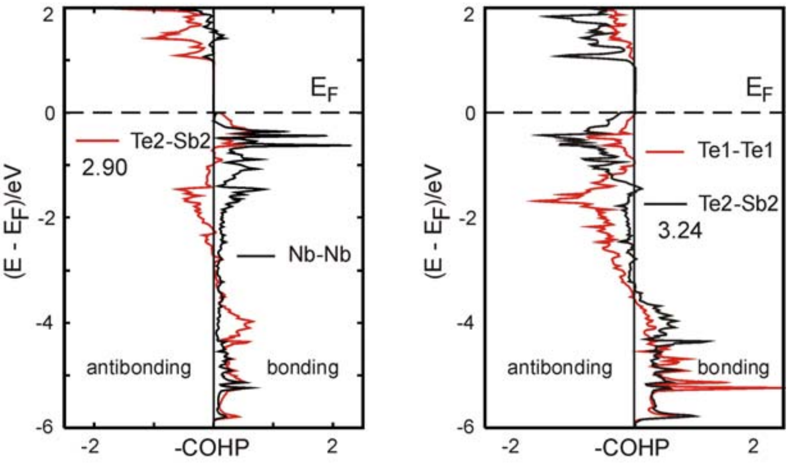

Figure 4.17 COHP curves for Nb–Nb and short Te2–Sb2 interactions (left) and Te1–Te1 and long Te2–Sb2 interactions (right).

Bond	no	distance (Å)	ICOHP (eV)
Nb–Nb	1	3.089(2)	-1.315
Nb–Sb2	2	2.8716(8)	-1.929
Nb–Te2	2	2.8854(7)	-1.947
Nb–Te1	4	2.9001(5)	-1.718
Te1–Te1	2	3.471(1)	+0.032
Te2–Sb2	1	2.898(1)	-1.249
Te2–Sb2	3	3.2361(7)	-0.198

Table 4.12 ICOHP values for different interaction in $Nb_3Sb_2Te_5$.

ICOHP value for long interaction of Te1–Te1 (3.47 Å) is very small and positive, an indication of weakly antibonding character. Also short interaction of Te2–Sb2 (2.89 Å) has stronger bonding character compared to the longer interaction (3.24 Å), as stronger bonding characters are expected for shorter bonds.

4.3.3 Electronic structure of Re_3GeAs_6

Re_3As_7 of the Ir_3Ge_7 type with its 56 valence electrons is metallic.[29] Electronic structure calculations suggested the metallic behavior for Re_3As_7 and showed a band gap just below the Fermi level (Figure 4.18).

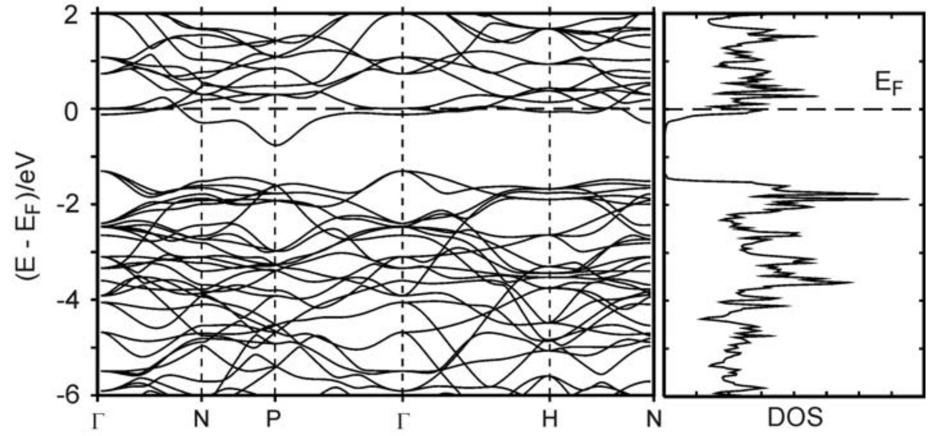

Figure 4.18 Band structure (left) and density of states (right) for Re_3As_7.

Replacing one As with one Ge will reduce the valence electrons to 55 and place the Fermi level in the band gap. To model the structure of Re_3GeAs_6, complete Ge/As ordering on the E2 site (Table 4.9) was achieved by reducing the symmetry to space group $R\overline{3}m$ (Figure 4.19).

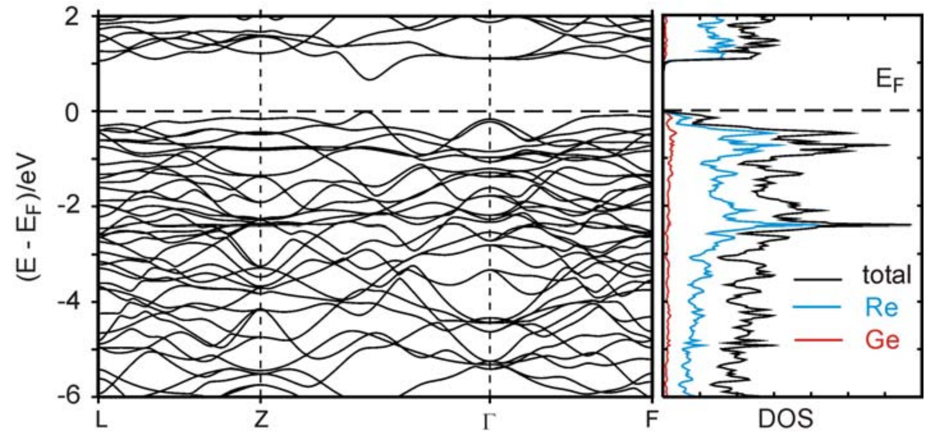

Figure 4.19 Band structure (left) and density of states (right) for Re_3GeAs_6.

Re_3GeAs_6 is a semiconducting material with a band gap around 0.9 eV. The lowest point of the conduction band and the highest point of the valence band create band gap between the points Z (½, ½, ½) and Γ (0, 0, 0) of the first Brillouin zone. Comparison between density of states for $Mo_3Sb_5Te_2$ and Re_3GeAs_6 shows that Re_3GeAs_6 has a larger band gap, and both have sharp peaks directly above and below Fermi level (Figure 4.20). Since the desired band gap is proportional to the optimal operating temperature,[30] it can be concluded that maximum ZT for Re_3GeAs_6 compound can be reached at higher temperature e. g. 1040 K. Sharp spikes in DOS of Re_3GeAs_6 lead to a large Seebeck coefficient based on Mott equation for Seebeck coefficient.[31]

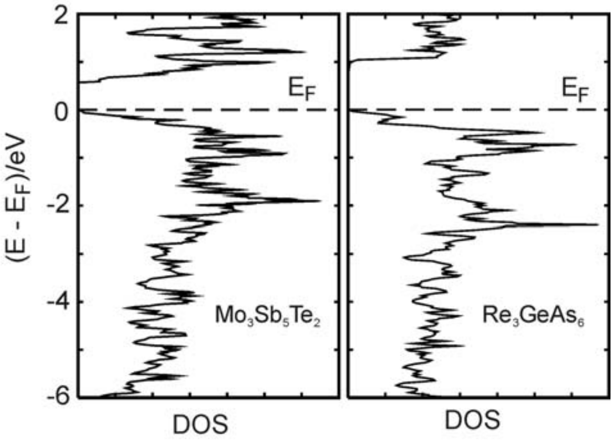

Figure 4.20 Density of states for $Mo_3Sb_5Te_2$ (left) and Re_3GeAs_6 (right).

Selected COHP curves are presented in Figure 4.21. The Re–Re interactions are mostly bonding. It is evident that Re–As1 interactions have strong bonding character while long interactions between As1–As1 mostly have antibonding character. Integrated COHP values (ICOHP) for different interactions are listed in Table 4.13.

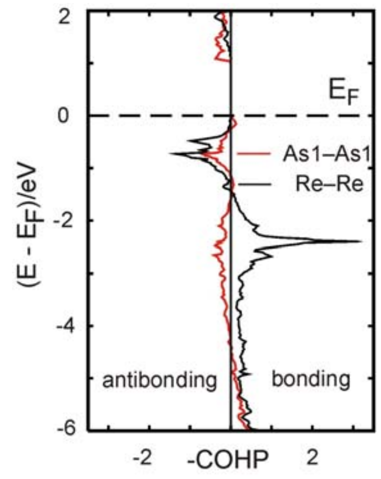

Figure 4.21 COHP curves for selected interactions in Re_3GeAs_6.

Bond	no	distance (Å)	ICOHP (eV)
Re–Re	1	2.772(4)	-1.678
Re–As1	4	2.586(1)	-2.202
As1–As1	2	3.08716(3)	-0.064

Table 4.13 ICOHP values for selected interactions.

4.4 Physical properties

The efficiency and performance of a thermoelectric material is a measure of its physical properties. Different studies, such as crystal structure determination and electronic structure calculation, were carried out to investigate details on the structure and behavior of the materials for further improvements. Proper choice of structures, elements and dopants are some of the outcomes of these investigations. In general, it is known that semiconducting materials with small band gap ($E_g = 6\text{-}10k_bT$), large Seebeck coefficient ($S = 100\text{-}200\ \mu VK^{-1}$), large electrical conductivity ($\sigma > 500\ \Omega^{-1}cm^{-1}$, carrier concentration, $n > 10^{19}$) and low thermal conductivity ($\kappa \leq 2\ Wm^{-1}K^{-1}$), will show promising thermoelectric properties and have potential for commercial applications.

4.4.1 Physical properties of Mo_3Sb_7 and $Mo_3Sb_5Te_2$

Mo_3Sb_7 is metallic, confirmed by both electrical conductivity and Seebeck coefficient measurements. In comparison to most metals ($-20 < S < +20$ μVK^{-1}), this compound has a higher Seebeck coefficient ($+26$ μVK^{-1} at 300 K).

4.4.1.1 Electrical conductivity

All measurements at University of Waterloo were carried out on cold-pressed pellets with dimensions of 6×1×1 mm. Replacing Sb atoms with Te atoms results in a semiconducting compound, $Mo_3Sb_{7-\delta}Te_\delta$, δ=0-1.6. Figure 4.22 shows the electrical conductivity for some of the cold-pressed pellets.

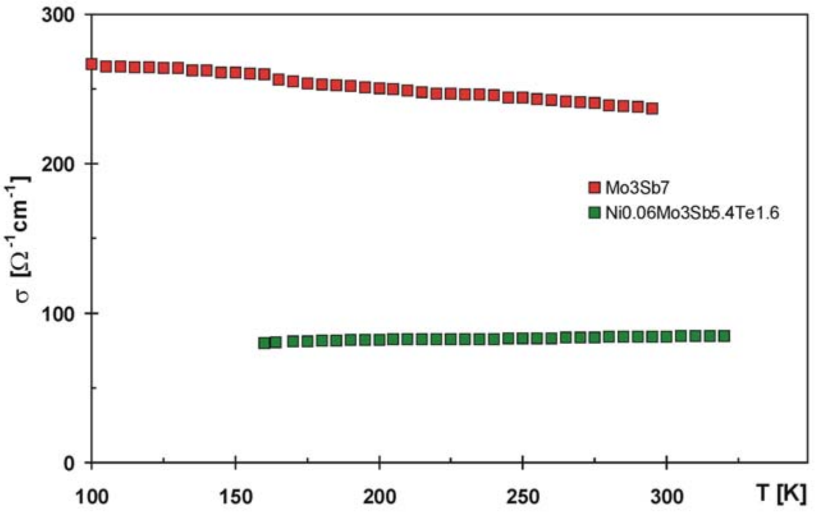

Figure 4.22 Electrical conductivities of cold pressed samples.

An increase of the conductivity with decreasing temperature was found for Mo_3Sb_7, which is an indication of metallic behavior. The observed trend for electrical conductivity (conductivity increase with temperature increase) in the remaining two compounds, reveal the nonmetallic nature of the two compounds. Addition of cation (Ni^{2+}) not only helps to decrease the band gap size, but also increases the number of charge carriers. The density of a cold pressed pellet of $Ni_{0.06}Mo_3Sb_{5.4}Te_{1.6}$ (7.334 gcm^{-3}) is about 85% of the density of single crystal (8.648 gcm^{-3}). In a study recently presented by Snyder et al.[32] electrical conductivity measurements on hot-pressed sample of $Mo_3Sb_{5.4}Te_{1.6}$ (97% of the theoretical density) exhibit much larger values for electrical conductivity (1500 Ω^{-1}cm^{-1} at 300 K) in comparison to our electrical conductivity measurements on cold-pressed $Mo_3Sb_{5.4}Te_{1.6}$ (85 Ω^{-1}cm^{-1}). To investigate the effect of hot pressing on thermoelectric effects of the samples, large samples (~ 2 g) of $Mo_3Sb_{5.4}Te_{1.6}$ and $Ni_{0.06}Mo_3Sb_{5.4}Te_{1.6}$ were prepared and examined for phase purity via powder X-ray diffraction. The pure phase samples were sent to Clemson University, South Carolina for physical property measurements. The sample was pressed under 240 Mpa pressure with die diameter of 0.5 inches for 1 hour at 720 ºC. As a result, the densities of hot-pressed samples were 8.54 gcm^{-3} (97% of the crystal density) for $Mo_3Sb_{5.4}Te_{1.6}$ and 8.71 gcm^{-3} (99% of the crystal density) for the $Ni_{0.06}Mo_3Sb_{5.4}Te_{1.6}$. Figure 4.23 shows electrical conductivities for the two hot-pressed samples.

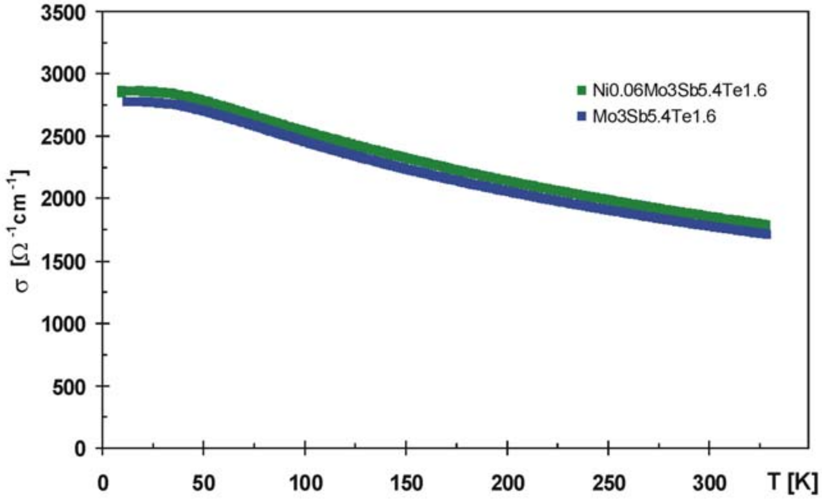

Figure 4.23 Electrical conductivities of hot-pressed $Mo_3Sb_{5.4}Te_{1.6}$ and $Ni_{0.06}Mo_3Sb_{5.4}Te_{1.6}$.

Electrical conductivity of $Ni_{0.06}Mo_3Sb_{5.4}Te_{1.6}$ is slightly larger than $Mo_3Sb_{5.4}Te_{1.6}$, 1852 Ω^{-1}cm^{-1} and 1786 S Ω^{-1}cm^{-1} at 300 K respectively. The Hall coefficient was measured at Clemson University. As it was expected, addition of cation (Ni^{2+}) increases the carrier concentration, namely from 3.8×10^{21} cm^{-3} in $Mo_3Sb_{5.4}Te_{1.6}$ to 4.8×10^{21} cm^{-3} in $Ni_{0.06}Mo_3Sb_{5.4}Te_{1.6}$ at 280 K (Figure 4.24).

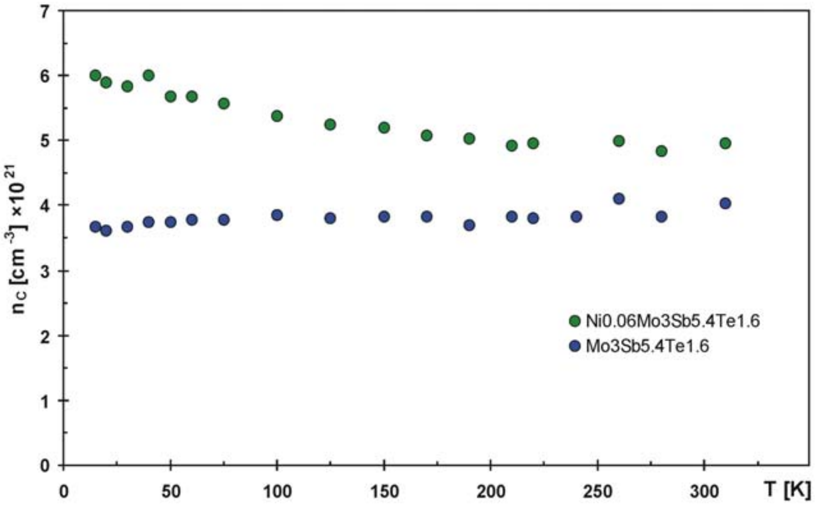

Figure 4.24 Carrier concentration for $Mo_3Sb_{5.4}Te_{1.6}$ and $Ni_{0.06}Mo_3Sb_{5.4}Te_{1.6}$.

At higher temperature scattering from the acoustic phonon modes increases so the mobility of both compounds decreases (Figure 4.25).

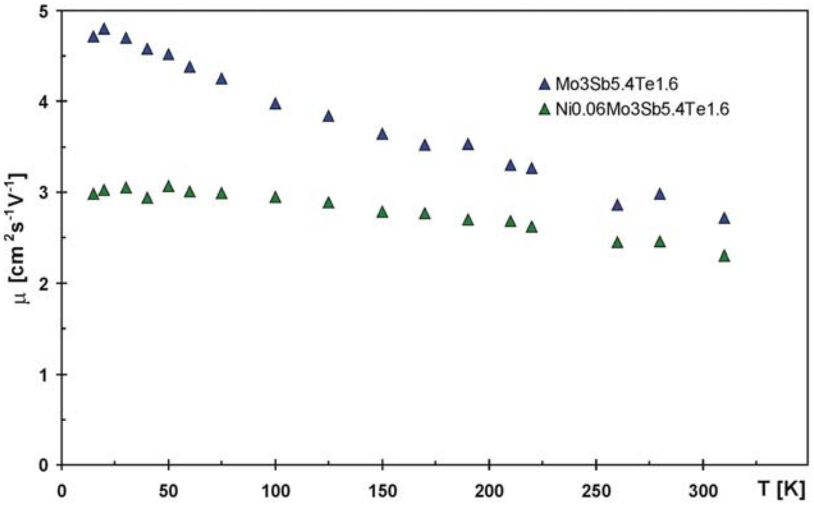

Figure 4.25 Carrier mobility for $Mo_3Sb_{5.4}Te_{1.6}$ and $Ni_{0.06}Mo_3Sb_{5.4}Te_{1.6}$.

4.4.1.2 Seebeck coefficient

Comparison between the Seebeck coefficient of Mo_3Sb_7 and $Ni_{0.06}Mo_3Sb_{5.4}Te_{1.6}$ is presented in Figure 4.26

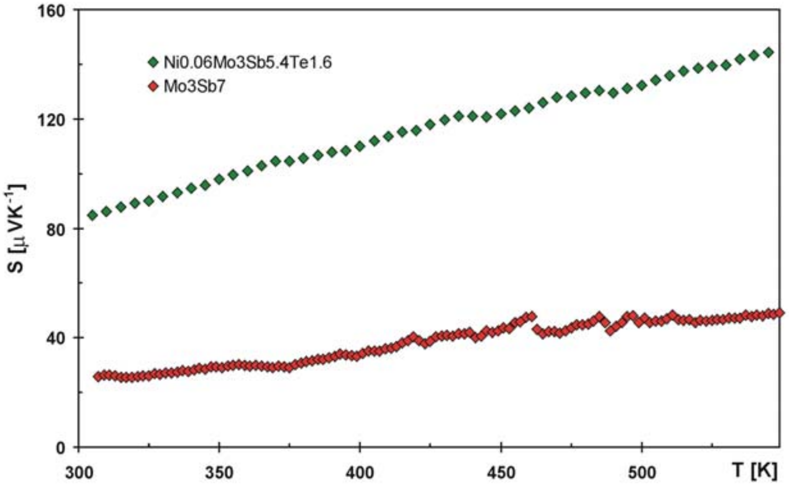

Figure 4.26 Seebeck coefficient of cold-pressed samples of Mo_3Sb_7, $Ni_{0.06}Mo_3Sb_{5.4}Te_{1.6}$ and $Mo_3Sb_5Te_2$.

Hot-pressed samples showed drastic increase in electrical conductivities and it would be beneficial to investigate the effect of hot pressing on the Seebeck coefficient (Figure 4.27).

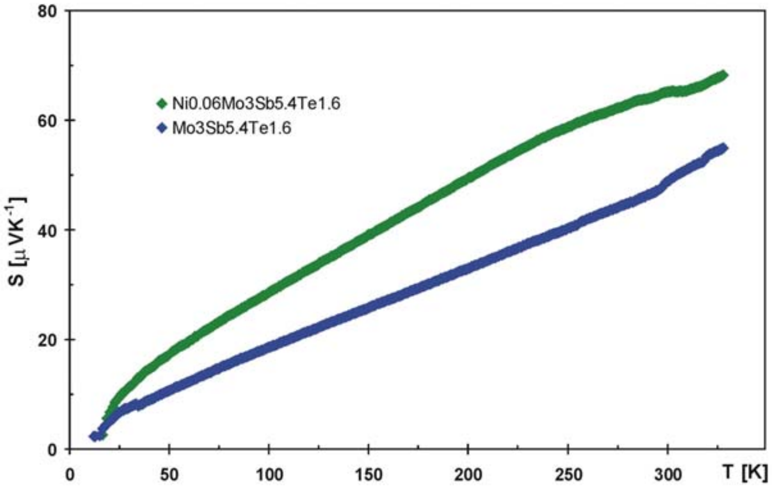

Figure 4.27 Seebeck coefficients of hot-pressed $Ni_{0.06}Mo_3Sb_{5.4}Te_{1.6}$ and $Mo_3Sb_5Te_2$.

The Seebeck coefficients for $Ni_{0.06}Mo_3Sb_{5.4}Te_{1.6}$ and $Mo_3Sb_{5.4}Te_{1.6}$ are +65 μVK^{-1} and +49 μVK^{-1}, respectively, at 300 K. It is important to notice that both, electrical conductivity and Seebeck coefficient are increased by addition of nickel. The addition of nickel results in a change of the Fermi surface. The electrical conductivity is proportional to the DOS energy at Fermi level, while the Seebeck coefficient is proportional to its slope. Hence both the number of states as well as the slope of DOS is increased.

4.4.1.3 Thermal conductivity

Figure 4.28 shows the thermal conductivity measurements on hot-pressed pellets of $Ni_{0.06}Mo_3Sb_{5.4}Te_{1.6}$ and $Mo_3Sb_5Te_2$.

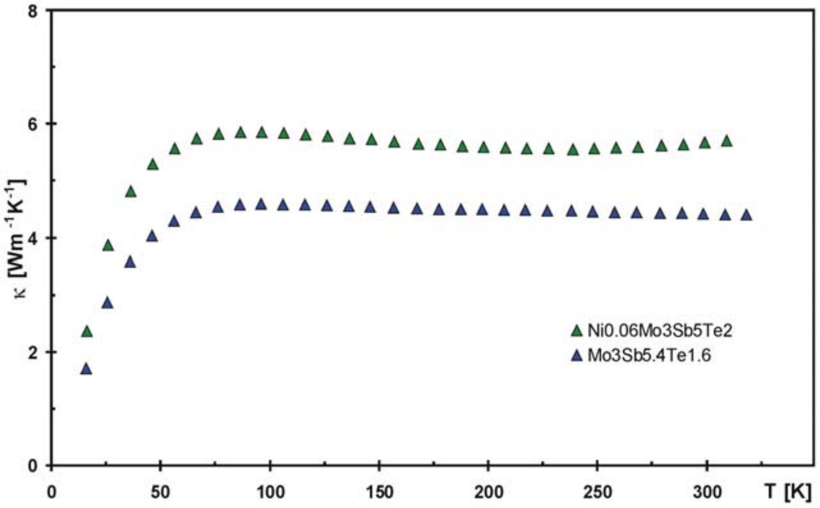

Figure 4.28 Thermal conductivity measurements for $Ni_{0.06}Mo_3Sb_{5.4}Te_{1.6}$ and $Mo_3Sb_5Te_2$.

Both compounds show constant thermal conductivity for the range of 75-300 K. By applying Wiedemann-Franz relationship it is possible to calculate the lattice thermal conductivities ($\kappa_e = L\sigma T$), where L is the Lorentz number ($W\Omega K^{-2}$), σ is electrical conductivity ($\Omega^{-1}m^{-1}$) and T is the temperature (K). Figure 4.29 shows the comparison between the lattice thermal conductivities of $Ni_{0.06}Mo_3Sb_{5.4}Te_{1.6}$ and $Mo_3Sb_5Te_2$.

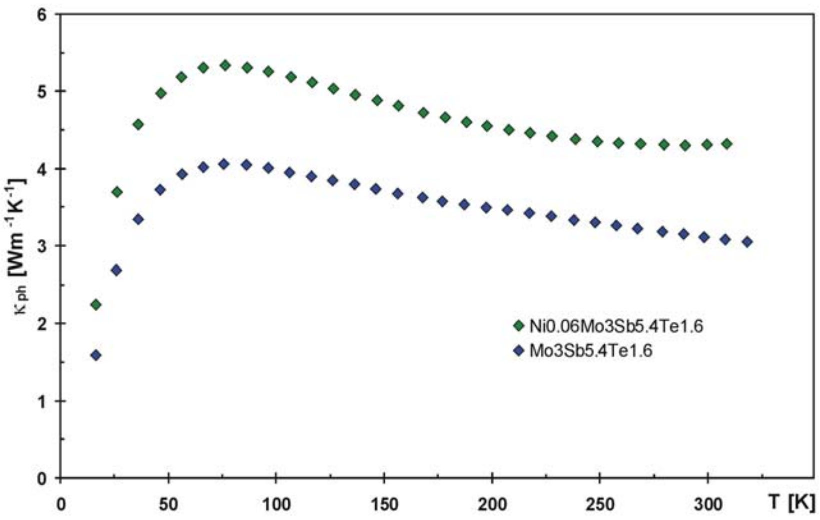

Figure 4.29 Lattice thermal conductivities (κ_{ph}) for $Ni_{0.06}Mo_3Sb_{5.4}Te_{1.6}$ and $Mo_3Sb_5Te_2$.

The lattice thermal conductivity for $Ni_{0.06}Mo_3Sb_{5.4}Te_{1.6}$ is 4.3 $Wm^{-1}K^{-1}$ and the lattice thermal conductivity for $Mo_3Sb_5Te_2$ is 3.1 $Wm^{-1}K^{-1}$ at 300 K. This is opposite to what we were expecting. The effect of introducing a rattler into a cage of the crystal is a known phenomenon,[33] and filled skutterudites are examples of the fact that rattlers can reduce the thermal conductivity. Unfortunately in our samples introducing Ni as "rattler" increased the thermal conductivity rather than decreasing it. An important condition for a filler atom to act as a rattler in a cage is that the atom should be small and heavy and have loose bonds to the cage so it can give rise to localized frequency phonon modes (Einstein modes).[34] The distances of Sb2 atoms to the middle of the cube are 2.68 Å. Considering the Pauling metallic radii for Ni (1.15 Å) and Sb (1.39 Å), there would be enough room for Ni to rattle, but when Slater atomic radii are considered (1.45 Å for Sb and 1.35 Å for Ni), the cube might be too small to accommodate the cation. As for Ni–Sb distances, in $NiSb_2$[35] the Ni atom is six fold coordinated with four bonds of 2.566 Å and two of 2.544 Å. In NiSb,[36] six Ni–Sb bonds are about 2.608 Å with two Ni–Ni bonds of 2.568 Å. It is thus concluded that the eight fold coordinated Ni atom would ideally have bond distance of 2.6 Å. For example in TiSb,[37] the

Ti–Sb distance is 2.830 Å (six fold coordinated), and in $TiSb_2$[37] the distance is 2.602 Å (eight fold coordinated). From the results of thermal conductivity measurements, it is unlikely that the Ni atom acts as a rattler in $Ni_{0.06}Mo_3Sb_{5.4}Te_{1.6}$. Instead it is acting like space filler, as it does not reduce the thermal conductivity. More investigations will be carried out on these systems, and the role of the cation in thermal conductivity of these materials will be investigated.

4.4.2 Physical properties of $Nb_3Sb_2Te_5$

$Nb_3Sb_2Te_5$ crystallizes in Ir_3Ge_7 structure type. As part of the investigation on thermoelectric materials with Ir_3Ge_7 structure type, physical property of this compound was investigated. Physical properties of the cold-pressed samples were measured at University of Waterloo and hot-pressed samples were measured at Clemson University.

4.4.2.1 Electrical conductivity

Since the band gap of $Nb_3Sb_2Te_5$ was larger than the gap of $Mo_3Sb_5Te_2$, it is expected for this compound to have lower κ_{el} as well. Electrical conductivity measurement on cold-pressed sample is shown in Figure 4.30. It should also be mentioned here that synthesis of $Nb_3Sb_{2-\delta}Te_{5+\delta}$ with $-0.1 > \delta$ and $\delta > 0.1$ was not successful and for different values of δ either $NbSb_2$ or $NbTe_2$ were present as side products. All measurements were carried out on phase pure samples ($Nb_3Sb_2Te_5$).

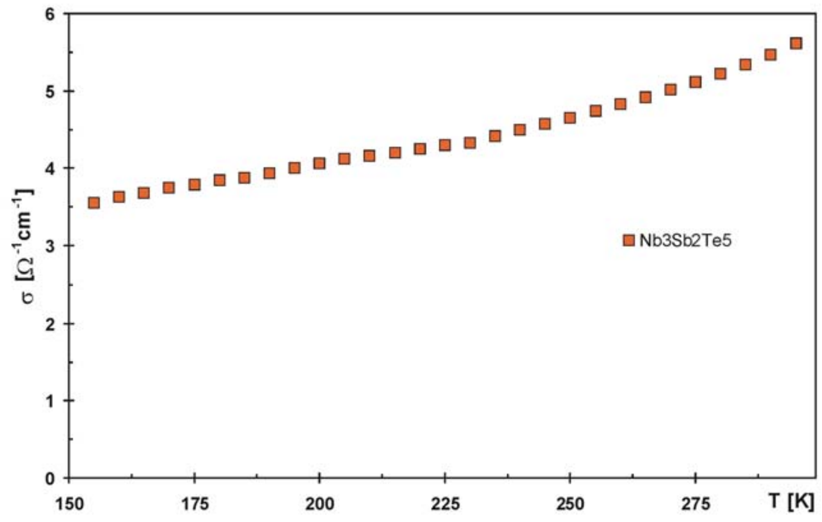

Figure 4.30 Electrical conductivity of cold-pressed sample of $Nb_3Sb_2Te_5$.

Semiconducting behavior of this compound can be observed from conductivity curve since conductivity increases with temperature. A large sample of phase pure $Nb_3Sb_2Te_5$ was prepared and sent to Clemson for physical property measurements. The sample was pressed under weight of 1.4 tons with die diameter of 0.375 inches for 1 hour at 650 ºC. The density of hot-pressed sample approached to 94% of the crystal density (7.646 gcm^{-3} vs. 8.146 gcm^{-3} for crystal). Figure 4.31 shows the conductivity of hot-pressed $Nb_3Sb_2Te_5$. It is obvious from the conductivity curve that this compound is a semiconductor and because the slope is not exponential this compound can be classified as an extrinsic semiconductor. In an intrinsic semiconductor, the conductivity is governed by the size of the band gap and the temperature. As for extrinsic semiconductor, the conductivity is controlled by the addition of the dopants.[38]

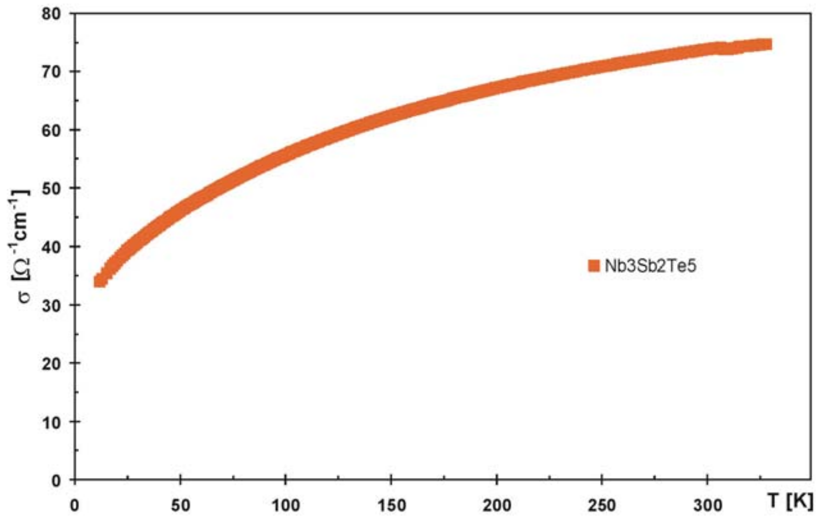

Figure 4.31 Electrical conductivity of hot-pressed sample of $Nb_3Sb_2Te_5$.

4.4.2.2 Seebeck coefficient

Seebeck coefficient measurement on cold-pressed sample of $Nb_3Sb_2Te_5$ is shown in Figure 4.32. $Nb_3Sb_2Te_5$ exhibits negative Seebeck values, thus it is an *n*-type material.

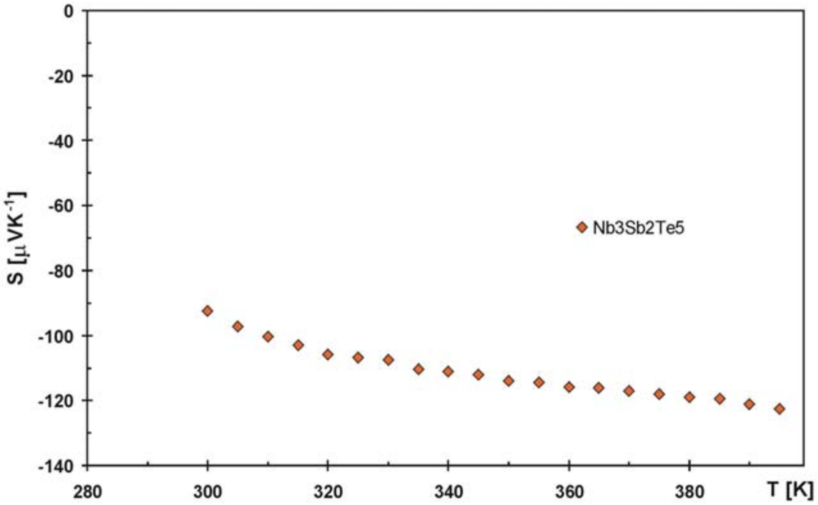

Figure 4.32 Seebeck coefficient of cold-pressed $Nb_3Sb_2Te_5$.

The Seebeck values of the hot-pressed samples were much smaller than what we measured with our equipment i.e. cold pressed, on a different sample of the same nominal composition. Seebeck coefficient measurements on other samples ($Mo_3Sb_{5.4}Te_{1.6}$ and $Ni_{0.06}Mo_3Sb_{5.4}Te_{1.6}$) showed small differences between the cold-pressed and hot-pressed samples. Because of the low electrical conductivity for this sample, we expected to have larger values of Seebeck coefficient but since the overall properties of this compound in comparison to molybdenum compounds are not desirable, no further investigations of the experiment seem to be necessary at this point. Figure 4.33 shows the Seebeck measurement of the hot-pressed $Nb_3Sb_2Te_5$.

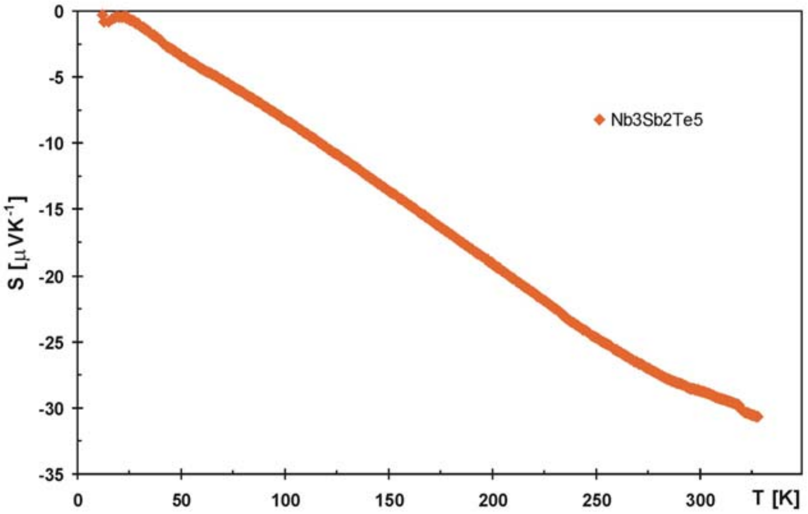

Figure 4.33 Seebeck coefficient of hot-pressed $Nb_3Sb_2Te_5$.

4.4.2.3 Thermal conductivity

The thermal conductivity of the hot-pressed sample was measured. The κ slowly decreases with increasing temperature above 60 K, and reaches 5.7 $Wm^{-1}K^{-1}$ at 300 K. These values are high for thermoelectric applications. Figure 4.34 shows thermal conductivity of $Nb_3Sb_2Te_5$.

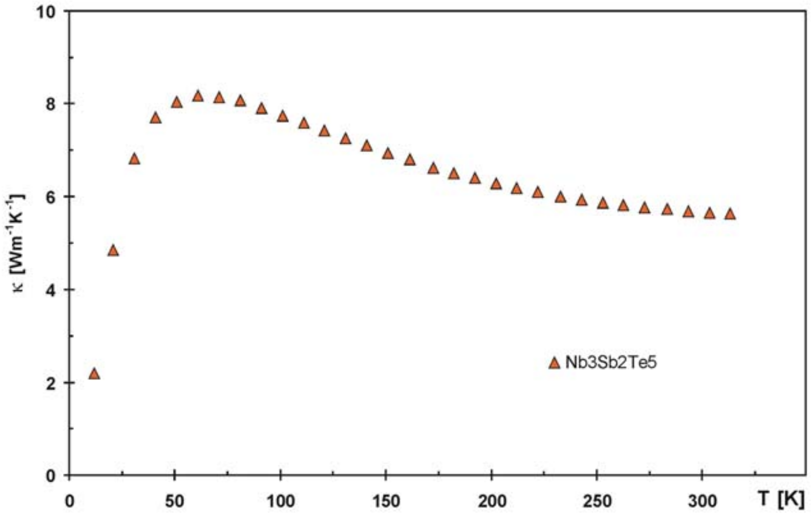

Figure 4.34 Thermal conductivity of hot-pressed $Nb_3Sb_2Te_5$.

4.4.3 Physical properties of $Re_3Ge_\delta As_{7-\delta}$

Thermoelectric modules are consisting of *p*-type and *n*-type materials electrically series and thermally parallel connected. Promising thermoelectric properties were observed in case of $Mo_3Sb_{5.4}Te_{1.6}$ and $Ni_{0.06}Mo_3Sb_{5.4}Te_{1.6}$ (both *p*-type materials). The third compound under investigation for thermoelectric applications is $Re_3Ge_\delta As_{7-\delta}$ ($0.1 \leq \delta \leq 1$) with the Ir_3Ge_7 structure and *n*-type properties. The *n*-type properties of $Re_3Ge_{0.6}As_{6.4}$ can be deduced from electron counting (55.4 valence electrons), whereas $Mo_3Sb_{5.4}Te_{1.6}$ with 54.6 valence electrons is *p*-type.

4.4.3.1 Electrical conductivity

Series of $Re_3Ge_{\delta}As_{7-\delta}$ samples with δ=0.4, 0.6, 0.8 and 1 were prepared, and phase pure samples were tested for physical property measurements. Electrical conductivities for cold-pressed samples were measured and the results are shown in Figure 4.35. The cold pressed samples had densities around 9.0 gcm^{-3}, which is about 83% of the crystal density determined via neutron diffraction.

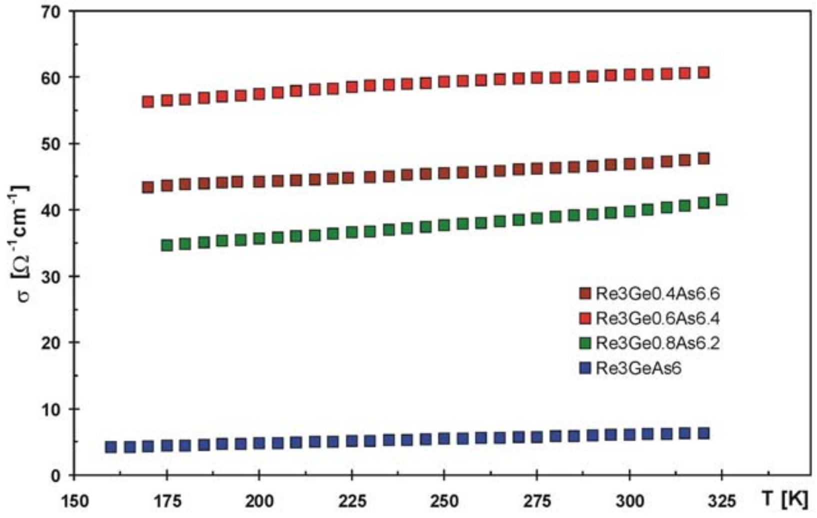

Figure 4.35 Electrical conductivity measurements for cold-pressed $Re_3Ge_{\delta}As_{7-\delta}$ (δ=0.4, 0.6, 0.8).

$Re_3Ge_{0.6}As_{6.4}$ has the best conductivity between all measured samples i.e. 60 Ω^{-1}cm^{-1} at 300 K. Large samples of Re_3GeAs_6 and $Re_3Ge_{0.6}As_{6.4}$ were prepared and their purities checked via powder X-ray diffraction. The two samples were hot-pressed under a weight of 2.3 tons with die diameter of 0.5 inch for 1.5 hours at 720 ºC. The sample densities were 89% and 93% for Re_3GeAs_6 and $Re_3Ge_{0.6}As_{6.4}$ respectively. The results of electrical conductivity measurements for the two hot-pressed samples are shown in Figure 4.36.

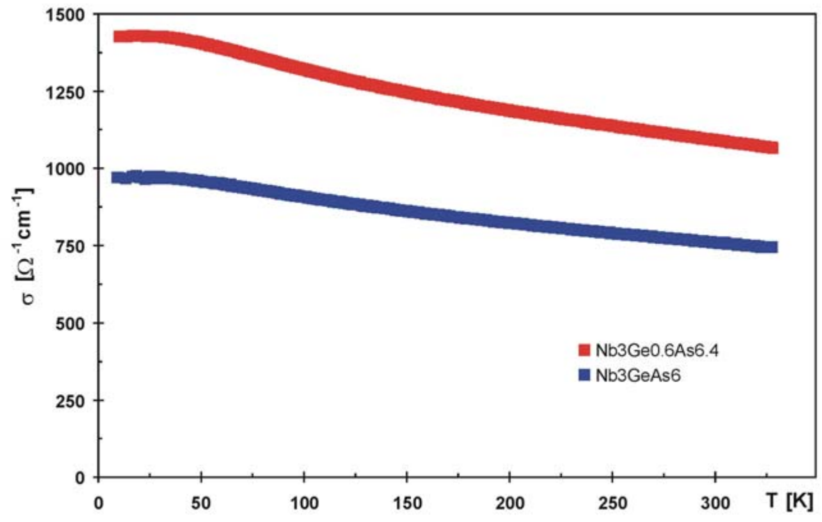

Figure 4.36 Electrical conductivity measurements for hot-pressed Re_3GeAs_6 and $Re_3Ge_{0.6}As_{6.4}$.

Since Re_3GeAs_6 has larger band gap compared to $Mo_3Sb_5Te_2$, it was expected to have smaller electrical conductivity and the experimental results confirmed the predictions (6.11 $\Omega^{-1}cm^{-1}$ and 60.35 $\Omega^{-1}cm^{-1}$ at 300 K for Re_3GeAs_6 and $Re_3Ge_{0.6}As_{6.4}$ respectively, compared to 84.62 $\Omega^{-1}cm^{-1}$ for $Mo_3Sb_{5.4}Te_{1.6}$).

4.4.3.2 Seebeck coefficient

Seebeck coefficient of different cold-pressed samples was measured at University of Waterloo (Figure 4.37). The negative sign of the Seebeck coefficient implies the *n*-type properties of these compounds. The large Seebeck coefficients (around –90 μVK^{-1} at 300 K) of these materials are quite promising. The Seebeck coefficients for hot-pressed samples were also measured, and the results are presented in Figure 4.38.

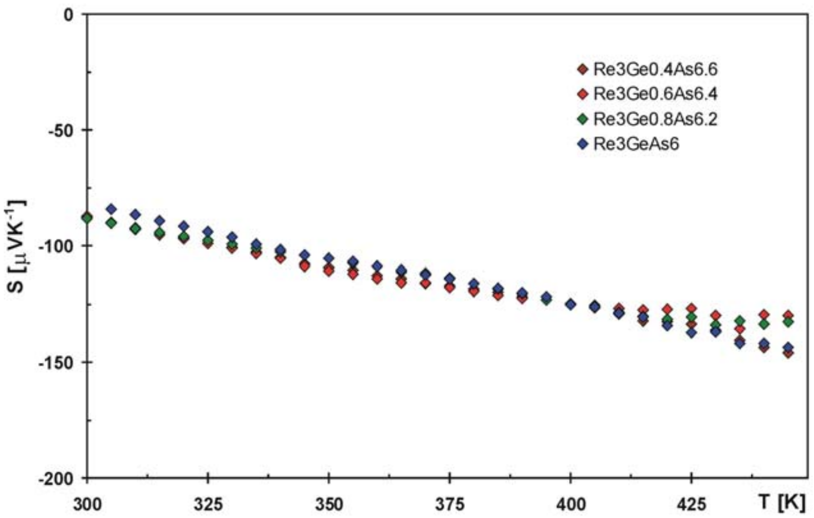

Figure 4.37 Seebeck coefficient measurements for $Re_3Ge_\delta As_{7-\delta}$ (δ=0.4, 0.6, 0.8).

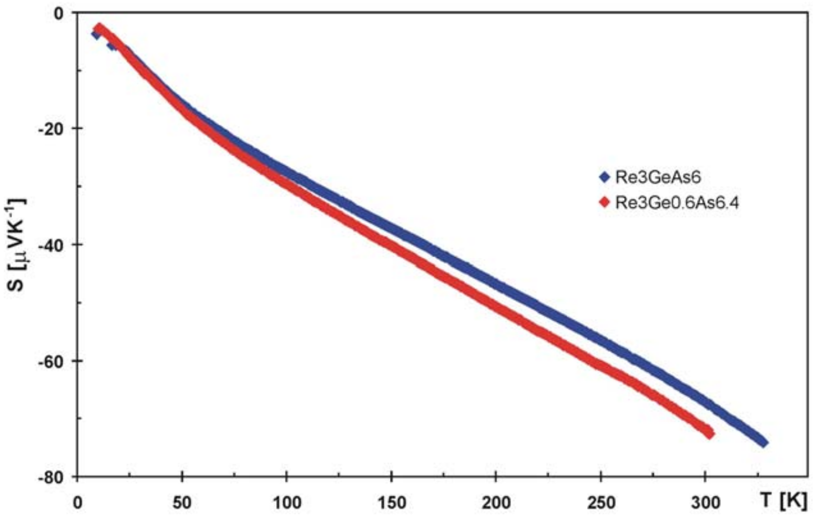

Figure 4.38 Seebeck coefficients for hot-pressed Re_3GeAs_6 and $Re_3Ge_{0.6}As_{6.4}$.

Seebeck values for hot-pressed samples increase with increasing temperature, and reach around –67 μVK^{-1} and –72 μVK^{-1} for Re_3GeAs_6 and $Re_3Ge_{0.6}As_{6.4}$ respectively. The large Seebeck values for both $Re_3Ge_{0.6}As_{6.4}$ and $Ni_{0.06}Mo_3Sb_{5.4}Te_{1.6}$ with *n*-type and *p*-type properties give rise to the idea of a possible thermoelectric device for high temperature applications comprised of the two compounds.

4.4.3.3 Thermal conductivity

Thermal conductivities were measured for the two hot-pressed samples (Re_3GeAs_6 and $Re_3Ge_{0.6}As_{6.4}$). The thermal conductivities increase rapidly from 1.1 $Wm^{-1}K^{-1}$ and 1.5 $Wm^{-1}K^{-1}$ at 20 K for Re_3GeAs_6 and $Re_3Ge_{0.6}As_{6.4}$ respectively, to around 3.1 $Wm^{-1}K^{-1}$ and 3.6 $Wm^{-1}K^{-1}$ at 100 K, and then increase to 3.8 $Wm^{-1}K^{-1}$ and 4.2 $Wm^{-1}K^{-1}$ at 300 K (Figure 4.39).

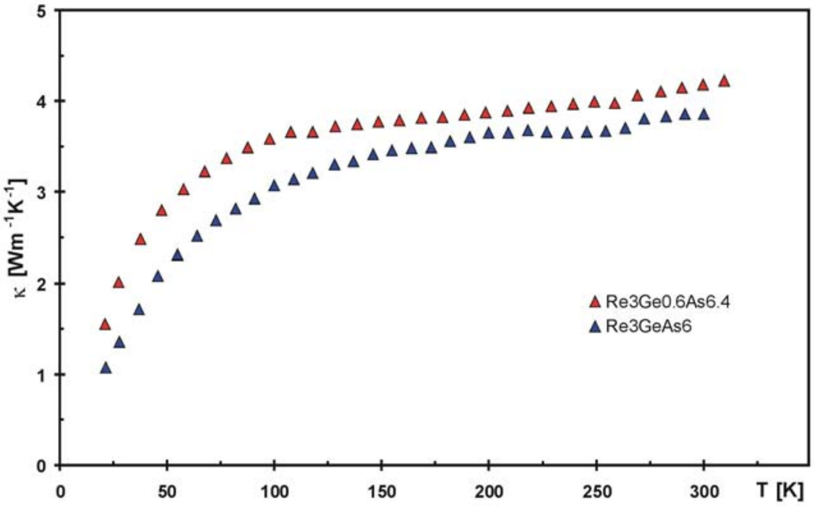

Figure 4.39 Thermal conductivities for Re_3GeAs_6 and $Re_3Ge_{0.6}As_{6.4}$.

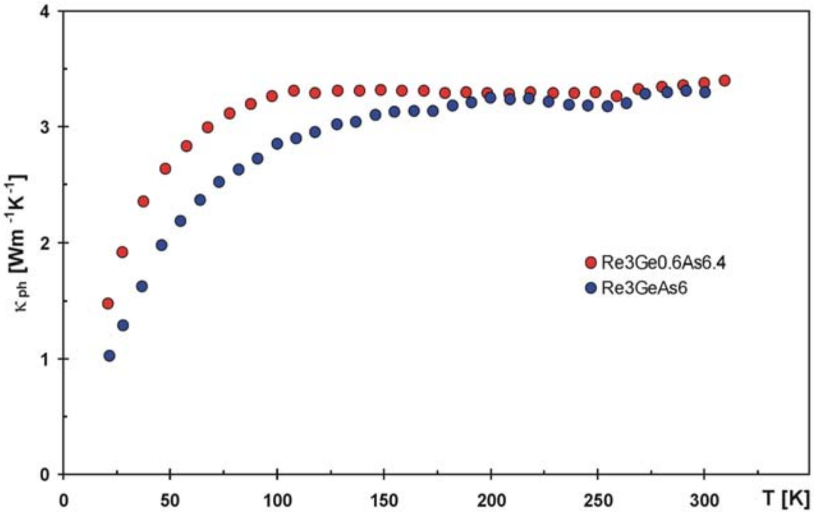

Figure 4.40 κ_{ph} curves for Re_3GeAs_6 and $Re_3Ge_{0.6}As_{6.4}$ calculated via Wiedemann-Franz law.

Figure 4.40 shows the lattice thermal conductivity of the samples calculated via Wiedemann-Franz law. Comparison between lattice thermal conductivities of Re_3GeAs_6 (3.3 $Wm^{-1}K^{-1}$), $Re_3Ge_{0.6}As_{6.4}$ (3.4 $Wm^{-1}K^{-1}$) and $Mo_3Sb_{5.4}Te_{1.6}$ (3.5 $Wm^{-1}K^{-1}$) implies that the difference between the thermal conductivities stem from difference in electronic contributions (molar masses of the three compounds are very similar) between the three compounds.

4.5 Comparison of the Ir_3Ge_7 materials with other high temperature thermoelectric materials

The thermoelectric properties of semiconducting materials with Ir_3Ge_7 structure are comparable to some of the leading thermoelectric materials. ZT diagrams for these compounds are shown in Figure 4.41, Figure 4.42 and Figure 4.43. Table 4.14 presents the thermoelectric properties for some of the best thermoelectric performers at high temperature in comparison to our measured samples.

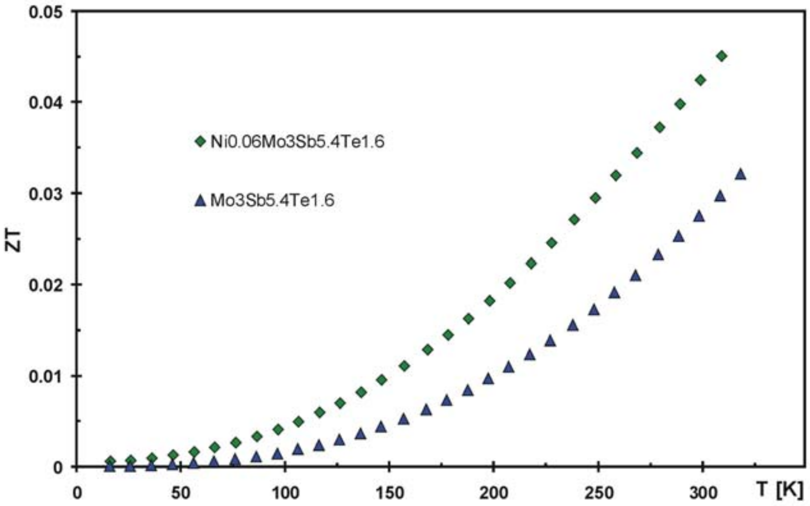

Figure 4.41 ZT vs. temperature for $Mo_3Sb_{5.4}Te_{1.6}$ and $Ni_{0.06}Mo_3Sb_{5.4}Te_{1.6}$.

The ZT value at 300 K for $Mo_3Sb_{5.4}Te_{1.6}$ (0.029) is comparable to the reported ZT for the sample with the same stoichiometry by Snyder et al.[32] The ZT diagram implies that the Ni intercalated compound ($ZT_{(300\ K)}$=0.04) has excellent thermoelectric properties, improved with respect to $Mo_3Sb_{5.4}Te_{1.6}$ competing with filled skutterudites at high temperature.

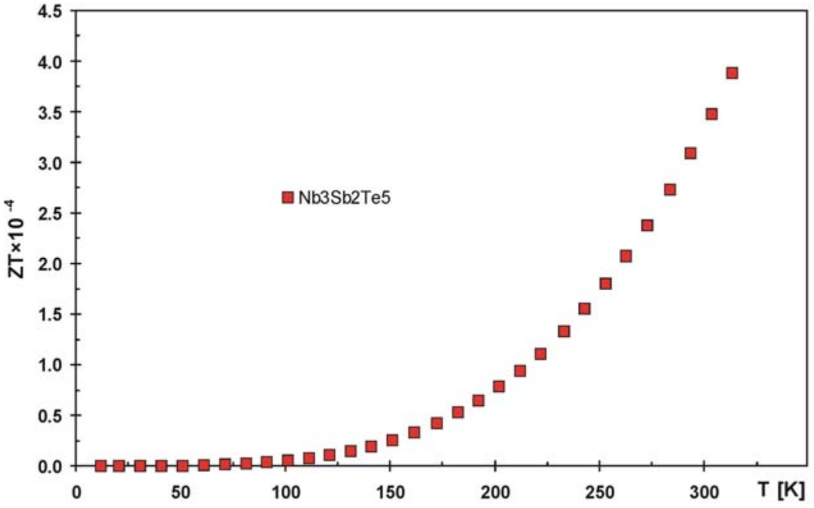

Figure 4.42 ZT vs. temperature for $Nb_3Sb_2Te_5$.

It is evident that $Nb_3Sb_5Te_2$ is not a competitive material for thermoelectric applications, since its ZT (300 K) value of 4×10^{-4} is 100 times smaller than that of $Mo_3Sb_{5.4}Te_{1.6}$.

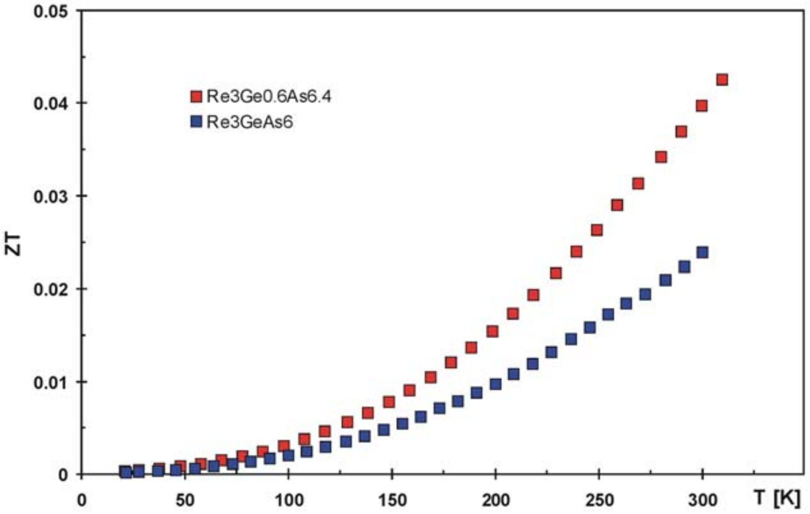

Figure 4.43 ZT vs. temperature of $Re_3Ge_{0.6}As_{6.4}$ and Re_3GeAs_6.

The ZT value of $Re_3Ge_{0.6}As_{6.4}$ at room temperature is comparable to $Ni_{0.06}Mo_3Sb_{5.4}Te_{1.6}$, 0.042 vs. 0.041, placing this compound into the same category as some of the best high temperature thermoelectric performers, if the ZT slope continues to increase steadily at high temperature.

	T [K]	S [μVK^{-1}]	σ [$\Omega^{-1}cm^{-1}$]	κ [$Wm^{-1}K^{-1}$]	ZT
$AgPb_{18}SbTe_{12}$[39]	300	-135	1850	2.3	0.44
$AgPb_{18}SbTe_{12}$	700	-335	250	1.0	1.40
$Yb_{14}MnSb_{11}$[40]	300	60	475	0.8	0.06
$Yb_{14}MnSb_{11}$	1000	160	222	0.7	0.81
$Mo_3Sb_{5.4}Te_{1.6}$[32]	310	-72	2020	4.35	0.07
$Mo_3Sb_{5.4}Te_{1.6}$	1000	-153	1055	2.76	0.9
$Ni_{0.06}Mo_3Sb_{5.4}Te_{1.6}$ (This work)	300	-65	1900	5.6	0.04
$Mo_3Sb_{5.4}Te_{1.6}$ (This work)	300	-49	1778	4.4	0.03
$Re_3Ge_{0.6}As_{6.4}$ (This work)	300	-72	1085	4.2	0.04
Re_3GeAs_6 (This work)	300	-67	759	3.85	0.03

Table 4.14 Comparison between the Ir_3Ge_7 materials and some of the leading high temperature thermoelectric materials.

4.6 References

[1] S. C. Sevov, in *Intermetallic Compounds: Principles and Practice, Vol. 3* (Eds.: J. H. Westbrook, R. L. Fleischer), John Wiley & Sons, Ltd., New York, NY, **2002**, pp. 113.

[2] U. Häussermann, M. Elding-Ponten, C. Svensson, S. Lidin, *Chem. Eur. J.* **1998**, *4*, 1007.

[3] A. Brown, *Nature* **1965**, *206*, 502.

[4] L. Pauling, *The Nature of the Chemical Bond*, 3rd ed., Cornell University Press, Ithaca, NY, **1948**.

[5] E. Dashjav, A. Szczepenowska, H. Kleinke, *J. Mater. Chem.* **2002**, *12*, 345.

[6] W. Hönle, H.-G. von Schnering, *Z. Kristallogr.* **1981**, *155*, 307.

[7] M. J. Ferguson, R. W. Hushagen, A. Mar, *J. Alloys Compds.* **1997**, *249*, 191.

[8] H. Kleinke, *Eur. J. Inorg. Chem.* **1998**, 1369.

[9] G. A. Papoian, R. Hoffmann, *Angew. Chem. Int. Ed.* **2000**, *39*, 2408.

[10] B. E. Brown, *Acta Crystallogr.* **1966**, *20*, 268.

[11] P. C. Donohue, P. E. Bierstedt, *Inorg. Chem.* **1969**, *8*, 2690.

[12] F. Q. Huang, C. Flaschenriem, P. Brazis, C. R. Kannewurf, J. A. Ibers, *Inorg. Chem.* **2003**, *42*, 3194.

[13] N. Soheilnia, K. M. Kleinke, H. Kleinke, *Chem .Mater.* **2007**, *19*, 1482.

[14] B. Eisenmann, J. Klein, *Z. Kristallogr.* **1991**, *197*, 279.

[15] E. Eisenmann, J. Klein, M. Somer, *Angew. Chem. Int. Ed.* **1990**, *29*, 87.

[16] N. Soheilnia, E. Dashjav, H. Kleinke, *Can. J. Chem.* **2003**, *81*, 1157.

[17] M. Martinez-Ripoll, A. Haase, G. Brauer, *Acta Crystallogr.* **1974**, *B30*, 2006.

[18] A. Kjekshus, P. G. Peterzens, T. Rakke, A. F. Andresen, *Acta Chem Scand.* **1979**, *33A*, 469.

[19] W. B. Pearson, *Z. Kristallogr.* **1985**, *171*, 23.

[20] S. C. Yin, Y. H. Rho, I. Swainson, L. F. Nazar, *Chem. Mater.* **2006**, *18*, 1901.

[21] A. C. Larson, R. B. von Dreele, Los Alamos National Laboratory: Los Alamos, NM, **2000**.

[22] B. Harbrecht, A. Selmer, *Z. Anorg. Allg. Chem.* **1994**, *620*, 1861.

[23] F. Klaiber, W. Petter, F. Hulliger, *J. Solid State Chem.* **1983**, *46*, 112.

[24] H. Kleinke, *Chem. Commun.* **2000**, 1941.

[25] O. Jepsen, O. K. Andersen, *Z. Phys.* **1995**, *97*, 25.

[26] A. Kokalj, *J. Mol. Graph. Model.* **1999**, *17*, 176.

[27] C. J. Bradley, A. P. Cracknell, *The Mathematical Theory of Symmetry in Solids*, Clarendon Press, Oxford, **1972**.

[28] N. Soheilnia, J. Giraldi, A. Assoud, H. Zhang, T. Tritt, H. Kleinke, *J. Alloys Compds.* **In press**.

[29] K. P. Jensen, A. Kjekshus, T. Skansen, *J. Less-Common Met.* **1969**, *17*, 455.

[30] J. O. Sofo, G. D. Mahan, *Phys. Rev. B* **1994**, *49*, 4565.

[31] N. F. Mott, H. Jones, *The Theory of the Properties of Metals and Alloys*, Dover Publications Inc., New York, NY, **1958**.

[32] F. Gascoin, J. Rasmussen, G. J. Snyder, *J. Alloys Compds.* **2007**, *427*, 324.

[33] B. C. Sales, D. Mandrus, R. K. Williams, *Science* **1996**, *272*, 1325.

[34] G. A. Slack, in *CRC Handbook of Thermoelectrics* (Ed.: D. M. Rowe), CRC Press,

Boca Raton, FL, **1995**, pp. 407.

[35] H. Holseth, A. Kjekshus, *Acta Chem. Scand.* **1968**, *22*, 3284.

[36] A. Kjekshus, K. P. Walseth, *Acta Chem. Scand.* **1969**, *23*, 2621.

[37] H. Nowotny, J. Pesl, *Monatsh. Chem.* **1951**, *82*, 336.

[38] A. R. West, *Solid State Chemistry and its applications*, John Wiley & sons Ltd., Wiltshire, UK, **1997**.

[39] K. F. Hsu, S. Loo, F. Guo, W. Chen, J. S. Dyck, C. Uher, T. Hogan, E. K. Polychroniadis, M. G. Kanatzidis, *Science* **2004**, *303*, 818.

[40] S. R. Brown, S. M. Kauzlarich, F. Gascoin, G. J. Snyder, *Chem. Mater.* **2006**, *18*, 1873.

Chapter 5

5. Conclusion

The main focus of this research was on finding new early transition metal antimonides and arsenides for thermoelectric applications. Large molecular masses, complicated crystal structures and covalent bonds are desired properties for thermoelectric research.

Ir_3Ge_7 materials have the right structural features such as high symmetry (body centered cubic), large number of covalent bonds and fascinating anionic structure. We were able to successfully prepare two new members of this structure type ($Mo_3(Sb,Te)_7$ and $Re_3(Ge,As)_7$), thereby adding a new materials family to the thermoelectric research map. The existence of the cubic void in the anionic structure of these materials allowed us to investigate the effect of different cation additions on lowering the thermal conductivity (rattling effect) and other physical properties of these materials. The low electronegativity difference between the transition metal and the anionic structure results in covalent bonds and large electrical conductivity in these materials. Moreover, the presence of several flat bands around the Fermi level in the electronic structure of these materials is a very important feature of these materials, since these flat bands are responsible for achieving large Seebeck values.

The thermoelectric properties of these materials are comparable to some of the best thermoelectric materials for high temperature applications. Currently the effects of different cation additions as well as the partial replacement of anions on the physical properties of these materials continue to be under investigation. While more work needs to be done before final success can be assured, the outcome of this research constitutes a great starting point for finding new materials within this family and further improvements of the presented materials.

6. Appendix

Laue Class	Crystal Class	N_V (max)
m3m	cubic	48
m3	cubic	24
6/mmm	hexagonal	24
6/m	hexagonal	12
4/mmm	tetragonal	16
4/m	tetragonal	8
3m	trigonal	12
3	trigonal	6
mmm	orthorhombic	8
2/m	monoclinic	4

Table A. 1 Maximum N_V from selected symmetries for different Laue classes

Empirical formula	$ZrSi_{0.07(2)}Sb_{1.93}$	$ZrSi_{0.12(3)}Sb_{1.88}$	$ZrGe_{0.21(5)}Sb_{1.79}$	$HfGe_{0.2(2)}Sb_{1.8}$
Molar Mass [g/mol]	328.63	323.95	322.97	411.91
Wavelength [Å]	0.71073	0.71073	0.71073	0.71073
Space group	*Pnma* (62)	*Pnma* (62)	*Pnma* (62)	*Pnma* (62)
a [Å]	7.401(2)	7.365(1)	7.304(1)	7.312(3)
b [Å]	3.9898(9)	3.9733(8)	3.9513(6)	3.943(2)
c [Å]	9.610(2)	9.574(2)	9.576(2)	9.488(4)
V [$Å^3$]	283.8(1)	280.14(1)	276.35(7)	273.5(2)
Z	4	4	4	4
Density [g/cm^3]	7.692	7.681	7.763	10.002
Absorp. coeff. [mm^{-1}]	21.567	21.396	23.002	57.314
F(000)	558	551	550	680
2θ range [°]	6 - 60	6 - 60	6 - 70	6 - 70
Reflections collected	1088	1339	2850	1048
Indep. reflec. (R_{int})	390 (0.0382)	577 (0.0267)	660 (0.0711)	440 (0.0328)
Absorption correction	Empirical	Empirical	Empirical	Empirical
Max., min. trans.	1.00, 0.563	1.00, 0.7139	1.00, 0.774	1.00, 0.752
Goodness-of-fit on F^2	1.387	1.142	0.985	1.263
R(F), $R_W(F^2)$ $I > 2\sigma(I)$	0.043, 0.097	0.026, 0.056	0.049, 0.083	0.042, 0.067
Extinction coefficient	0.0001(7)	0.0013(4)	0.0001(3)	0.0013(2)
Max. diff. peak, hole [$e/Å^3$]	+2.95, -2.46	+2.06, -2.02	+2.08, -3.59	+3.16, -2.65

Table A. 2 Crystallographic data for $MA_\delta Sb_{2-\delta}$, M=Zr, Hf; A=Si, Ge.

Empirical formula	$Mg_{0.07(2)}Mo_3Sb_7$	$Ni_{0.04(1)}Mo_3Sb_7$	$Cu_{0.041(6)}Mo_3Sb_7$
Formula weight [g/mol]	1141.71	1142.42	1145.15
Wavelength [Å]	0.71073	0.71073	0.71073
Space group	$Im\bar{3}m$ (229)	$Im\bar{3}m$ (229)	$Im\bar{3}m$ (229)
a [Å]	9.5740(7)	9.5734(6)	9.5829(9)
V [$Å^3$]	877.6(1)	877.4(1)	880.0(1)
Z	4	4	4
Density [g/cm^3]	8.641	8.648	8.643
Absorp. coeff. [mm^{-1}]	25.229	25.312	25.342
F(000)	1935	1936	1941
2θ range [º]	6 - 70	6 - 60	6 - 70
Reflections collected	2213	1625	1193
Indep. reflec. (R_{int})	198 (0.047)	155 (0.085)	219 (0.036)
Absorption correction	Empirical	Empirical	Empirical
Max., min. trans.	1.00, 0.79	1.00, 0.043	1.00, 0.78
Goodness-of-fit on F^2	1.06	1.14	0.95
R(F), $R_W(F^2)$ ($I > 2\sigma(I)$)	0.023, 0.049	0.033, 0.063	0.022, 0.030
Extinction coefficient	0.00076(9)	0.0006(1)	0.00035(3)
Max. diff. peak, hole [$e/Å^3$]	+1.32, -1.64	+2.37, -1.78	+1.01, -1.24

Table A. 3 Crystallographic data for $A_\delta Mo_3Sb_7$, A=Mg, Ni, Cu.

Empirical formula	$Nb_3Sb_2Te_5$
Formula weight [g/mol]	1160.23
Wavelength [Å]	0.71073
Space group	$I\bar{4}3m$ (217)
a [Å]	9.8180(4)
V [Å^3]	946.39(7)
Z	4
Density [g/cm^3]	8.143
Absorp. coeff. [mm^{-1}]	24.189
F(000)	1940
2θ range [º]	5 - 70
Reflections collected	2376
Indep. reflec. (R_{int})	367 (0.036)
Absorption correction	Empirical
Max., min. trans.	0.74, 0.52
Goodness-of-fit on F^2	1.101
R(F), $R_W(F^2)$ ($I > 2\sigma(I)$)	0.025, 0.046
Extinction coefficient	0.00072(5)
Max. diff. peak, hole [e/Å^3]	+1.28, -1.24

Table A. 4 Crystallographic data for $Nb_3Sb_2Te_5$.

Empirical formula	Re_3GeAs_6
Formula weight [g/mol]	1080.75
Temperature [K]	298
Wavelength [Å]	1.3302
Space group	$Im\overline{3}m$ (229)
a [Å]	8.73180(7)
V [Å^3]	665.75(2)
Z	4
Density [g/cm^3]	10.78
2θ range [º]	4.9 - 115.1
R_P, R_{wP}, R_F^2	0.0358, 0.0482, 0.0265

Table A. 5 Crystallographic (neutron) data for Re_3GeAs_6.

Empirical formula	$Re_3Ge_{0.6}As_{5.4}$
Formula weight [g/mol]	1081.68
Temperature [K]	298
Wavelength [Å]	1.5406
Space group	$Im\overline{3}m$ (229)
a [Å]	8.7287(3)
V [Å^3]	665.05(8)
Z	4
Density [g/cm^3]	10.81
2θ range [º]	5 - 112.6
R_P, R_{wP}, R_F^2	0.0837, 0.0680, 0.050

Table A. 6 Crystallographic (X-ray) data for $Re_3Ge_{0.6}As_{6.4}$.